SLAC-141

Rho-Meson Production by Pions at 15 GeV/c: A Study of Vector Dominance and of Rho-Omega Interference

Blair N. Ratcliff

SLAC Report No. 141

December 1971

AEC Contract AT(04-3)-515

STANFORD LINEAR ACCELERATOR CENTER
Stanford University · Stanford, California

DISCLAIMER

SLAC-141
UC-34
(TH) and (EXP)

RHO-MESON PRODUCTION BY PIONS AT 15 GeV/c: A STUDY OF VECTOR DOMINANCE AND OF RHO-OMEGA INTERFERENCE*

BLAIR N. RATCLIFF

STANFORD LINEAR ACCELERATOR CENTER
STANFORD UNIVERSITY
Stanford, California 94305

PREPARED FOR THE U. S. ATOMIC ENERGY COMMISSION UNDER CONTRACT NO. AT(04-3)-515

December 1971

*Ph.D. dissertation.

Printed in the United States of America. Available from National Technical Information Service, U. S. Department of Commerce, 5285 Port Royal Road, Springfield, Virginia 22151.
Price: Printed Copy $3.00; Microfiche $0.95.

THIS PAGE

WAS INTENTIONALLY

LEFT BLANK

ABSTRACT

We present the results of a wire spark chamber experiment studying the reaction $\pi^- p \rightarrow \pi^+ \pi^- n$ at 15 GeV/c. The differential cross section, density matrix elements, and dipion mass distributions are given in the rho region for momentum transfers (t) less than $0.30 (\text{GeV}/c)^2$. The density-matrix elements and differential cross section exhibit structure in the forward direction ($-t < m_\pi^2$). Using the vector dominance model, a comparison is made with polarized and unpolarized single-pion photoproduction data which also exhibit structure in the forward direction. Qualitative agreement with the vector dominance model is found and, in particular, the transverse rho differential cross section displays a pronounced forward peak, analogous to that observed in single-pion photoproduction. Quantitative agreement is found for the unnatural-parity-exchange cross section and for the asymmetry at small momentum transfers. Elsewhere there are disagreements in detail which may not be explained by changes in normalization or the value of the rho-photon coupling constant. The data show a significant (> 4 standard deviations) rho-omega interference effect in the dipion mass distribution for $0.1 < |t| < 0.3 (\text{GeV}/c)^2$. The overall phase between the amplitudes in the observed data is dominated by transverse production and is shown to be -1.40 ± 0.45 (rad) which differs from the phase found at lower energies by $\simeq -\pi/2$. The lower limit on the branching ratio $\Gamma(\omega \rightarrow 2\pi)/\Gamma(\omega \rightarrow 3\pi)$ is 0.7% at the 95% confidence level.

ACKNOWLEDGMENTS

It is a pleasure to acknowledge the contributions of the many people who have made this experiment possible. I would like to express my sincere appreciation to my collaborators on the experiment: F. Bulos, R. K. Carnegie, G. E. Fischer, E. E. Kluge, D.W.G.S. Leith, H. L. Lynch, B. Richter, H. H. Williams, and S. H. Williams; and to thank them for all the things I have learned from them and with them during the course of the experiment. I am particularly indebted to my adviser, Professor Burton Richter, for suggesting this experiment to me and for his overall supervision of my work.

The design and construction of this experiment would have been impossible without the time and talents of many engineers and technicians at SLAC. I would like to extend my thanks for engineering help to U. Cummings, L. Karvonen, and E. Roskowski; for mechanical construction to H. Bowden, M. Lateur, R. Pickup, R. Ricks, and W. Walsh; and for electronics to M. Fishman, R. Friday, M. Gan, M. Hargain, D. McShurley, K. Mauro, and F. Rosche. Particular thanks are due A. Kilert, R. Friday, D. McShurley, and W. Walsh for their continuing efforts during the hectic trials and tribulations of experimental setup and operation.

On-line computer programming was provided by G. Armstrong, M. Beniston, R. Brody, D. Feick, and R. Good, while D. Budenaers, J. Good, M. Gravina, J. Schnecke, and K. Turcotte were instrumental in the off-line data handling and computing.

I am also very grateful to the many people who helped in the preparation of this report. Special thanks are due S. Dripps for translating illegible handwriting into unreadable prose and to A. L. Berg for her patient typing and

editing. H. Lynch and H. H. Williams read portions of the manuscript and made many helpful comments.

TABLE OF CONTENTS

LIST OF TABLES

LIST OF FIGURES

CHAPTER I

INTRODUCTION

The vector mesons were first observed experimentally early in the past decade, beginning with the discovery of the ρ meson[1] in 1961 and followed shortly thereafter by the discovery of the ω, ϕ, and K*.[2] Historically, theoretical predictions of their existence had been made some time earlier from the behavior of the nucleon form factor data. Nambu[3] postulated the existence of an isoscalar vector meson in 1957 in order to explain the charge distributions of the neutron and proton. Shortly thereafter, Frazer and Fulco[4] were also led to the prediction of an isovector vector meson from the behavior of the electromagnetic structure of the nucleons.

At the same time that these predictions were being made from the form factor data, other theorists who were attempting to construct a theory of strong interactions were led to similar predictions for the existence of vector mesons on the basis of conserved currents and universality. In 1960, Sakurai[5] formulated a theory in which an isovector and two isoscalar vector mesons played key roles. This theory was subsequently extended, using the idea of unitary symmetry, by Salam and Ward[6] and later independently by both Gell-Mann[7] and Ne'eman[8] to accommodate all of the vector mesons.

The interrelation between these two different approaches was provided in 1961 by Gell-Mann and Zachariasen[9] who emphasized the idea of the vector meson dominance of the electromagnetic form factors of the hadrons. The vector dominance hypothesis[10,11] was later extended to apply to all of the electromagnetic interactions of the hadrons.

It is curious, in retrospect, that the vector mesons should have been predicted from the form factor data since more recent measurements show

a more rapid falloff with momentum transfer than is expected from the vector-meson propagator.[12] Despite this difficulty, however, the idea of vector dominance has been of great utility in describing many other reactions involving the hadronic interactions of the photon. In particular, the vector dominance model (VDM) provides a direct relationship between single-pion photoproduction and the reaction[11]

$$\pi^- p \rightarrow \rho^o n \quad . \tag{I.1}$$

It is to a study of this relationship that we address ourselves here.

The essence of the VDM can be summarized by the following statement.[10] The entire hadronic electromagnetic current $\left[j_\mu(x)\right]$ is identical with a linear combination of the known neutral vector meson fields $\left[\rho^o_\mu(x),\ \omega_\mu(x),\ \phi_\mu(x)\right]$. That is,

$$j_\mu(x) = -\left(\frac{m_\rho^2}{2\gamma_\rho}\,\rho^o_\mu(x) + \frac{m_\omega^2}{2\gamma_\omega}\,\omega_\mu(x) + \frac{m_\phi^2}{2\gamma_\phi}\,\phi_\mu(x)\right) \tag{I.2}$$

where m_V denotes the vector meson mass and γ_V is the inverse vector-meson-photon coupling constant. Using general arguments from field theory,[10,13] it can then be shown that Eq. (I.2) implies a direct relationship between a photoproduction amplitude from a nucleon N and a linear combination of the corresponding production by the transversely polarized vector mesons (V_{tr}),

$$T(\gamma N \rightarrow \pi N) = \sum_{\rho,\omega,\phi} \frac{e}{2\gamma_V}\, T(V_{tr} N \rightarrow \pi N) \ . \tag{I.3}$$

In deriving Eq. (I.3), it is assumed that γ_V is independent of the photon mass (q^2) at the γ-V vertex and that the amplitude $T(V_{tr} N \rightarrow \pi N)$ is also a slowly varying function of q^2.

A somewhat simpler and more pictorial way to arrive at Eq. (I.3) is through the vector-meson-photon analogy[14] as shown in the following diagrams.

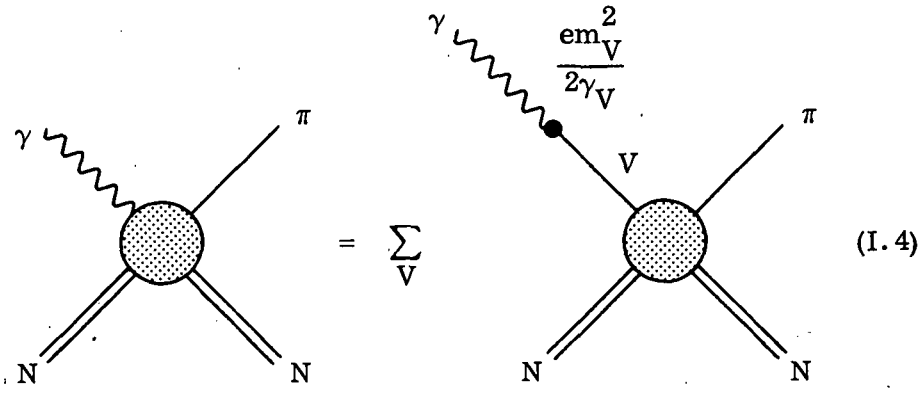

(I.4)

According to these diagrams, the interaction of the photon with the nucleon is mediated by the known vector mesons. The γ-V process occurs via a coupling constant $em_V^2/2\gamma_V$, which changes the photon into a vector meson with a certain coefficient without changing its helicity. Since a photon is always transverse, this immediately implies Eq. (I.3).

By utilizing time-reversal invariance, the amplitudes on the right-hand side of Eq. (I.3) can be reversed, which then defines a direct relationship between single-pion photoproduction and vector meson production by pions,

$$T(\gamma N \rightarrow \pi N) = \sum_{\rho, \omega, \phi} \frac{e}{2\gamma_V} T(\pi N \rightarrow V_{tr} N) \quad . \qquad (I.5)$$

As will be discussed in Chapter VI, the contributions from the ϕ and ω mesons are expected to be small so that, experimentally, Eq. (I.5) relates single-pion photoproduction to reaction (I.1).

Studies of single-pion photoproduction at SLAC[15] and DESY[16] have shown a pronounced forward peak in the differential cross section ($d\sigma/dt$) over a large range of incident photon energies. The cross section was shown to increase by about a factor of two for momentum transfers to the nucleon between

$-t = m_\pi^2$ and $-t=0$. In addition, experiments with linearly polarized photons[17] have also shown dramatic structure for $-t < m_\pi^2$. In particular, the unnatural-parity-exchange cross section rises dramatically from zero at $-t = m_\pi^2$ to equality with the natural-parity-exchange cross section at $t=0$. The VDM then predicts through Eq. (I.5) that similar structure will be observed in the production of transverse rho mesons by pions.

Many previous comparisons of reaction (I.1) with single-pion photoproduction using the VDM have been made.[11,18-21] These tests have shown a general agreement when comparison is made with the unpolarized photoproduction data using a coupling constant of $\gamma_\rho^2/4\pi \approx 0.45$. However, in no case have the ρ^o data been sufficient to permit a direct comparison for small values of momentum transfer ($-t < m_\pi^2$) where the photoproduction data show the sharp structure.

The VDM has been observed to fail badly when comparison is made with photoproduction data obtained with linearly polarized photons.[22-24] However, all such comparisons have been made at rather low energies, and once again information has been lacking at small values of momentum transfer.

In addition to its intrinsic interest, the validity of the VDM in the small momentum transfer region has important practical implications for analyses which attempt to extract the π-π scattering amplitude by the Chew-Low technique[25] of extrapolating data to the pion pole. Such analyses in the past[26] have not had data available in the small momentum transfer region and so have generally relied upon the elementary one-pion-exchange prediction that the differential cross section should vanish at $t=0$. In contrast to this prediction, single-pion photoproduction data predict through the VDM that the cross section for transverse ρ^o production has a sharp rise at $t=0$, and similar

predictions are also made by absorptive exchange models.[27] It is thus of great interest to check the validity of this prediction of the VDM by determining directly the behavior of the $\rho^o n$ cross section for small values of t.

A study of $\pi^- p \to \pi^+ \pi^- n$ is also of interest because of the possible observation of the interference effect between the ρ^o and the ω. The possibility that the ω and ρ^o could mix with one another through the electromagnetic interaction was first suggested by Glashow[28] shortly after the discovery of these vector mesons in 1961. It was pointed out that the ω and ρ^o differed by no quantum number which was respected by electromagnetism, so that electromagnetically induced transitions between the ω and ρ^o could occur. Moreover, this effect might be greatly enhanced by the near degeneracy between the masses of the two mesons.

Such a mixing of states would manifest itself by the G-parity violating decays $\omega \to \pi^+ \pi^-$ and $\rho^o \to \pi^+ \pi^- \pi^o$. Because the ω width ($\Gamma_\omega \simeq 12$ MeV) is so much narrower than that of the ρ^o ($\Gamma_\rho \simeq 150$ MeV), the two-pion decay of the ω is much the easier of the two decays to observe experimentally. Consequently, searches for the ρ-ω effect have concentrated on reactions with two pions in the final state such as reaction (I.1).

Perhaps the first significant evidence for the $\omega \to \pi^+ \pi^-$ decay was reported by Flatté et al.[29] in 1966. This experiment studied the reaction $K^- p \to \Lambda \pi^+ \pi^-$ at several energies and observed a 3.4 standard-deviation peak at an incident kaon momentum of 1.5 GeV/c. However, the other momenta from 1.7 to 2.7 GeV/c showed no significant effect. Flatté assumed that this was due to an energy-dependent interference between a small ω amplitude and large ρ^o and background amplitudes.

Beginning in 1969 and continuing to the present, a large number of experiments have been reported[30] which have observed statistically significant anomalies in the region of the ω. Perhaps the most compelling of those which observed production by way of the strong interactions was carried out by G. Goldhaber et al.[31] at 3.7 GeV/c. This experiment studied the $\pi^+\pi^-$ mass spectrum in the reaction $\pi^+ p \to \pi^+\pi^-\Delta^{++}$. A destructive interference effect was observed which consisted of a 3.5 standard-deviation dip at the mass of the ω.

Effects with similar statistical significance have been seen in other reactions.[30] However, all of these experiments have been at quite low energies. For example, the experiments which have seen significant effects in the reaction of interest here, $\pi^- p \to \pi^+\pi^- n$, have all been at energies below 5 GeV. Moreover, the results of only one such experiment[32] with high statistics (at 2.3 GeV/c) have been published, and because of the nature of the effect which is seen (a peak), the value of the overall phase between the ρ^0 and ω amplitudes is not well determined in this experiment without additional assumptions. It is therefore of great interest to search for the ρ-ω interference effect in this reaction both to demonstrate that an effect indeed exists in $\pi^+\pi^- n$ at high energies and to gain some insight into its possible energy dependence.

The present experiment, which was begun in 1968, utilized a wire spark chamber spectrometer at SLAC to study pion interactions from hydrogen at high energy. Primary emphasis was placed upon a study of the reaction

$$\pi^- p \to \rho^0 n$$

in the small momentum transfer region at 15 GeV/c. However, in order to avoid biases, the triggering requirements were quite nonrestrictive which

allowed information on many other processes to be gathered in addition. For example, the spectrometer simultaneously detected reactions such as

$$\pi^- p \rightarrow \pi^+ \pi^- \Delta^o \quad ,$$

$$\pi^- p \rightarrow K^o \Lambda^o \quad \text{and} \quad K^o \Sigma^o \quad ,$$

and

$$\pi^- p \rightarrow \pi^+ \pi^- \pi^- p \quad .$$

Moreover, since the spectrometer contained a Cerenkov counter to identify the forward particles in the final state, the reactions

$$\pi^- p \rightarrow K^+ K^- n$$

and

$$\pi^- p \rightarrow p\bar{p}n$$

could also be detected.

The analysis of several of these final states is currently in progress and will be discussed elsewhere. This thesis concentrates on a study of the reaction $\pi^- p \rightarrow \pi^+ \pi^- n$ at 15 GeV/c in the region of the ρ^o. Primary emphasis is placed upon the behavior of this reaction for small values of momentum transfer as a test of the vector dominance model and also upon a study of the ρ-ω mixing. A short discussion of the theory of the VDM and results from this analysis are presented in Chapter VI, whereas Chapter VII discusses the physics and the results of the ρ-ω interference analysis.

The other sections of the thesis discuss the details leading up to these results. Chapter II details the experimental apparatus, whereas Chapter III discusses the reconstruction programs and the reduction of the data. In Chapter IV, we describe the performance of the experimental system and relate it to a study of the elastic diffraction scattering of pions from hydrogen. Finally, Chapter V discusses the analysis and results of the $\pi^+ \pi^- n$ data in the ρ^o region.

CHAPTER II

EXPERIMENTAL CONSIDERATIONS

A. Design Considerations and General Description

The basic design of the experimental apparatus was motivated by the desire to study the reaction $\pi^- p \rightarrow \rho^o n$ with high statistics in the small momentum transfer ($-t < m_\pi^2$) region in order to make a comparison with single-pion photoproduction through the vector dominance model. This comparison required the determination of the differential cross section and spin density matrix elements as functions of t in the forward direction ($-t < m_\pi^2$). Thus, a large number of events with good momentum transfer resolution was required. Because the photon and ρ^o have different masses, the experiment had to be done at high incident energies. Since it was necessary to distinguish between $\rho^o n$ and $\rho^o N^*$ final states, good resolution in the missing mass was a necessity. Moreover, the apparatus had to distinguish pions from heavier particles such as kaons in the final state to insure that they contributed no significant bias for the $\rho^o n$ data sample.

The spectrometer which was designed in accordance with these considerations is shown in Fig. 1. The incident pion entered the LH_2 target after being counted and analyzed for momentum and angle in the beam hodoscopes. This analysis was necessary in order to have the required resolutions in momentum transfer and missing mass. The produced events were detected by triggering hodoscopes A and B located behind the main analyzing magnet. The triggering criteria were kept quite loose to avoid triggering biases and to allow collection of final states in addition to $\rho^o n$. The vector momenta of the outgoing tracks were measured by 7 wire spark chambers with magnetostrictive readout. Three of these chambers were located in front of the magnet

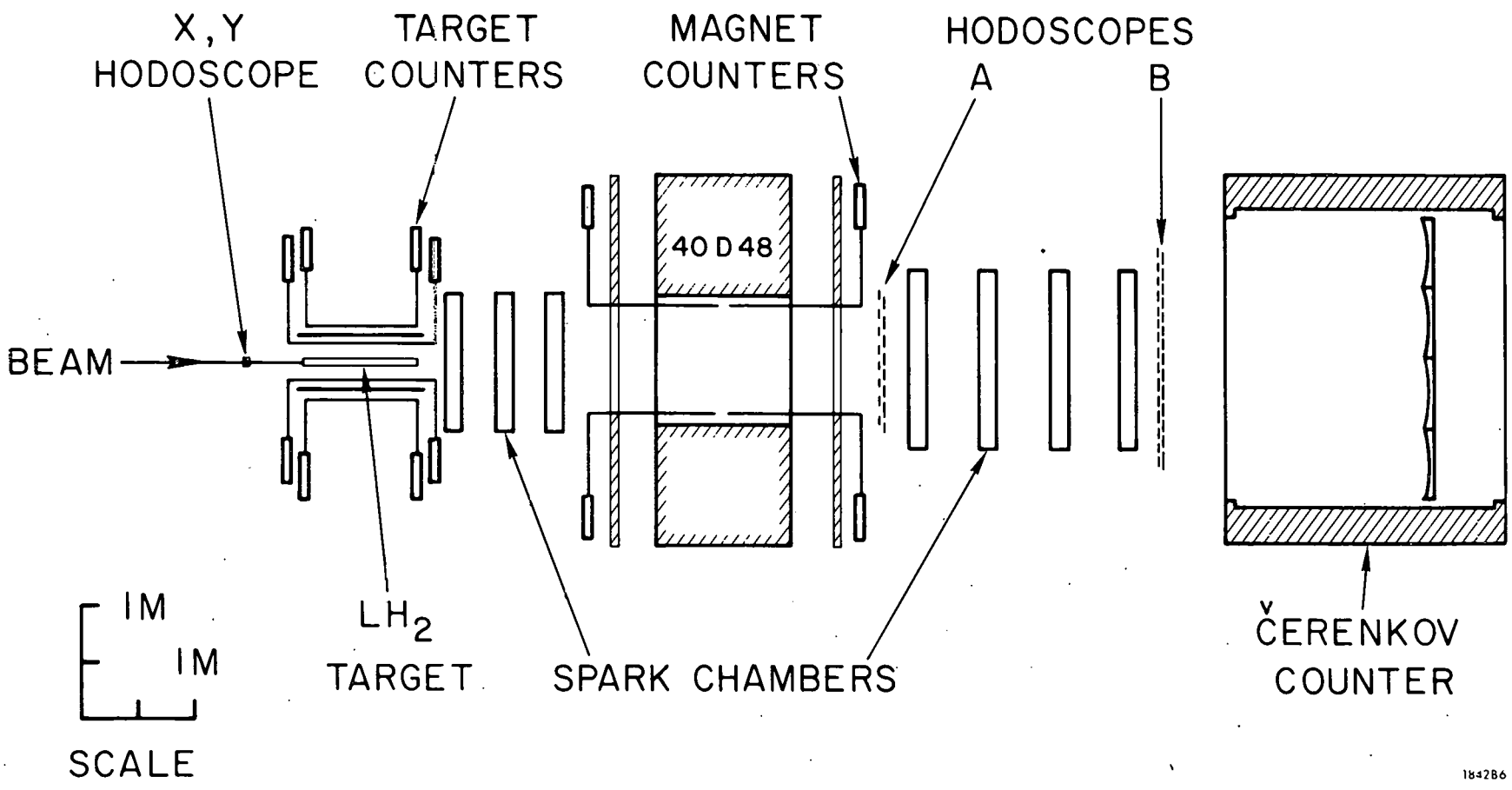

FIG. 1--Plan view of the experimental apparatus.

with 4 chambers following it. A large-aperture, high-pressure Cerenkov counter located after the last set of spark chambers differentiated between pions and higher mass particles in the final state. A scintillator-Pb sandwich counter surrounded the target to detect particles which escaped the spectrometer and to aid in the differentiation between $\rho^{o}n$ and $\rho^{o}N^{*}$ final states. The inside faces of the magnet were also lined with counters to veto particles which intersected the magnet iron. Information from both the Cerenkov counter and the target counters was not a part of the system trigger requirements and was used only in the off-line analysis. An on-line computer performed the data logging and continuously monitored the performance of the spectrometer.

The following are detailed descriptions of the major components of the experimental apparatus and the data collection procedures.

B. Beam

The pion beam, whose layout is shown in Fig. 2, was produced by steering the primary electron beam at $\sim$19 GeV/c onto a one-radiation-length beryllium target. Particles produced at an angle of $\sim 1^{o}$ were focused into the existing rf-separated beam line which served the SLAC 82" bubble chamber. This beam line contained a momentum defining crossover and was achromatic at the second focus. A pulse magnet located at the second focus allowed individual pulses to be delivered at rates up to 180 pulses/sec either to the bubble chamber or to the beam line which served this experiment. Thus, it was possible, for example, to transmit pions to this experiment and kaons of the same momentum to the bubble chamber on a pulse-by-pulse basis.

After entering our beam line, the beam deflection was increased by septum magnets immediately following the second focus. The beam was then focused

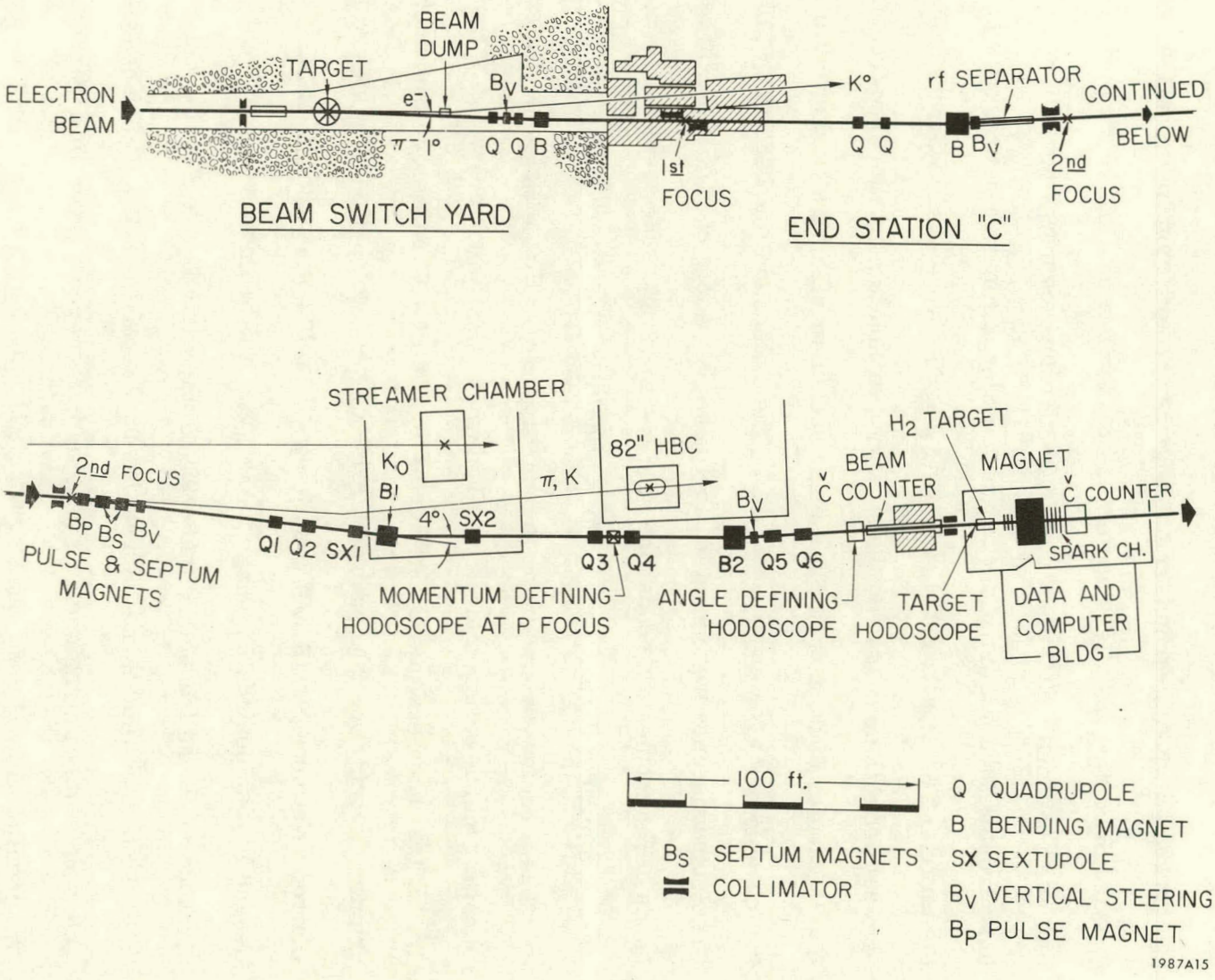

FIG. 2--Layout of the beam transport system.

at the momentum hodoscope by quadrupole pair Q1-Q2 after being momentum dispersed by bending magnet B1. The downstream quadrupole pair Q5-Q6 focused the image of this point to the center of the upstream wire spark chamber package of the spectrometer. Q3-Q4 focused off-momentum rays which crossed the optic axis at sextupole SX2 onto the center of B2 so that the system was achromatic just upstream of Q5. Sextupoles were used to correct the most troublesome second-order terms in order to improve beam spot size at the target. Two small vertical steering magnets were used to correct for vertical deflections caused by the rf separator and to bring the beam correctly into the center of the target. The beam had an angular pass band of ±2.5 mrad horizontally and ±3.5 mrad vertically. The momentum passband was ±2.5%. Counter hodoscopes were used to label particles within each of these three bands. The momentum hodoscope resolved to ±0.3%. The resolution in angle was ±0.5 mrad utilizing vertex information from the spectrometer.

Beam setup was done using the spectrometer. Beam quality during experimental running was monitored by a hodoscope (XY) which consisted of four 1/2" × 1/2" counters joined together to form a 1" × 1" hodoscope with each counter covering one x-y quadrant. This counter was surrounded by a ~5" diameter veto counter (RING) containing a 1" × 1" hole. The XY-RING assembly was located 10" before the target. The beam was centered in the XY hodoscope and focused so that ~92% of the particles were within the 1" × 1" square. Additional information on the quality of the beam was available from the beam angle and momentum hodoscopes. Beam line transmission was monitored by comparing the particle flux at the XY hodoscope with that measured in two scintillation counters (S1-S2) located at the second focus. The beam intensity was typically 10 pions per 1.6-μsec machine pulse.

Electrons were filtered from the beam before the second focus by placing a 1/2" lead filter at the first focus. The electron contamination at 15 GeV/c was measured to be less than 0.2% both by attenuation measurements with the filter and by a shower counter located behind the main spectrometer. Muon contamination was measured to be $\sim 3.9\%$ (corrected to the target position) by use of a muon telescope consisting of a variable number of 9.5" blocks of iron interspersed with scintillator. This amount of muon background was consistent with that expected from pion decay in the beam and was the major contributor to the beam halo. Total K^- and $\bar{p}$ contamination were shown to be less than 0.3% by a threshold Cerenkov counter located before the XY hodoscope.

C. Target

The target in this experiment was a 40" × 2" cylinder of liquid hydrogen. The density of the liquid hydrogen was monitored by two calibrated platinum resistors located in the cell, and by measurements of the hydrogen vapor pressure in the outlet tube. Checks were made of these quantities at four-hour intervals during the run and they were found to be extremely stable. In addition, the resistor readings were recorded continuously on strip-chart recorders for later use in the off-line analysis.

D. Spark Chamber System

The experiment contained 7 wire spark chambers; three 40" × 24" chambers before the analyzing magnet and four 60" × 40" chambers following it. Each chamber consisted of four planes (two gaps). The first gap contained conventional orthogonal x-y planes whereas the planes of the second gap were inclined at angles of $\pm 30^{\circ}$ with respect to the vertical to resolve ambiguities in track reconstruction. The wire planes were constructed with an

aluminum-polyester cloth having a wire spacing of 0.040"/wire. A special stretcher and optical alignment system allowed the wires to be aligned to a tolerance of 0.010". To minimize rf pickup in the electronics, the structure of a chamber was planned so that when assembled it formed a closed box with its sides and windows at ground potential. Since the main pion beam passed through the chambers, a polyurethane plug was installed in each gap to prevent extra tracks due to beam particles. Care was taken to insure that spurious sparking did not occur at either the edges of the plug or the edges of the chamber.

Each of the chamber planes was read out using magnetostrictive techniques. The principle of magnetostriction is straightforward. When a spark current passes over a magnetostrictive wire, it produces an acoustic wave which travels with the velocity of sound ($\sim 0.2"/\mu sec$) along the wire. A small coil located at the end of the wire transforms this wave into an electrical signal. The time taken for the wave to reach the pickup coil determines which chamber wires carried the current, and hence, one coordinate of the spark position. The orthogonal (or crossed) coordinate is measured in a similar fashion on the other plane of the gap.

In order to illustrate the most important features of the chamber construction, Fig. 3(a) shows a typical chamber plane and Fig. 3(b) depicts a cross section of the chamber. Note particularly the lucite guide for the magnetostrictive "wand" which was an independent unit containing the amplifier and pickup coil attached to a support bar which supported the magnetostrictive wire. "Start" and "stop" fiducials at the chamber edges eliminated the necessity of accurately positioning the pickup coil with respect to the chamber. The wand could be inserted into the guides from either end as a check on

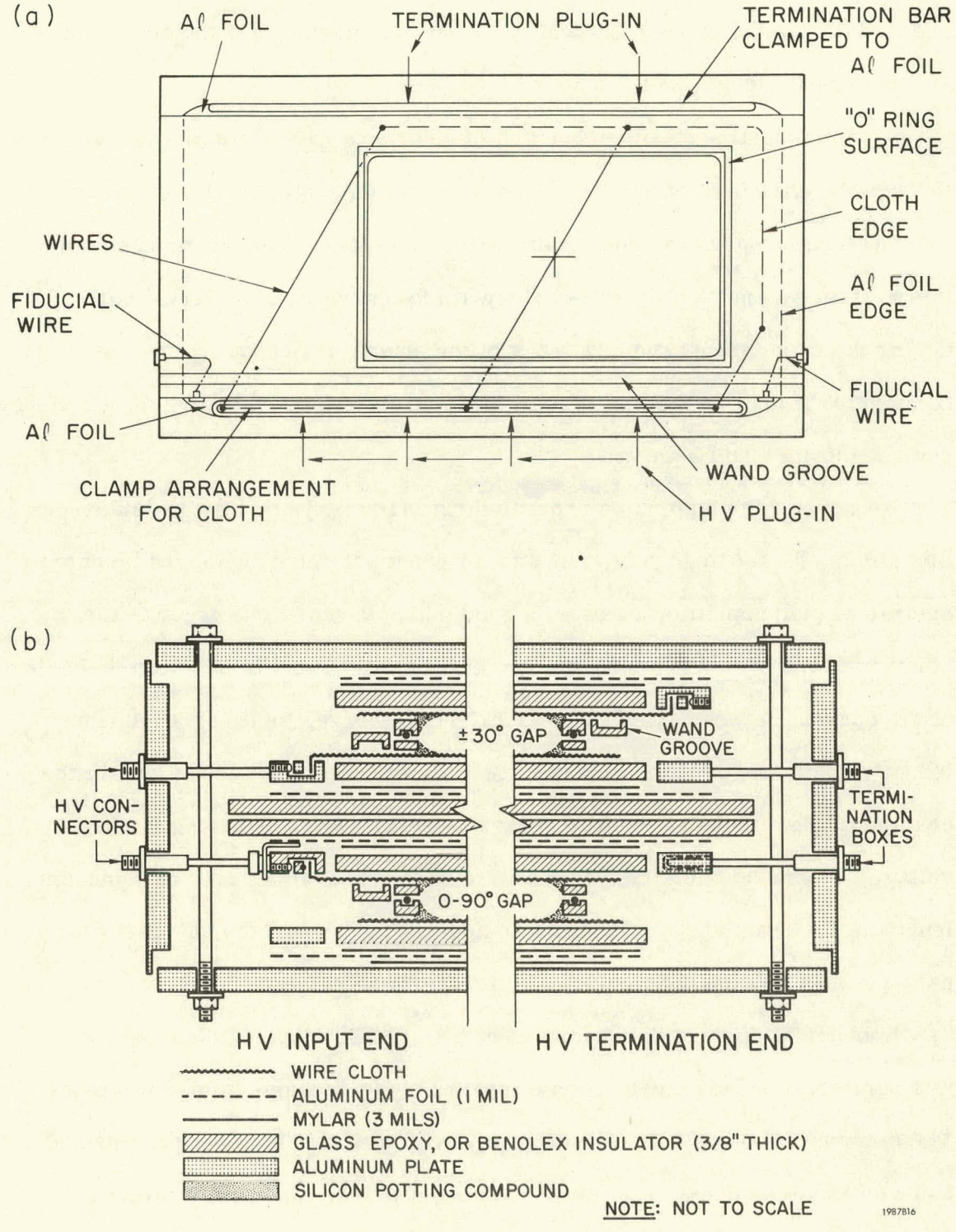

FIG. 3--(a) Typical wire-chamber plane, (b) cross section of a spark chamber.

possible nonlinearities in the readout. The linearity of the wand units was checked before the experiment and the wand was discarded if the accumulated error along its length was > 0.01".

A commercial spark chamber gas of 90% neon - 10% helium was circulated through the chambers with a pump and purification system containing high-temperature furnaces to remove nitrogen and oxygen. The performance of this system was not totally satisfactory at high pulse rates. Periodically during the experiment, the efficiency of the chambers fell due to the gas becoming "poisoned." The gas system then had to be flushed before the efficiency returned to its usual high value.

Because of the high pulse repetition rate (180 pps) and high instantaneous flux (10 π^- per 1.6 μsec pulse), it was necessary that the chambers be able to operate at high repetition rates with good multiple-spark efficiency. The primary cause of low multiple-spark efficiency was found to be unequal sharing of the current between sparks due to differences in the total resistive and inductive path length of the spark current for different spark locations in the chamber. This path-length difference was equalized by replacing the high-voltage and ground bus strips with a wire having the same resistance per unit length as the chamber wires. This compensation allowed the chambers to have the excellent multiple-spark efficiency shown in Fig. 4.

In order to operate the chambers at high rates, a pulsed clearing field was applied to prevent re-ignition of sparks along previous breakdown paths. The clearing field had a 50-volt dc component upon which was superimposed a 250-volt pulse, 3 msec long, after each beam pulse. Each gap received its high voltage by means of a set of four 50-ohm cables connected in parallel. The HV pulse was generated by discharging a matching set of cables through a

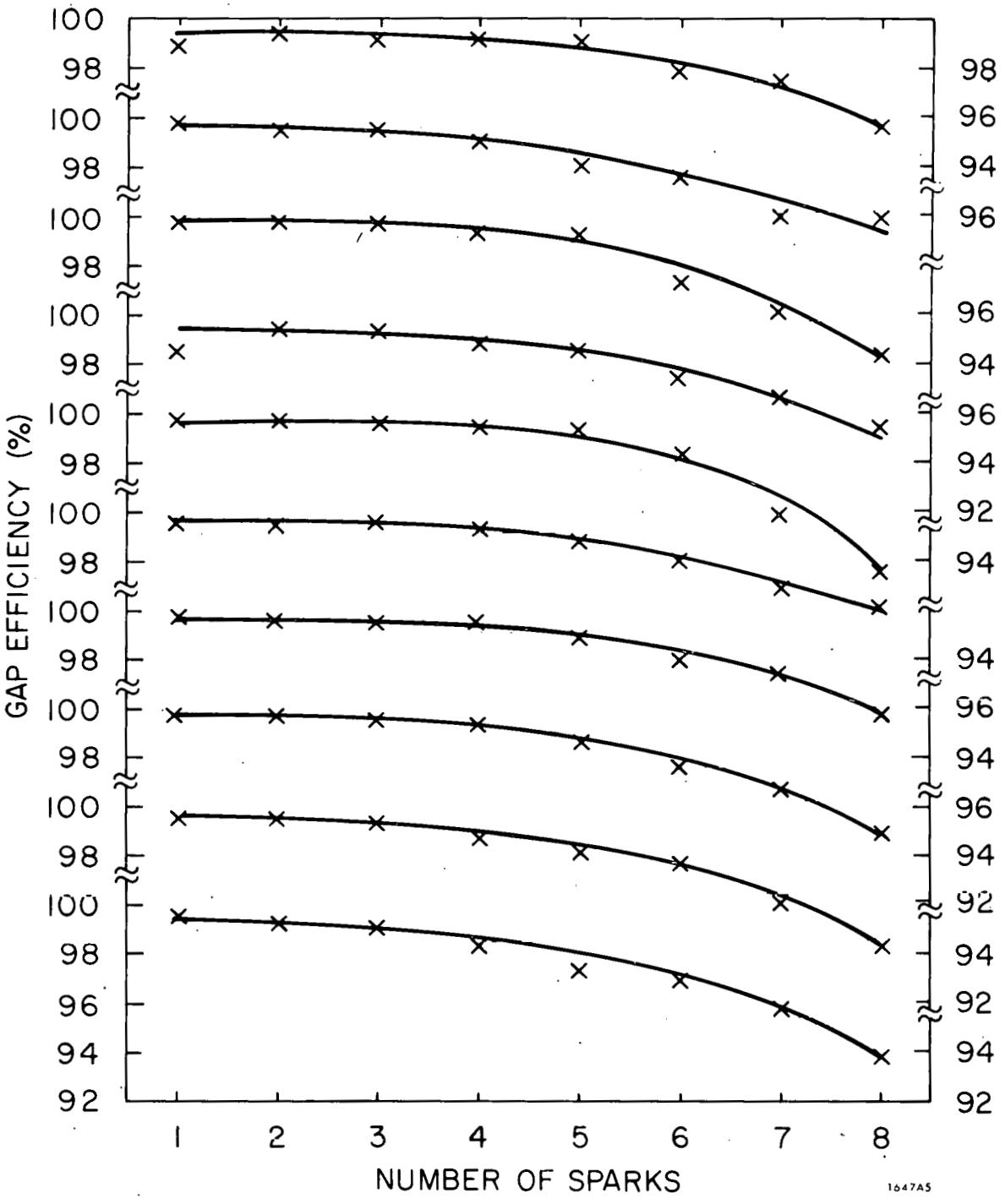

FIG. 4--Gap efficiency of the spark chambers.

series hydrogen thyratron. Typically the chambers operated with a 6-kV rectangular pulse 225 nsec in length. The system was designed to spark at rates as high as 180 pps. However, during actual running the maximum repetition rate was approximately 100/sec and the average data rate was ~ 10 events per second. No deterioration in the performance of the chambers was noted at the highest repetition rates used.

The spark coordinates were recorded using a gated clock and scaler system. The arrival of the "start" fiducial caused 8 scalers to begin counting a 20-MHz clock pulse. As subsequent pulses arrived, the scalers were gated off in succession. Each scaler thus contained a number corresponding to the delay time between the arrival of the "start" fiducial and the arrival of the spark pulse. If the plane contained less than 8 coordinates, the "stop" fiducial was also seen. The known physical distance between the "start" and "stop" fiducials defined the distance scale for transforming the scaler readings to spark coordinates in space. Since the average number of sparks per plane was typically 4 with $\sim 3\%$ overflow, the "stop" fiducials were seen on nearly every pulse. This allowed continuous fiducial monitoring and updating during data reconstruction. The velocity of a signal along a magnetostrictive wire was ~ 50 nsec/0.010" so the 20-MHz clock provided a least-count accuracy of 0.010". During the experimental run, other uncertainties in the spark position contributed so that the resolution in position (sigma) was ~ 0.015" to 0.020".

A more complete discussion of the design and performance of the wire spark chamber system is presented in the articles of F. Bulos, M. Gan, and H. Lynch.[33]

E. Spectrometer Magnet

The spectrometer magnet gap was 15" high along the field direction (y) and 40" wide in the bend plane (x) with 48" pole faces along the beam axis (z). Magnetic-mirror plates were installed at both the entrance and exit of the gap to prevent high flux leakage into the spark chamber region.

The field was quite uniform over the whole aperture and, for purposes of track reconstruction, was well approximated by a pure dipole with small focusing terms. The field was mapped before the experiment with a Hall probe. These results were checked by comparison with measurements of the $\int B_y dz$ taken with a long flip coil. The two measurements agreed to an accuracy of $\sim 0.2\%$.

The field integral ($\int B_y dz$) was set to 1040 kG-in. during the experimental run. Field strength was monitored during the experiment by computer readout of the magnet excitation current. Measurements of the flux at the center of the magnet were made at hourly intervals throughout the experiment with both a Hall probe and a nuclear magnetic resonance detector and were recorded for later use in the off-line analysis.

F. Counters

The beam transport system contained three counter hodoscopes which were used to label incident particles in momentum (P) and angle (θ, ϕ). Each of these hodoscopes consisted of a number of 1/8" thick scintillator strips attached to photomultipliers. The counters were arranged to overlap so that the number of bins, and hence the effective resolution, was increased.

The 6 P counters overlapped to form 11 bins each with a resolution of $\pm 0.3\%$. Similarly, 6 ϕ counters formed 11 bins in the vertical angle and 4 θ counters formed 7 bins in the horizontal angle. Angles were measured

using the vertex position of the reconstructed event to determine the point at which the incident particle interacted in the target which gave an angular resolution of ±0.5 mrad.

The primary flux counter in the beam was the XY-RING hodoscope which was located 10" before the target. This hodoscope consisted of four 1/2" × 1/2" × 1/4" counters joined together to form a 1" × 1" hodoscope (XY) with each counter covering one x-y quadrant. This counter was surrounded by an ~ 5" diameter veto counter (RING) containing a 1" × 1" hole. The XY-RING hodoscope was used to monitor the incident beam flux as was mentioned previously. In addition, it determined the position of the incident particle to ±1/4". The accurate determination of the incident particle position was particularly important for those events which did not have two high momentum tracks coming from the production vertex (e.g., $\pi^- p$ elastic scattering). In this case, the vertex position could not be reconstructed from the spectrometer information, so the position of the incoming particle was used instead for calculating the incident beam angle and the position of the scattering vertex in the target.

The triggering counter system consisted of two "picket fence" hodoscopes. Hodoscope A, which contained 20 2-1/4" × 20" × 1/4" strips of scintillator connected to individual photomultipliers, was located immediately following the analyzing magnet. Hodoscope B, which contained 34 2-1/4" × 32" × 1/4" similar counters, was located after the last set of chambers. The hodoscope dimensions were such that the acceptance of the spectrometer system was not limited by the active area of the triggering counters. Since the incident beam passed through the hodoscopes, a small lucite plug was inserted in the appropriate counter to desensitize the beam region.

In order to veto particles which intersected the pole faces, the inside gap of the magnet was lined with 3/8"-thick scintillator strips connected to photo-tubes through adiabatic light pipes. Twelve counters were used in all.

The target-veto hodoscope was constructed as an open-ended box which surrounded the target. It consisted of two layers of 3/8" scintillator with 1/2" of lead between them to convert photons and stop low-energy charged particles. Each layer of scintillator contained 4 independent counters, each forming one side of the box. This design allowed the counters to give some information as to the nature of the counted particle and was useful for rejecting higher missing mass background in the $\pi^+\pi^-$n and the elastic scattering data samples.

All counter timings and, with the exception of the spectrometer veto counters, all counter high voltages were set with scattered particles from the pion beam. It was not possible to set the high voltages of the veto counters with scattered beam particles since a large fraction of such particles enter these counters very obliquely and have correspondingly large path lengths through the scintillator. It was necessary, however, to be able to count particles with the minimum path length through the scintillator, so the high voltages of the veto counters were set using cosmic rays.

Efficiencies of all counters were measured before their assembly in the spectrometer using either a cosmic-ray or a beta-ray coincidence telescope and were shown to be $\gtrsim 99\%$ over their active surface. Counter performance was monitored on-line by a comparison of singles rates. With the exception of triggering hodoscopes, any inefficiency of the counters only decreased the usable incident pion flux or increased the total analysis time and did not bias the measured angular distributions or cross sections. However, any inefficiency in either hodoscope A or B caused a loss of those events in which one

of the particles intersected the inefficient counter since a track was required to have "live" hodoscope counters at both ends during track reconstruction (see Chapter III.B). In order to insure that such an event loss did not affect the results, the efficiencies of the counters in these hodoscopes were measured on the actual data sample by reconstructing a subset of the data without the hodoscope matching condition. By using the large Cerenkov hodoscope to ensure that these reconstructed tracks were actually in time with the main-event pulse, the efficiency of the hodoscopes was measured as a function of the position of the track. This measured efficiency was then utilized in the Monte Carlo calculation (see Chapter V.B) which was used to correct for the detection efficiency of the spectrometer. As was noted previously, the individual hodoscope counters were $\gtrsim 99\%$ efficient over their active surface. However, there were physical cracks where the counters joined together in the hodoscope so the average inefficiency for a particle passing through a hodoscope was $\sim 2.5\%$.

Information from the above counters was used in two different ways. First, certain counters (e.g., P, θ, ϕ) were scaled in the hardware in order to monitor the distributions of the incident beam. These scaled quantities were used during the experimental run and were also read out periodically onto magnetic tape for later use during the off-line analysis. Second, for the event-by-event computer readout, it was necessary to determine which counters had fired in time with the event pulse (see Section G). This was done by comparing the timing of a discriminated output from each of the counters with that of the event pulse at strobe buffer units. If a coincidence occurred, a flip-flop corresponding to the counter was set positive and the information stored until it was read by the computer.

G. Electronics and Triggering

The fast electronics was the generator for the 16-nsec event pulse which fired the spark chambers and caused the event information to be read by the computer. An event was defined as follows:

1. One particle through XY.
2. No other particle within ~±16 nsec of this particle in either XY or the RING.
3. At least one counter fired in hodoscope A and two counters fired in hodoscope B or one counter fired in hodoscope B and two counters fired in hodoscope A.
4. No particles in the magnet veto counters.

We write this as

$$\text{Event} = (XY) \cdot \left[\overline{(XY > 1) + (R)}\right] \cdot \left[(2A \cdot 1B) + (2B \cdot 1A)\right] \cdot (\overline{Mag}) .$$

The basic motivations for this choice of the event trigger were straightforward. The incident flux (π^-) was defined to be $(\pi^-) = (XY) \cdot \left[\overline{(XY > 1) + (R)}\right]$ since this allowed the remainder of the electronics system to be effectively dead timeless. The loose triggering hodoscope condition was chosen primarily so that events which had both particles focused into the same triggering hodoscope counter would not be lost. Secondarily, it allowed the hodoscope efficiencies to be measured on the experimental data as was mentioned in Section F. The magnet counters were used as a veto on the trigger during most of the run since they reduced the background substantially from high multiplicity events which interacted with the magnet iron.

The method used to generate (π^-) is illustrated in Fig. 5. (XY) was simply the sum of the discriminated outputs of the 4 XY quadrant counters. The (R)

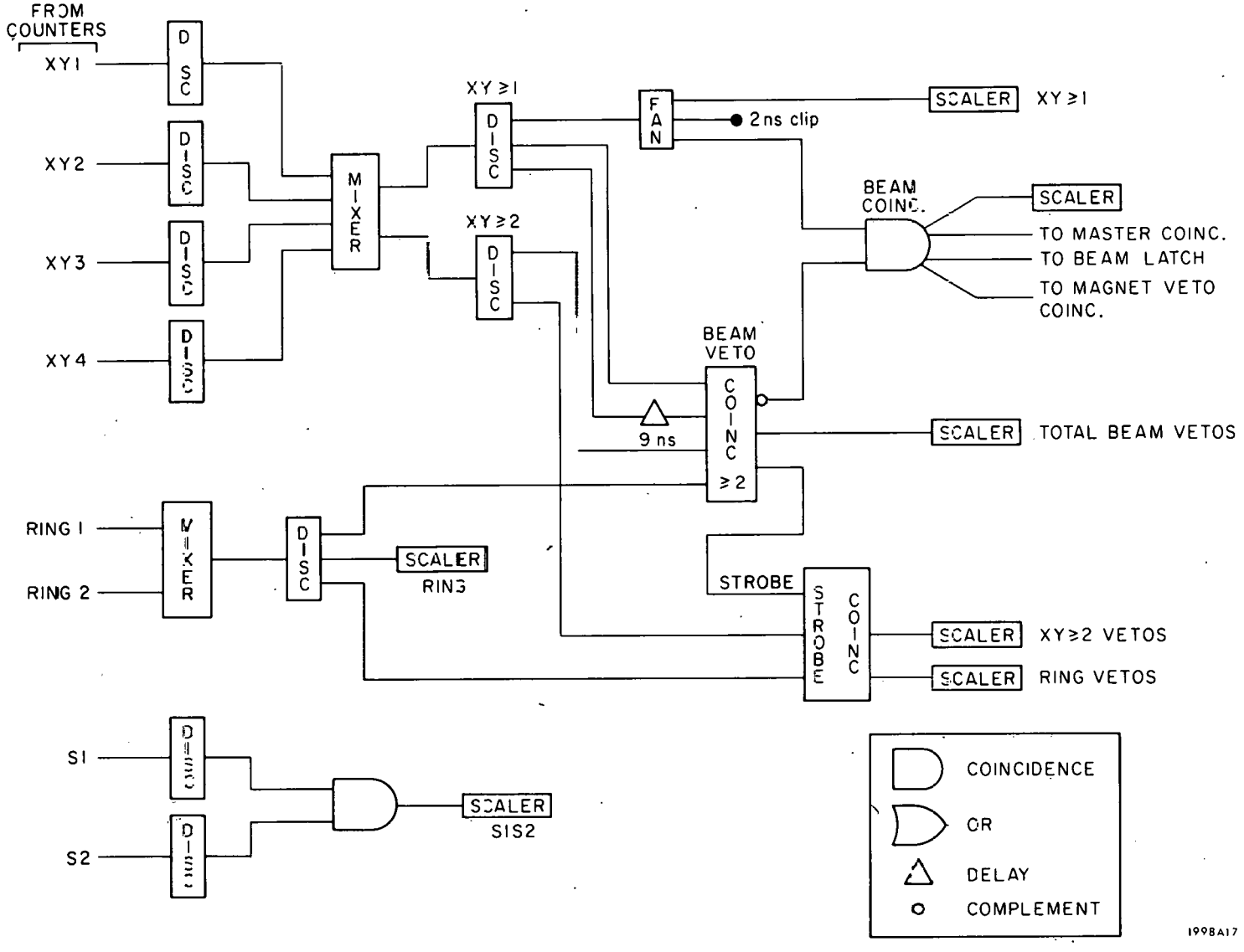

FIG. 5--Beam logic for generation of the incident particle ($\bar{a}$) pulse.

portion of the veto was developed by forming a coincidence of R with XY in a two-out-of-four majority logic unit which then vetoed any XY pulses which occurred in time. The (XY > 1) part of the veto was developed in two complementary ways. If two different quadrants of XY fired within ~ 6 nsec of one another, then XY ≥ 2 fired and the majority logic unit vetoed the XY count which occurred in time. If the counts were more than 6 nsec apart then the pulse of (XY ≥ 1) was lengthened to the duration of its input above threshold. It then overlapped with the same pulse which was delayed by 9 nsec at the majority logic input and once again the XY count was vetoed. If the particles were in the same quadrant of the XY counter, however, the majority logic was found to reliably veto only those particles which were more than ~11 nsec apart. Thus, the overall efficiency for correctly vetoing two particles which were within the ± 16-nsec window was ~ 83%. The remaining events with two incident particles were subtracted in the analysis stage by rejecting events with more than one particle in any of the beam hodoscopes.

The generation of the main event pulse is shown in Fig. 6. The discriminated outputs of the 20 HA and 34 HB counters were summed and discriminated for ≥ 1 and ≥ 2 particles. HA ≥ 1 (HB ≥ 1) was then put in coincidence with HB ≥ 2 (HA ≥ 2). These signals formed the input to an "or" circuit which gave $[(2A \cdot 1B) + (2B \cdot 1A)]$. The final event pulse was then formed by placing this signal in coincidence with the (π^-) signal while the summed output of the magnet counters served as a veto. After the occurrence of an event, the master coincidence was latched off for the duration of the machine pulse to allow the spectrometer system sufficient time to recover before accepting the next event.

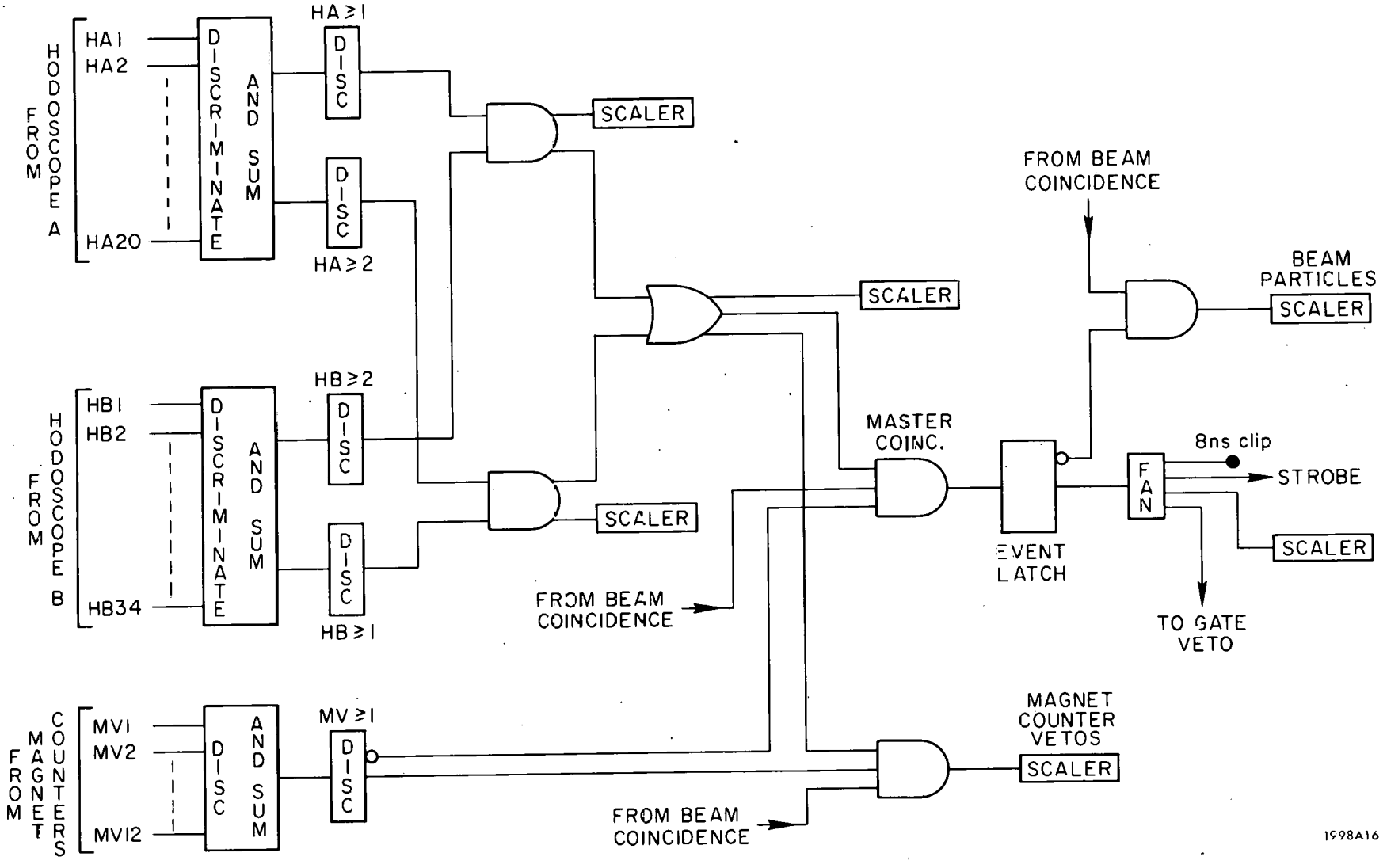

FIG. 6--Trigger logic for generation of the event (strobe) pulse.

The time delay in the generation of the event pulse was due in large measure to the necessary cable lengths in the system. These lengths were kept as short as possible by locating the fast electronics beside the analyzing magnet. The total delay time between an event passing through the triggering counters and full high voltage on the spark chambers was measured to be ~ 300 nsec.

The electronics were gated "on" in an 8-μsec window surrounding the machine pulse. The gate was depressed after the occurrence of an event in order to inhibit noise pickup from the spark chambers. However, the chambers were well shielded against rf noise emission and little pickup was noted even in the absence of this inhibit. Gates were also automatically inhibited if the computer was unready to accept the next event, or if there was a trip-out in the chamber high voltage or clearing field power supplies.

Important quantities from the electronics $\{$e.g., (π^-), $[(XY > 1)+(R)]$, Event$\}$ were scaled in the hardware to allow the performance of the electronics to be continuously monitored throughout the experiment. It should be noted that (π^-) was scaled twice because of its importance for normalizing the cross sections. A fast inhibit on (π^-) insured that no incident particles were counted in a pulse after the event had occurred.

H. Cerenkov Hodoscope

A large aperture (100" × 50") Cerenkov counter was placed behind the downstream set of spark chambers to identify the particles in the final state. The counter had a minimum path length of radiator of 70" and was filled with Freon 12 at pressures between 0 and 3 atm. Optically, it was designed such that each of the eight 25" × 25" mirrors reflected Cerenkov light into a corresponding light collection horn and phototube. The signals from each of these phototubes was integrated and the peak height of the integrated signal read by

the computer through an analog-to-digital converter and stored for each event. In addition, the signals from all the tubes were summed directly so that the Cerenkov information was available for triggering if desired. As a result of this design, the counter could be used either as a hodoscope of eight optically independent Cerenkov cells or, by utilizing the summed phototube output, as a large threshold counter with uniform efficiency across the aperture.

The counter was operated during this experiment at a gas pressure of 18.4 psia. The efficiency for detecting an 8 GeV pion at this pressure was > 99.8%. The threshold momentum for detecting a kaon was 9.2 GeV/c.

Detailed information on the construction and performance of this counter may be found elsewhere.[34]

I. Computer

An IBM 1800 computer was used for data read-in and logging. After receiving an event interrupt from the triggering electronics, the computer read out the contents of the counter buffers, the magnetostrictive scalers, and the Cerenkov counter analog-to-digital converters. At the beginning and ending of each experimental run, as well as periodically during a run, the computer also read the electronics and counter scalers and the excitation currents in the magnets. All of this information was written onto magnetic tape (about 400 tapes for the experiment).

In addition to its tape writing duties, the computer monitored the performance of the entire experimental system. Tracks were reconstructed for a subsample of events. The reconstructed tracks and spark coordinate positions could then be observed on a scope display. Counter performance was monitored by looking at histograms of counter singles rates. Spark chamber efficiencies and spark frequency tables allowed checks of the spark chamber system and

histograms of the tube pulse heights insured that the Cerenkov hodoscope was operating properly. The computer also checked the magnet excitation currents periodically but did not have direct control over them. Any needed magnet trimming was done manually.

The 1800 was able to present a few selected displays of important kinematical quantities (e.g., the effective mass of the two outgoing pions), but was not sufficiently powerful to carry out a complete on-line analysis. More complete analysis was available by means of an IBM 2250 remote scope terminal which was linked to the main SLAC computer, an IBM 360/91. A data link between the 1800 and the 360/91 gave this system a real-time capability. However, it was used mostly in an off-line mode, where finished tapes were taken to the 360/91 and analyzed under the control of the remote terminal. Thus, a rather complete analysis of systems performance was available with a short real-time delay. In addition, a complete set of kinematics histograms was available which allowed real-time decisions to be made on the basis of the observed data.

J. Data Collection

The data used in this thesis were collected at the Stanford Linear Accelerator Center in December 1969 and January 1970. These runs were preceded by several months of apparatus checkout at low repetition rates, which began in September 1969.

The major portion of the running time was devoted to a study of reactions in which two or more forward charged particles were produced in the final state by incident pions on protons. Emphasis was placed upon the study at an incident pion momentum of 15 GeV/c. Over 200 data tapes containing typically

35,000 events each were produced by the interaction of 8.582×10^8 incident particles. Other special runs were made to collect alignment data on the spectrometer system (see Chapter III) and data on $\pi^- p$ elastic scattering which was used as a check on the absolute normalization and is discussed in Chapter IV.

CHAPTER III

DATA RECONSTRUCTION

A. Chamber Alignment

The accuracy with which the angles and momentum of a track can be reconstructed depends on the precision with which the positions of the spark chamber planes are known. The spark chambers were optically aligned in the spectrometer system using standard surveying techniques. However, it is difficult by such methods to reach the required accuracy (0.005" - 0.010"). Such accuracy can be obtained by aligning the chambers using straight particle tracks. For this purpose, special alignment runs were made throughout the experiment. The data for these runs were taken by shifting the chambers on the precision chamber support system so that the plugs were no longer in the beam. The support system allowed the chambers to be positioned to an accuracy of better than 0.005" for horizontal shifts up to 5". The incident beam flux was then lowered to less than one pion per pulse to avoid overloading the chambers. The event trigger was set to record one track through the spectrometer and runs were made with the magnetic field both on and off.

Alignment was first performed using the straight beam tracks for which the magnetic field was set to zero. The position of each of the planes was defined to be the mean of the distribution of the distance between the measured track and the raw spark chamber coordinate (the deviation). The individual plane coordinate systems were then shifted until these deviations were centered at zero. Typical shifts from the surveyed positions were ~ 0.020".

When tracks with nonzero slope were studied after this alignment on straight beam tracks, the deviations were no longer centered at zero, but had

shifted systematically in opposite directions for tracks of negative and positive slope. This effect was consistent with the drift expected for the ionization electrons under the influence of the chamber high voltage pulse. In the ~100-nsec time interval between the application of the high voltage and the formation of the spark, these electrons drifted toward the high voltage plane with an average velocity of ~1" - 2"/μsec which typically caused a shift of ~0.020" in the position of the spark. The exact amount of this shift depended on the slope of the particle track. We corrected for this electron drift by shifting the apparent position of the high voltage plane ~1/2 of the gap width toward the ground plane. The deviation distributions were then well centered at zero, independent of the slope of the track.

Once the chambers were aligned for an experimental cycle (December or January), no further shifting of planes on a run-to-run basis was done. The deviations were very stable throughout an entire cycle, with a maximum shift in the mean of the deviations of $\leq 0.010"$.

B. Track Reconstruction

Off-line track finding and reconstruction were done using the same analysis package which was developed for use in the 360/91-1800 on-line system. After a new event was read from the tape, the raw chamber scaler readings were transformed to spark coordinate positions along the wand and these single spark coordinates were stored in a point bank. Coordinates in this bank were matched on a chamber-by-chamber basis and the resulting matched points stored in a matched point list. In order to understand this matching procedure, it should be remembered that each chamber contained 4 planes; conventional orthogonal planes in one gap (x-y) and planes inclined at angles of $\pm 30^{\circ}$ with

respect to the vertical in the other (η-ξ). It was therefore possible to determine which pair of x-y points belonged together by looping through all x-y combinations while checking to see if a particular combination was substantiated by either an η or a ξ point. Any such substantiated combination was called an x-y matched point. Matching in η-ξ was done in a similar fashion.

After the matched point lists were filled for all 7 chambers, another data bank was filled with lines which were the possible track candidates in downstream chambers. These lines were constructed by taking the x-y matched points from pairs of downstream chambers and forming all possible lines between them. The first and third downstream chambers formed one pair while the second and fourth chambers formed the other. Lines were constructed in a similar fashion using the η-ξ matched points, and combinations of x-y matched points in one chamber with η-ξ points in the other. Thus, 8 line lists were constructed in all.

The actual search for downstream tracks was carried out by taking each of the trial lines in turn and searching the downstream matched point lists to find those points which were within a certain tolerance of the trial line. If there were less than 3 matched points which fulfilled this condition, the line was rejected as a possible track candidate. Otherwise a least squares fit to these coordinates defined an "improved" line. A search was then made of the downstream coordinate points to find any additional coordinates which were within a distance ALLCOTOL from this line and a least squares fit was again performed. A search was then made to find the coordinate for each plane which lay within BESCOTOL of the new line and which was closest to it. A check was made to see if any spark coordinate had been gained or lost since the previous iteration. If not, the line was considered to be a good track. If

the spark coordinates had changed, a check was made to insure that the line had at least 6 planes. If it did not, the track was rejected. Otherwise, the points were least squares fit and passed through the BESCOTOL section again. This loop was repeated either until the spark coordinates were identical on two successive calls or a maximum of 5 calls was made. This least squares fit track was then rejected if more than one chamber had less than three planes with coordinates on the track. Otherwise, it was compared with all tracks which had been found previously for the event and was rejected as a duplicate if all of the spark coordinates were identical with those of a previously found track.

One of the primary functions of the iterative procedure described above was to force good tracks to converge to the same set of coordinates, irrespective of the trial line from which the search started. However, it was discovered that a substantial number of tracks was being found which differed by only a single coordinate. To alleviate this difficulty, each new track was sent through the entire track finding procedure,again starting with the ALLCOTOL analysis. Finally, the track was compared with the triggering hodoscope counters. Tracks which did not have a "live" hodoscope counter at each end were assumed to have occurred out of time with the triggering event. Magnet crossing was not attempted for these events.

In order to find tracks in the upstream chambers, the downstream track was projected forward through the magnetic field assuming that the track originated at the center of the target. This defined a line about which the ALLCOTOL-BESCOTOL loop was used. If a match was not found for each downstream track by this method, a new line was defined for input to the ALLCOTOL-BESCOTOL loop by projecting the downstream track to all points

in turn in the upstream chamber nearest the magnet. If still no track was found, the same routine was repeated using the middle upstream chamber. The ALLCOTOL-BESCOTOL loop used after a trial upstream line was established was essentially identical to that described previously and so will not be discussed here.

Once an upstream track was found, its projection was compared with that of the downstream track inside the magnet to determine if the two tracks in fact belonged together. This comparison was carried out in the nonbend plane (y-z) using four empirically placed focusing lenses: two inside the magnet and others at both the entrance and the exit of the magnet gap. If the positions of the projected tracks differed in y by more than PHICUT at the intersection point, the upstream track was rejected as the appropriate matching track and the search for the correct one was continued. A similar comparison of the upstream and downstream track matching was performed in the bend plane (x-z) by the same subroutine which calculated the particle momentum (see Chapter III.C). Once a matching track was found, the geometrical coordinates of both its upstream and its downstream portions were stored in a data bank where they could be accessed by later portions of the analysis program.

The above description of the reconstruction program corresponds to what was called the "slow" mode. This mode was used for carrying out some preliminary analysis of the data and also for the study of hodoscope efficiencies. However, the average computer CPU time necessary to analyze an event in this mode was ~ 55 msec. Since there was such a large number of events to be reconstructed, it was important to reduce the analysis time per event as much as possible.

Two major program modifications were made to this end. First, both the matched point and the line searches using η-ξ points were dispensed with and trial lines were established from only the x-y matched points. This greatly reduced the number of possible search combinations since the number of line lists was 2 rather than 8 as before. The track-finding efficiency was essentially unaffected by the change since the plane efficiencies of the chambers were extremely good. Second, instead of finding all tracks in the back and then keeping only those which were hodoscope-agreeing at both ends as was done above, "roads" were formed before the track search was begun. That is, bands were formed by connecting the edges of all "live" hodoscope A counters with the "live" hodoscope B counters. Points which were not within these bands were deleted from the point bank and thus were ignored in the subsequent track search. Taken together, these two program modifications cut the analysis time per event to $\sim$25 msec which was a reduction of about a factor of two.

C. Momentum Reconstruction

After track segments were found in both the upstream and downstream chamber packages, it was necessary to calculate the momentum of the charged particle which produced those track segments. If the Lorentz equation for the force is integrated along the path of the particle, we find the total change in momentum due to the magnetic field to be

$$\Delta\vec{p} = q\int_{\text{path}} d\vec{\ell} \times \vec{B} \quad . \tag{III. 1}$$

We define a right-handed coordinate system with the strong component of the dipole field along the y axis and the incident beam particle moving along the

positive z axis. The total momentum (p) of the particle is then given by

$$p = \frac{\Delta p_x}{\left(\frac{\ell_d}{\sqrt{1+\ell_d^2+m_d^2}} - \frac{\ell_u}{\sqrt{1+\ell_u^2+m_u^2}} \right)} \qquad \text{(III. 2)}$$

where $\ell = dx/dz$, $m = dy/dz$, and the subscript u(d) denotes tracks in the upstream (downstream) chamber package. Δp_x is the x component of Eq. (III. 1). Two problems now remain: (1) the calculation of Δp_x, and (2) the determination of ℓ_d and ℓ_u so as to minimize the error on p.

In order to obtain Δp_x, the field map is used to obtain a fit to $\int_{-\infty}^{\infty} B_y dz$ along constant lines in x and y. It is assumed that the magnetic field B_y is symmetric in x, y, and z so that the most general quadratic expansion which fulfills Maxwell's equations can be written as

$$\int_{-\infty}^{\infty} B_y dz = \alpha_1 + \alpha_2 (x^2 - y^2) \qquad \text{(III. 3)}$$

with α_1 and α_2 as fitting coefficients. If a power series expansion of the field map is now used, it can be shown that Δp_x becomes

$$\Delta p_x = -q \int_{\text{path}} \left[B_1 + B_2 (x^2 - y^2) \right] dz \qquad \text{(III. 4)}$$

with

$$\int_{-\infty}^{\infty} B_1 dz = \alpha_1$$

$$\int_{-\infty}^{\infty} B_2 dz = \alpha_2 \quad .$$

It should be noted that the $\int B_z dy$ term in Δp_x, has canceled with a term in $\int B_y dz$ to this order in the expansion.

Equation (III. 4) has a large α_1 term which represents the integral of the constant part of the B_y field and a remaining integral which depends on the path of the particle through the magnetic field. Since the magnetic field B_y is nearly constant over the whole gap, the second integral is a small correction to Δp_x and is calculated along a simplified trial orbit which is taken to be a parabola in the x-z plane for simplicity. Motion in the y direction is described by a straight line. Using the power series expansion of the field, it is then possible to derive an expression for the second term in Eq. (III. 4) which depends only on the coefficients of the expansion and on the coefficients of the trial orbit. In this way, we can avoid an integration through the magnetic field on a track-by-track basis and still calculate Δp_x with sufficient accuracy that it contributes insignificantly to the error in p.

Since tracks in the spectrometer have small angles in the y-z plane and since the error in Δp_x is small, the primary contribution to the variance of Eq. (III. 2) results from the uncertainty in ℓ_u and ℓ_d. If we assume for simplicity of calculation that all events are in the x-z plane and the small angle approximation is valid, then the variance of the momentum is given by

$$V(p) = \left(\frac{p^2}{\Delta p_x}\right)^2 \left[V(\ell_u) + V(\ell_d) - 2\,C(\ell_u, \ell_d)\right] \quad . \qquad \text{(III. 5)}$$

$V(\ell)$ is defined to be the variance of the quantity ℓ and $C(\ell_u, \ell_d)$ is the covariance of ℓ_u and ℓ_d. We wish to calculate the momentum in such a way that V(p) is minimized. We will, of course, get the smallest possible variance only if we use all of the available information. For tracks in the x-z plane this means that we must determine the upstream and downstream angles by using the constraint that the back and front tracks must join smoothly together inside the magnetic field. This can be done by fitting the lines in the spark chambers

using a constrained (1-c) fit. However, this requires precise tracking of the particle through the magnetic field and thus would require large amounts of computer time. There is, however, another method available which gives exactly the same results for the variance of the momentum and is much simpler to apply. We call this the "improved point-bound-vector" method.

The "point-bound-vector" method uses the slope and the intercept at the magnet center from the downstream chambers and a single point from the upstream track. From these quantities ℓ_u can be found which allows p to be calculated using Eq. (III.2). The point from the upstream track can be chosen in any fashion desired and it is of value to "improve" the "point-bound-vector" method by extrapolating the track upstream in order to minimize V(p). The final result for the variance can then be written as

$$V(p) = \left(\frac{p^2}{\Delta p_x}\right)^2 \left[V(\ell_u) + V(\ell_d) - \frac{\left[C(\ell_u, b_u) - C(\ell_d, b_d)\right]^2}{V(b_u) + V(b_d)} \right] \qquad \text{(III.6)}$$

where b_u (b_d) is the intercept of the upstream (downstream) track at the magnet center. This is exactly the same result which is derived from a constrained fit in the x-z plane.

D. Kinematics

After the vector momentum for each of the decay particles has been reconstructed, the kinematics of the event can be calculated. Invariant quantities are calculated using four-vector products in the standard manner. For example, the invariant mass of the dipion system in the reaction $\pi^- p \rightarrow \pi^+ \pi^- x^0$ can be written as

$$m_{\pi\pi}^2 = (p_1 + p_2)^2 = 2m_\pi^2 + 2E_1E_2 - 2|\vec{p}_1|\,|\vec{p}_2|\,\cos\theta_{\pi\pi} \,. \qquad \text{(III.7)}$$

E_1 (E_2) and $\vec{p}_1$ ($\vec{p}_2$) are the components of the four-momentum p_1 (p_2) of the outgoing pions and $\theta_{\pi\pi}$ is the decay angle between them. All of these quantities are directly measured by the spectrometer system.

Similarly the missing mass (M_{xo}) can be written as

$$M_{xo}^2 = (p_\pi + p_p - p_\rho)^2 = m_\rho^2 + m_p^2 + m_\pi^2 + 2m_p (E_\pi - E_\rho)$$

$$- 2E_\pi E_\rho + 2|\vec{p}_\pi| \cdot |\vec{p}_\rho| \cdot \cos \theta_{\pi\rho} \qquad \text{(III.8)}$$

where p_π (p_p) is the four-momentum of the incoming beam particle (target proton) and $p_\rho = p_1 + p_2$.

If only events from the reaction $\pi^- p \rightarrow \pi^+ \pi^- n$ are considered, there is an additional kinematic constraint in the problem because the mass of the missing particle is known. In order to make use of this constraint, cuts are made on the missing mass and target veto counters (see Chapter V.C). All events which pass these cuts are assumed to have a missing neutron, which constrains $|\vec{p}_\pi|$ in terms of $|\vec{p}_\rho|$. This constraint is most important for calculating the momentum transfer. Instead of the usual form $t = (p_\pi - p_\rho)^2$, we have

$$t \approx t_{min} - p_\perp^2 \quad . \qquad \text{(III.9)}$$

t_{min} is the smallest kinematically allowed momentum transfer which can produce the observed dipion mass. It is independent of the scattering angle of the dipion and is extremely small for $\pi^+ \pi^- n$ events at 15 GeV/c. Hence, the resolution in t is dependent only on the accuracy of the measurement of $p_\perp$ which is strongly dependent only on the measurement of the angles in the beam and the front chamber package. This leads to a much better resolution in t than is possible using the standard four-momentum calculation (see Chapter IV.A).

E. Data Summary Tapes

A data summary tape (DST) was a magnetic tape volume which contained the important geometric and kinematic variables for each of the produced events corresponding to a particular reaction. For example, in order to study $\pi^+\pi^-$n events, a tape was prepared which contained all events of the type $\pi^- p \rightarrow y^o x^o$ where x^o denotes the missing particle ($M_{x^o} \leq 1.5$ GeV) and y^o denotes the zero charged state which decays into the two charged particles measured by the spectrometer. Pions were then selected by imposing a Cerenkov counter cut. The inclusion of higher missing mass states allowed the study of nonneutron background in the missing mass as will be discussed in Chapter V.E.

The data summary tapes were created as the final step in a three-stage data reduction process. The raw data events were first analyzed to determine if they contained two or more good tracks in the rear chambers. Those that did not were rejected. With this criterion, the number of data events was reduced by approximately a factor of 3 in $\sim$64 hours' use of the 360/91. The number of events was reduced still further on a second set of tapes which contained only those events with two or more tracks which crossed the magnet. This required $\sim$25 hours' use of the 360/91. The event records of these "geometry" tapes contained the total reconstructed geometry and kinematics of the accepted events. A DST for any particular reaction could then be written by utilizing these geometry tapes.

As examples of the information contained on a DST and as samples of the raw data, we present three graphs. Figure 7 shows the invariant mass spectrum for the $\pi^+\pi^-$ events produced in the reaction $\pi^- p \rightarrow \pi^+\pi^- x^o$. The dominant feature is the copious ρ^o production. There is also a sharp peak near

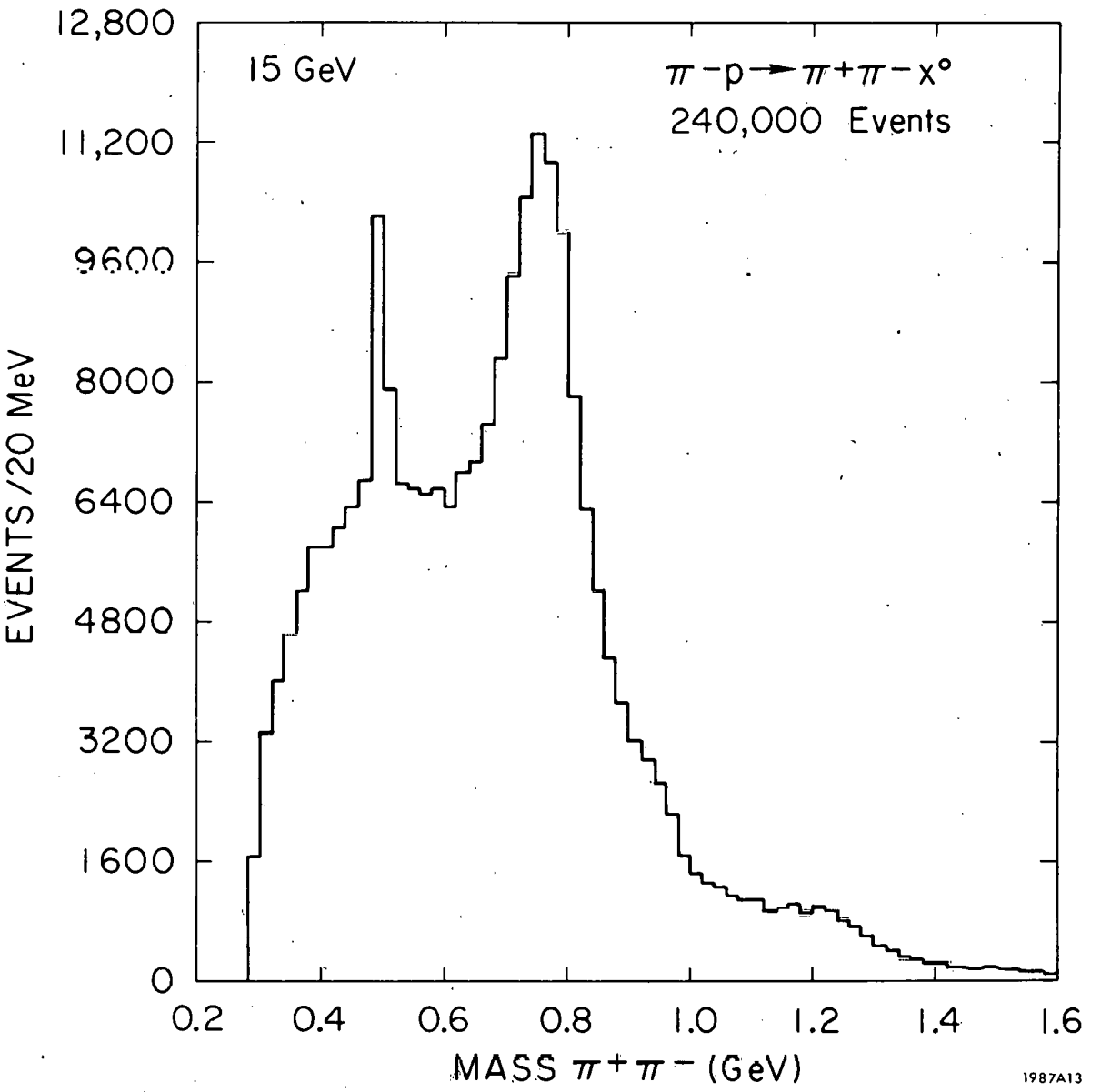

FIG. 7--$\pi^+\pi^-$ invariant mass spectrum for all missing masses.

500 MeV from the decay $K^o \rightarrow \pi^+\pi^-$. The shoulder at approximately 1200 MeV is suggestive of the f^o which is strongly suppressed by the acceptance of the spectrometer. The relative height of the f^o peak can be increased somewhat by restricting the missing mass to the region of the neutron ($0.8 < M_{xo} < 1.06$ GeV) as shown in Fig. 8. The background underneath the ρ^o and the K^o peak has been reduced substantially. Some K^o signal still remains from the reactions $\pi^- p \rightarrow K^o\Sigma^o(\Lambda^o)$ since the missing mass resolution is $\sim$85 MeV (see Chapter IV.A).

In Fig. 9, we present the missing mass for the reaction $\pi^- p \rightarrow \rho^o x^o$ ($0.665 < m_{\rho o} < 0.865$ GeV). Clear neutron and Δ^o signals are observed as well as a higher missing-mass bump around 1700 MeV. The distribution for higher missing mass states is smooth and extends above 4 GeV.

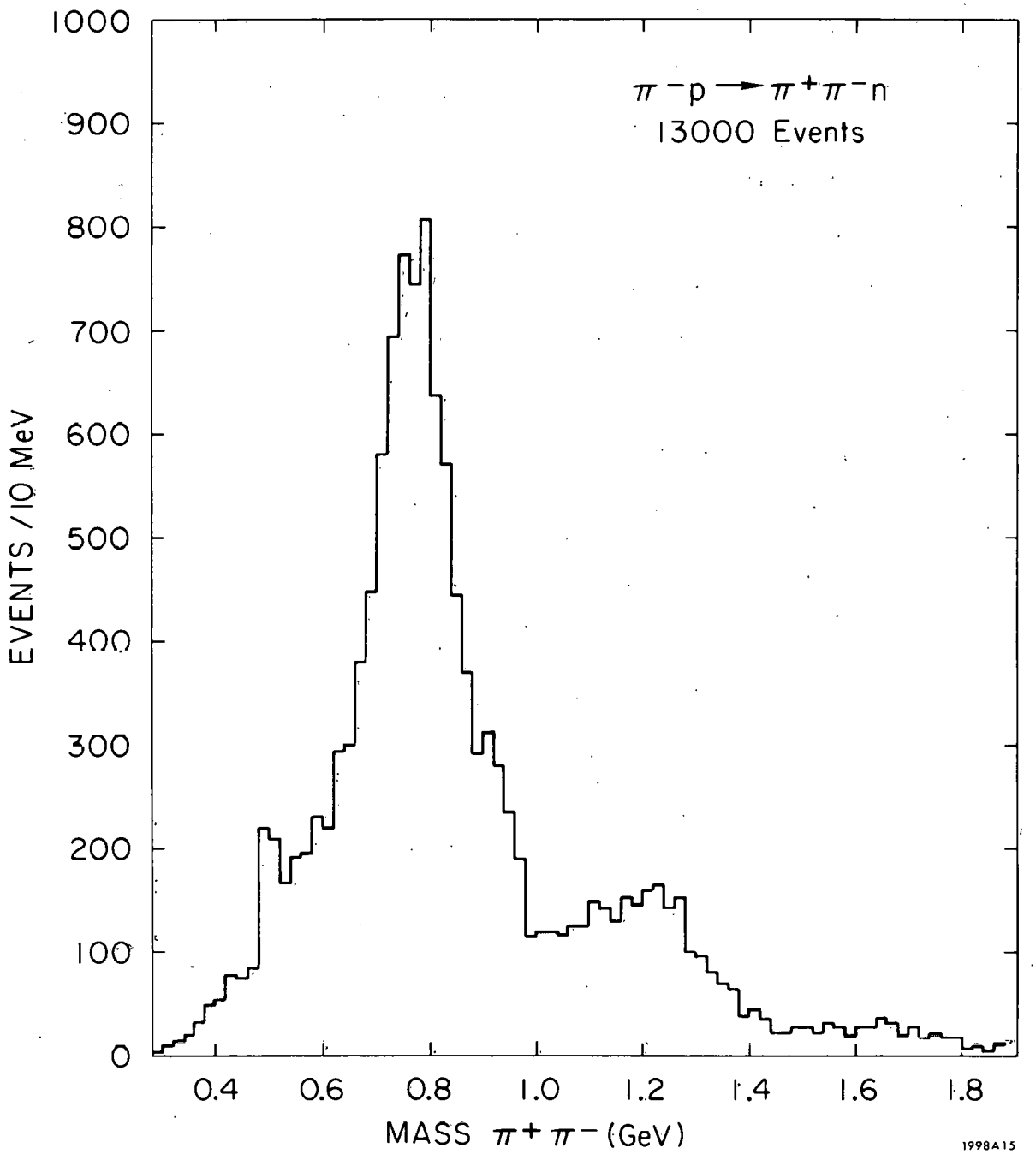

FIG. 8--$\pi^+\pi^-$ invariant mass spectrum for $\pi^+\pi^-$n events.

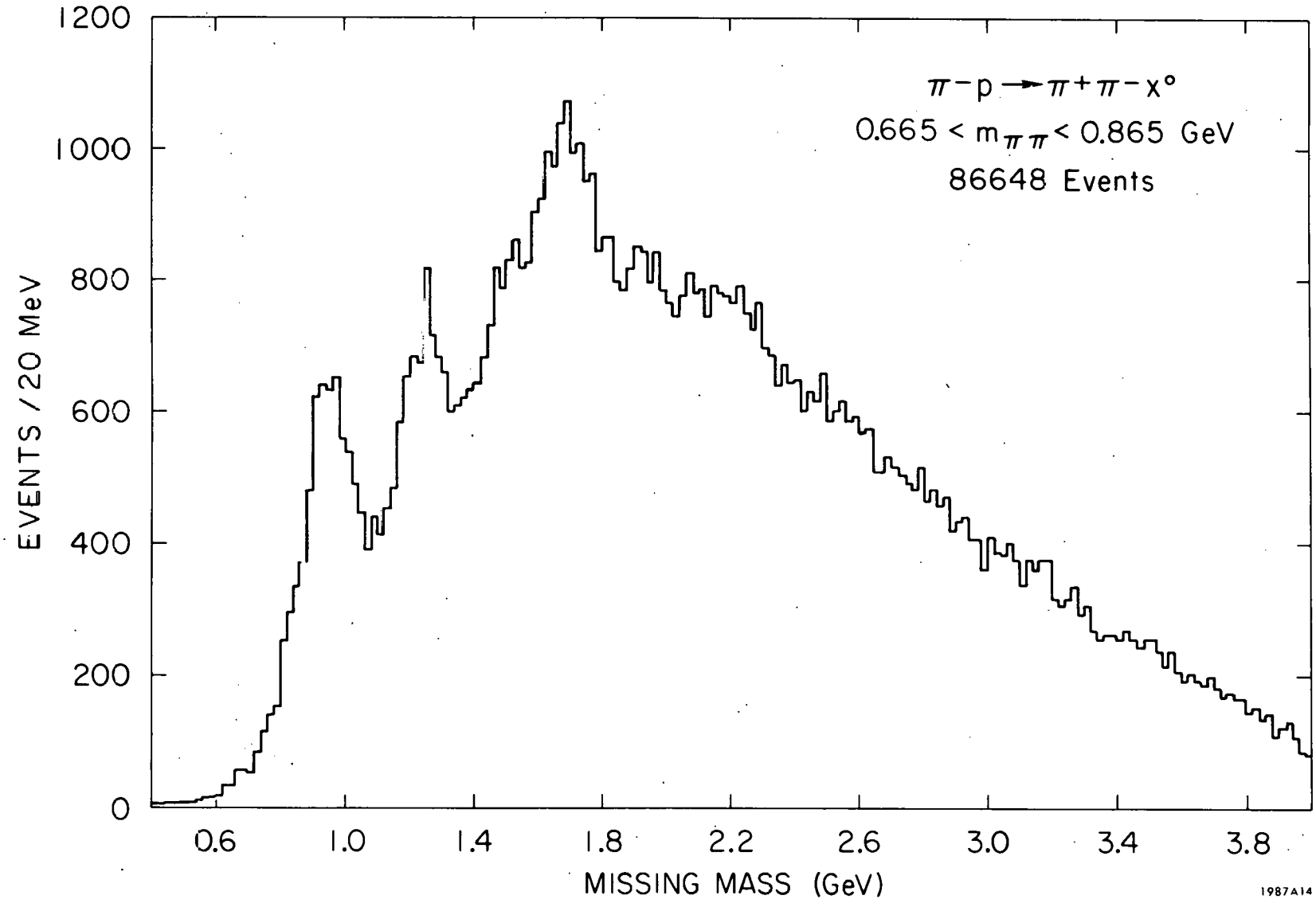

FIG. 9--Missing mass (M_{X^0}) spectrum for the reaction $\pi^- p \rightarrow \pi^+ \pi^- x^0$, $0.665 < m_{\pi\pi} < 0.865$ GeV.

CHAPTER IV

SPECTROMETER PERFORMANCE: NORMALIZATIONS AND RESOLUTIONS

A. Scale Calibrations and Resolutions

Good knowledge of the absolute invariant mass scale and of the mass resolution was necessary in this experiment because the ρ-ω interference parameters were rather sensitive to the precise values. These numbers were obtained by observation of the decay $K^o \to 2\pi$ which was produced in the reactions $\pi^- p \to K^o \Lambda^o(\Sigma^o)$.

In Fig. 10, we show the $\pi^+\pi^-$ mass spectrum in the K^o region for a missing mass between 0.98 and 1.28 GeV. The data are restricted to K^o decays which occur inside the target volume so that a contribution from multiple scattering is included. The line is a fit to a Gaussian resolution function plus a linear background term. The K^o mass and the mass resolution of the apparatus are given by

$$M_{K^o} = 497.4 \pm 1.0 \text{ MeV}$$

$$\sigma_{K^o} = 6.5 \pm 1.0 \text{ MeV}$$

where the given errors include conservative estimates for the systematic effects. This compares with the accepted K^o mass value[35] $M_{K^o} = 497.79 \pm 0.15$ MeV.

There were sufficient kaons available that K^o mass distributions could be fitted in 5 - 10 run blocks in order to check for any systematic shift in the mass scale during the experimental run. No shifts were observed other than those due to the small changes in the magnetic field, which were measured by

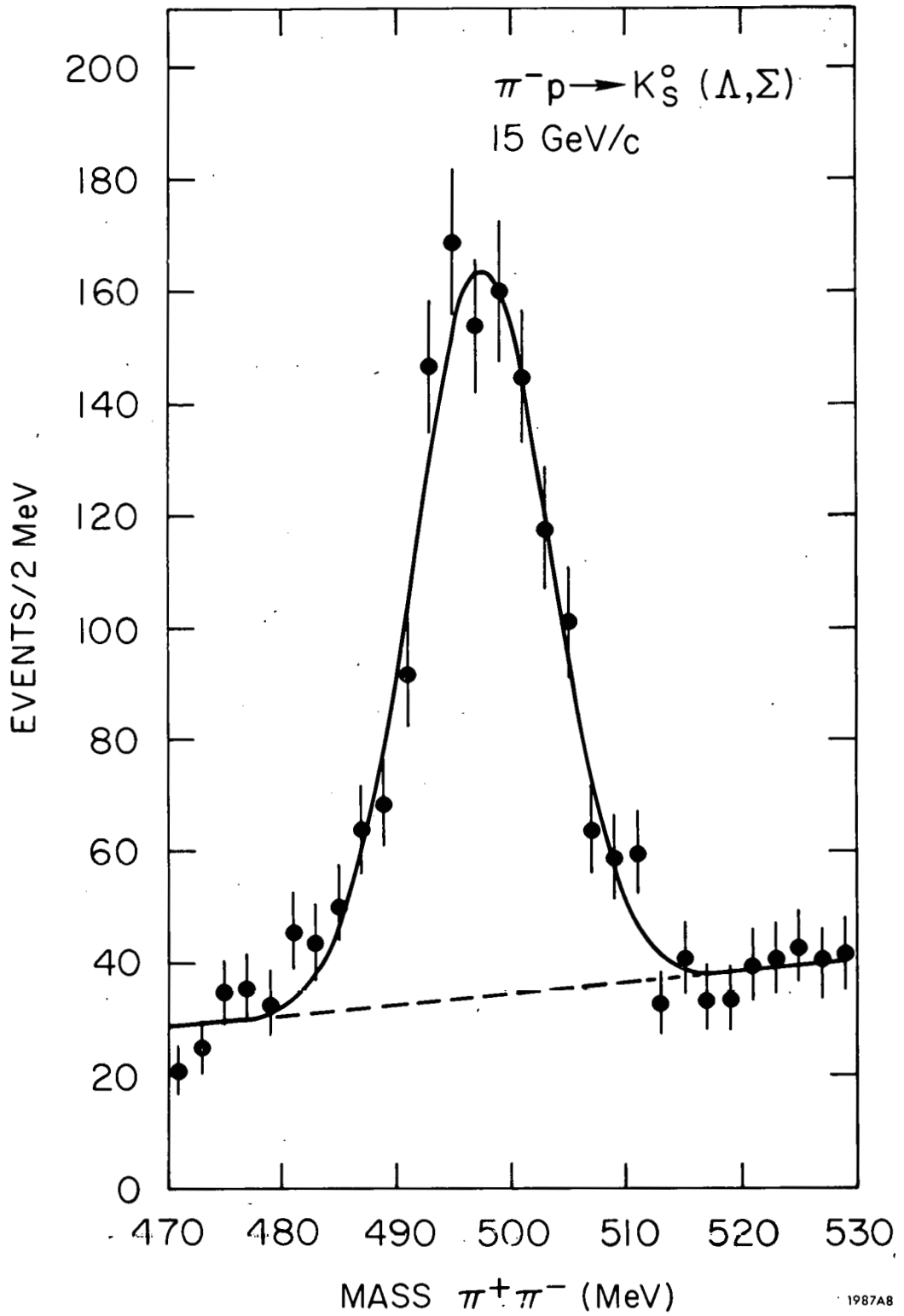

FIG. 10—Invariant mass spectrum for $\pi^+\pi^- x^o$ events in the K^o region with $0.98 < M_{x^o} < 1.28$ GeV.

the Hall probe and the NMR detector (Chapter II.E). Therefore, we concluded that the mass scale was stable throughout the experiment.

Because the ρ^o decays with a larger angle between the pions in the lab than does the K^o, the mass resolution in the ρ^o region is degraded. In addition, the average multiple scattering for the ρ^o is somewhat larger since the decay pions travel through a larger fraction of the target hydrogen on the average. Taking these effects into account, a 6.5 MeV resolution at the K^o corresponds to $\sigma \approx 8$ MeV for $\pi^+\pi^-$ masses in the region of the ρ^o.

The absolute value of the incident beam momentum was not well known prior to the experiment. Its value was determined by centering the neutron peak at ~ 940 MeV. The experimental missing mass resolution for the reaction $\pi^- p \to \rho^o x^o$ was obtained from the width of the observed neutron peak when no target veto counters fired as shown in Fig. 14(c). This gave a missing mass resolution of $\sigma_{x^o} = 85 \pm 5$ MeV. It should be noted that the resolution in mass and missing mass were also calculated by propagating the errors on (1) the incident beam particle vector momentum, (2) single spark chamber plane coordinate position, (3) and multiple scattering in the target and hodoscopes. The results of this calculation agreed with the experimental observations within a fraction of the quoted error.

The resolution in t was determined primarily by the resolution in angle of the incident and final state particles [see Eq. (III.9)]. Its value was calculated to be

$$\sigma_t = 0.03 \sqrt{-t}$$

which corresponds to a resolution of $\sigma_t = 0.0011$ (GeV/c)^2 for our smallest t bin ($t_{min} < |t| < 0.0025$).

B. Normalization

In order to calculate cross sections, it was necessary to correct for beam and event loss in the system. Some of these corrections (e.g., the triggering hodoscope efficiencies) were dependent on the position of the event in the spectrometer and were included in the Monte Carlo efficiency program which will be discussed in Chapter V. Other corrections (e.g., beam losses) were nearly independent of the actual topology of the final event and could be included by simply multiplying the cross section by the appropriate factor. We discuss this class of corrections here. In this discussion, we will use a correction factor (CF) which is defined as the ratio of the corrected cross section to the measured cross section.

1. Pion-Beam Contamination

As has been discussed previously, the contamination of the pion beam by muons was measured during the experiment by a muon telescope. Upper limits on the contamination by other particles were very small so their contribution was ignored in the multiplicative term. However, uncertainties in the knowledge of the actual value of these contributions were included in the estimation of the error. The result was

$$CF = 1.04 \pm 0.004 \quad .$$

2. Bad Bits

An event was said to contain "bad bits" if one or more of the beam hodoscopes had either zero or two or more "live" counter bins. Such events could not be included in the analysis since the kinematical variables of the incoming beam particle were not well known. Therefore, the incident beam flux also had to be corrected by subtracting the number of beam particles which had associated bad bits. This number was not directly measured so it was

estimated from the data by assuming it to be given by the fraction of all two-track events which had bad bits. A small ($\sim 2\%$) correction was then applied for the efficiency of the two-particle veto in the XY counter. The validity of this assumption was checked by comparison with bad bits rates in the elastic scattering runs where the triggering conditions were quite different. The magnitude of the correction changed only slightly under these different running conditions and the differences were included in the estimate of the error. The resulting correction factor was

$$CF = 1.095 \pm 0.012 \quad .$$

3. Delta Rays in Magnet Veto

Since the counters lining the magnet pole faces were a veto on the trigger, any event accompanied by a delta ray which entered these counters was not recorded. In order for a delta ray to reach the veto counters, it needed to have sufficient energy (E_{min}) to escape the target and reach the magnet gap, but insufficient energy (E_{max}) to pass through the magnetic field. The number of events with such an accompanying delta ray was calculated using a simple model in which any delta ray which passed into the magnet gap with energy between E_{min} and E_{max} was assumed to have vetoed the event. The result of this calculation was

$$CF = 1.012 \pm 0.005 \quad ,$$

where the error was estimated from the uncertainty in the model.

4. Absorption in the Spectrometer

Absorption in the spectrometer was calculated assuming that the absorption cross section for heavy material scales from the hydrogen cross

section by $A^{2/3}$. Including an estimate of the systematic error in this assumption, we find that

$$CF = 1.044 \pm 0.015 \quad .$$

5. Pion Decay in the Spectrometer

The loss due to the decay of pions in the final state was calculated assuming that the event was lost if the decay muon had either a momentum or an angle which would have caused the spectrometer system to measure the missing mass to be outside the missing mass cut. This calculation yielded

$$CF = 1.022 \pm 0.010 \quad .$$

6. Vertex Cut

In order to reject badly measured events, a cut was placed on events whose vertex lay outside the fiducial volume of the target cell. An estimate of the fraction of good events which were also discarded by this cut was made by a hand fit to the experimental vertex distribution which gave

$$CF = 1.018 \pm 0.003 \quad .$$

7. The Empty Target

The empty target rate was extremely small because only events whose vertex lay inside the target cell were considered in the analysis. The correction factor was

$$CF = 0.992 \pm 0.001 \quad .$$

8. Magnet Crossing

During the track reconstruction program, projected upstream and downstream tracks were required to match to a given tolerance at the center of the magnet, thus causing the loss of some good events. From the experimental

histograms of the distance between matched tracks, it was concluded that

$$CF = 1.02 \pm 0.01 \quad .$$

9. Track-Finding Inefficiency

Track losses due to the measured spark chamber inefficiency were included in the Monte Carlo. It was discovered, however, that these efficiencies did not accurately reproduce the total decrease in event yield which was observed when the chambers were not operating at peak efficiency. Moreover, tracks could also be lost from other causes such as algorithm inefficiency. The magnitudes of these track finding inefficiencies were estimated directly by the hand scanning and reconstruction of events and by studies of the variation in the number of tracks found as conditions changed throughout the experiment. The correction factor thus obtained compared well with that derived from the elastic scattering measurements in which spark chamber and reconstruction efficiencies were calculated in an independent manner. The result was

$$CF = 1.080 \pm 0.045 \quad .$$

10. Two Tracks Interpreted as Three

As mentioned previously in the discussion of the analysis program, the track finding program periodically found two tracks which differed by only one or two sparks. Since only two track events were analyzed, any such three track events were rejected. This required a correction factor of

$$CF = 1.028 \pm 0.002 \quad .$$

11. Pion Absorption in the Target

Pion absorption in the target was included in the efficiency Monte Carlo (see Chapter V.B). However, we include an estimate of the systematic error

on the calculation so that

$$CF = 1.000 \pm 0.030 \quad .$$

12. Efficiency Monte Carlo

The normalization error due to unknown systematic effects in the Monte Carlo was estimated from the amount the normalization shifted when a fairly serious known mistake (such as an incorrect target vertex distribution) was made in the efficiency calculation. This gave

$$CF = 1.000 \pm 0.02 \quad .$$

13. Summary

Multiplying all of the above factors together and combining the errors gave

$$CF = 1.410 \pm 0.085 \quad .$$

The average density of the liquid hydrogen in the target was 0.0694 gm/cm^3 with an absolute error of $\lesssim 1/2\%$. There were 8.582×10^8 incident pions at 15 GeV, so that one 15 GeV event produced at the target corresponded to a cross section of

$$0.000387 \pm 0.000023 \quad \mu b/\text{event}$$

which corresponds to a $\sim 6\%$ normalization error.

In calculating the error above, the individual errors (1-13) have been combined in quadrature. A priori, this is not well justified though it is difficult to find an approach which seems any more reasonable. As an indication of the possible variation in the error estimate which would be made if a different combinatorial technique were used, we note that if the errors are summed linearly, we find an error of $\sim 16\%$. This estimate is probably an upper limit on the error given the individual estimates.

In the remainder of this thesis, the quoted normalization error will be the one derived by combining the errors in quadrature. However, the uncertainties in this procedure should be remembered.

In order to derive cross sections for specific reactions such as $\pi^- p \rightarrow \pi^+ \pi^- n$, it was necessary to include corrections for the missing mass resolution, and estimates of competing background processes. These points will be discussed in more detail in Chapter V. For reference purposes, we simply note here that there was a nonneutron background of $12 \pm 2\%$ with an additional 2% error for the uncertainty in the missing mass resolution. Therefore, one $\pi^+ \pi^- n$ event corresponded to

$$0.000340 \pm 0.000023 \quad \mu b/\text{event} \quad .$$

C. Elastic Scattering

In order to check the behavior of the experimental apparatus and the data reconstruction programs, it is useful as a comparison to study a reaction which has been exhaustively studied in previous experiments. In order to be a complete check, this reaction would ideally be topologically similar to the reaction $\pi^- p \rightarrow \rho^0 n$; and its normalization, differential cross section, and density matrix elements would be well known. Such a reaction would check the normalization corrections and analysis programs, and would also allow a direct study of any biases which might be present as a function of spatial position or momenta of the event tracks.

Unfortunately, in this imperfect world there exists no reaction at 15 GeV which fulfills all of these conditions. However, the differential cross section for the elastic scattering of negative pions from protons[36] is known to an absolute systematic accuracy of better than 1%, and its measurement is thus an excellent check of many important normalization corrections even though

it does not check all parts of the system. In particular, elastic scattering directly checks the normalization corrections which must be made for the following:

1. electronics and triggering inefficiency,
2. spark chamber and hodoscope inefficiency,
3. beam contamination by muons and other particles,
4. beam counter corrections (bad bits),
5. track finding algorithm.

It also checks the general methods by which corrections which are similar but nonidentical in the two reactions are derived. In addition, such a measurement indirectly checks the complete experimental apparatus and thus gives one confidence that the general properties of the system are well understood.

Elastic scattering data were taken during both December 1969 and January 1970. The trigger for this measurement was

$$(XY) \cdot \left[\overline{(XY>1)+(R)}\right] \cdot (1A \cdot 1B) \cdot (\overline{MAG}) \cdot (\bar{L}) \quad .$$

That is: one and only one beam particle; at least one track following the magnet; no particles intersecting the magnet pole faces; and no signal from the lollipop (L). The lollipop was a circular 5" diameter counter placed directly behind the B hodoscope to veto out beam particles and small-angle scattering. The remainder of the experimental arrangement was unchanged. To insure that the beam electronics and scaling systems were properly checked, the incident-pion flux was unchanged from that of the preceding normal data runs ($\sim$ 10 pions/pulse at 180 pps). The average triggering cross section was 6.68 mb and the total real time expended for the collection of the data presented here was $\sim$1-1/2 hours. The empty target background was typically

10% but became as large as 20% at the smallest value of t. Several empty target measurements were made to insure a reliable subtraction of this background.

Since the primary motivation for the measurement was to check the normalization corrections for the apparatus, the elastic differential cross section was measured in the region where the geometrical acceptance was 100% with the edges of the acceptance region being defined by the magnet aperture for large scattering angles and by the lollipop counter for small angles. This negated any dependence of the final cross section on an acceptance Monte Carlo. However, scattered tracks in this momentum transfer region go through the dead spot in the front chambers, so the analysis was done utilizing the angle and position of the track in the rear chambers only.

Tracks were reconstructed in the back chambers using the standard analysis package described in Chapter III. B. Good events were required to have one and only one hodoscope-agreeing track. This removed background scatterings which had occurred out of time with the trigger pulse and also rejected a part of the inelastic background. Using only the angular information from the beam hodoscopes and the back chambers, the scattering angle and the momentum of the scattered pion were calculated under the hypothesis that the event was elastic. Using the calculated momentum, the actual track in the back chambers was projected upstream and compared with the position of the incident beam particle at the target. The distribution of distances between the projected track and the incident beam particle is shown in Fig. 11. In general, the elastically scattered events are expected to be in the peak corresponding to a close approach between the projected track and the incident beam particle. Inelastic background may thus be rejected by cutting out those

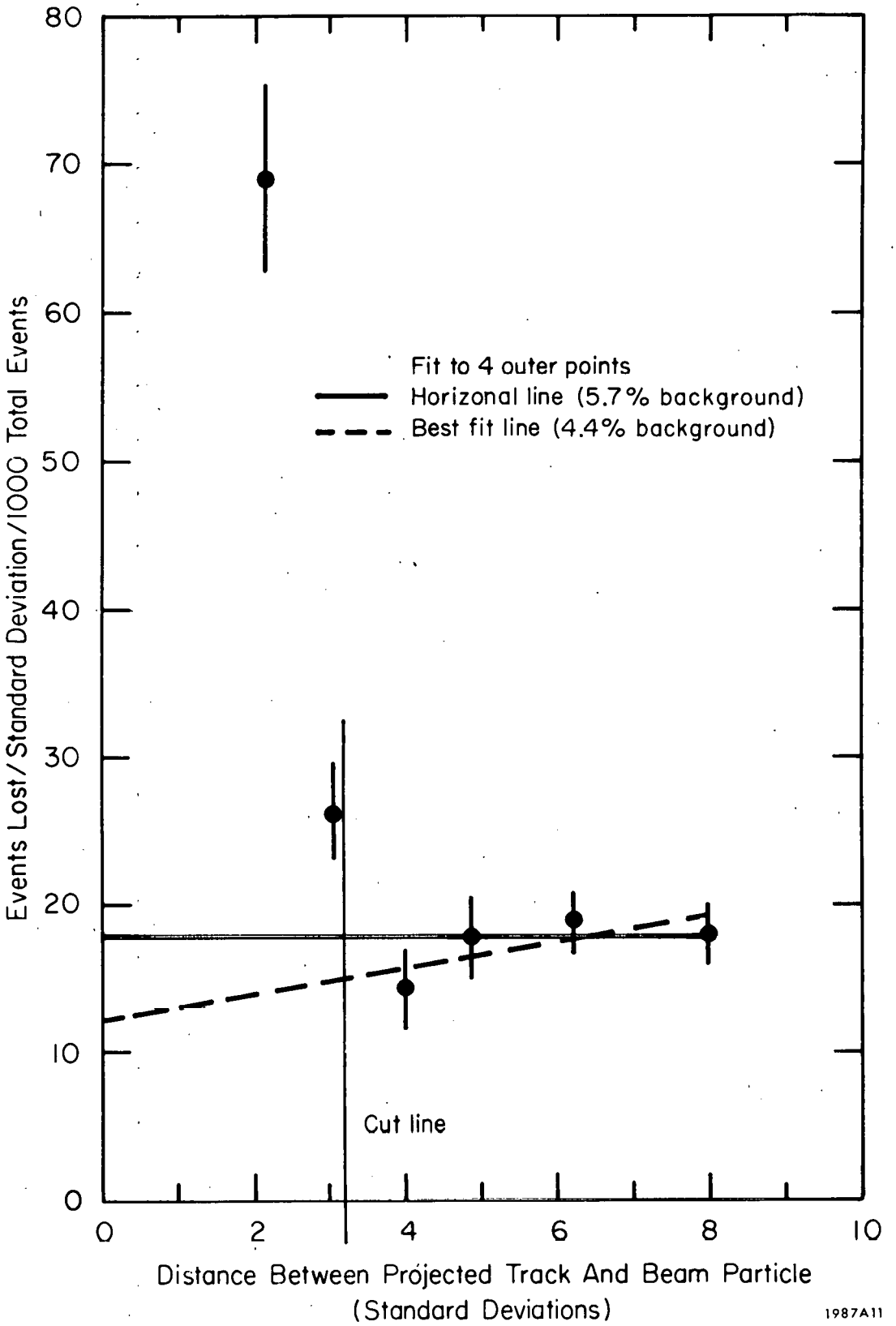

FIG. 11--Distribution of the distance between the projected elastic track and the beam particle at the target center.

events which lie outside a cutoff in approach distance as shown by the vertical line in Fig. 11.

Additional inelastic event rejection is possible by utilizing the target-veto hodoscope. Since the elastically scattered proton or accompanying delta rays can count in the inner target counters, one cannot demand zero particles in the hodoscope. However, for $-t < 0.22$, the proton does not have sufficient energy to penetrate the lead between the inner and outer layers of the hodoscope. Thus, any event which had one or more particles in the outer counter was rejected. The efficiency of this cut was determined from studies of the target veto which were carried out using the reaction $\pi^- p \rightarrow \rho^0 x^0$. These studies showed that the above cut eliminated $\sim 60\%$ of the background in the N*(1236) region and a larger fraction of the higher missing mass states.

An estimate of the inelastic background remaining after these cuts had been applied was obtained in two independent ways. First of all, it was noted that Fig. 11 is equivalent to a missing-mass-squared spectrum for the reaction $\pi^- p \rightarrow \pi^- x^+$. By means of a Monte Carlo program, it was shown that the 1σ point of Fig. 11 corresponds to a resolution in the missing mass squared ($M^2_{x^+}$) of ~ 500 MeV^2. The cut of 3.2 standard deviations in the vertex distance which was made to reject inelastic events was thereby shown to be equivalent to requiring $M^2_{x^+} \leq 2.5$ GeV^2. An estimate of the background remaining inside this cut was then made on the basis of published data[37] for the reaction $\pi^- p \rightarrow \pi^- x^+$ at 16 GeV/c. Cross sections for reactions with four or more pions in the final state were small and were also effectively vetoed by the target-veto hodoscope, so they were ignored. The measured slopes of the differential cross sections for the background reactions were sufficiently similar to the elastic that the estimates were made on the basis of the total cross sections.

The background cross section was estimated to be 0.143 mb which, when compared to the elastic cross section of 4.36 mb, implied a residual inelastic background of 3.3%.

An estimate of the background was also made from the experimental data. Since the missing mass resolution was so broad, the number of background events as a function of missing mass squared was expected to be nearly constant over a rather wide interval. Consequently, the background was estimated by straight-line extrapolations underneath the elastic peak using the outer four points in Fig. 11. The constant height extrapolation gave 5.7% whereas a best-fit straight line gave 4.4%. No statistically significant variation in the background was noted as a function of t. However, as noted above, the t slopes for the background reactions were only slightly flatter than that of the elastic and a statistically significant variation in the background was not expected across the observed range of momentum transfer.

Considering the uncertainties implicit in the calculations, the agreement between the two methods of estimating the background was quite encouraging. For calculation of the normalization of the elastic cross section, a background of 5% ± 3% was assumed.

Most of the normalization corrections needed here were similar to those needed for normalizing $\pi^- p \rightarrow \rho^o n$ and were discussed in Section B. An additional correction was necessary for the deadtime in the lollipop counter. Whenever two particles were present in the system simultaneously, the system would not trigger on the scattering of either of them since the other would count in the lollipop and veto the trigger. Thus, an inefficiency in the hardware rejection of two simultaneous beam particles was directly reflected as

a normalization bias. This effect was estimated directly from the data and was also calculated on the basis of observed counting rates to be $\sim 4\%$.

The absolute elastic differential cross section at 14.96 GeV/c is shown in Fig. 12. Coulomb scattering was $< 1\%$ of the measured cross section at the smallest t value. For comparison purposes, the points of Foley et al.,[36] are shown on the same graph. The points were scaled from 16 GeV/c by the formula

$$\frac{d\sigma}{dt}(p_2) = \left[\frac{\sigma_{TOT}(p_2)}{\sigma_{TOT}(p_1)}\right]^2 \frac{d\sigma}{dt}(p_1)$$

which has been shown to work extremely well.[36] The systematic normalization error in the points of Foley et al. is $\sim 1\%$ while the normalization error of this experiment is estimated to be $\sim 6\%$ where the normalization errors have been combined in quadrature as discussed in Section B. To make any possible systematic effects evident, the errors shown are statistical. The agreement in normalization is clearly extremely good. There is a hint that the slopes differ slightly as might be expected since the inelastic background was not subtracted as a function of t. Overall, however, the agreement is quite remarkable and lends strong support to the thesis that the normalization corrections are well understood.

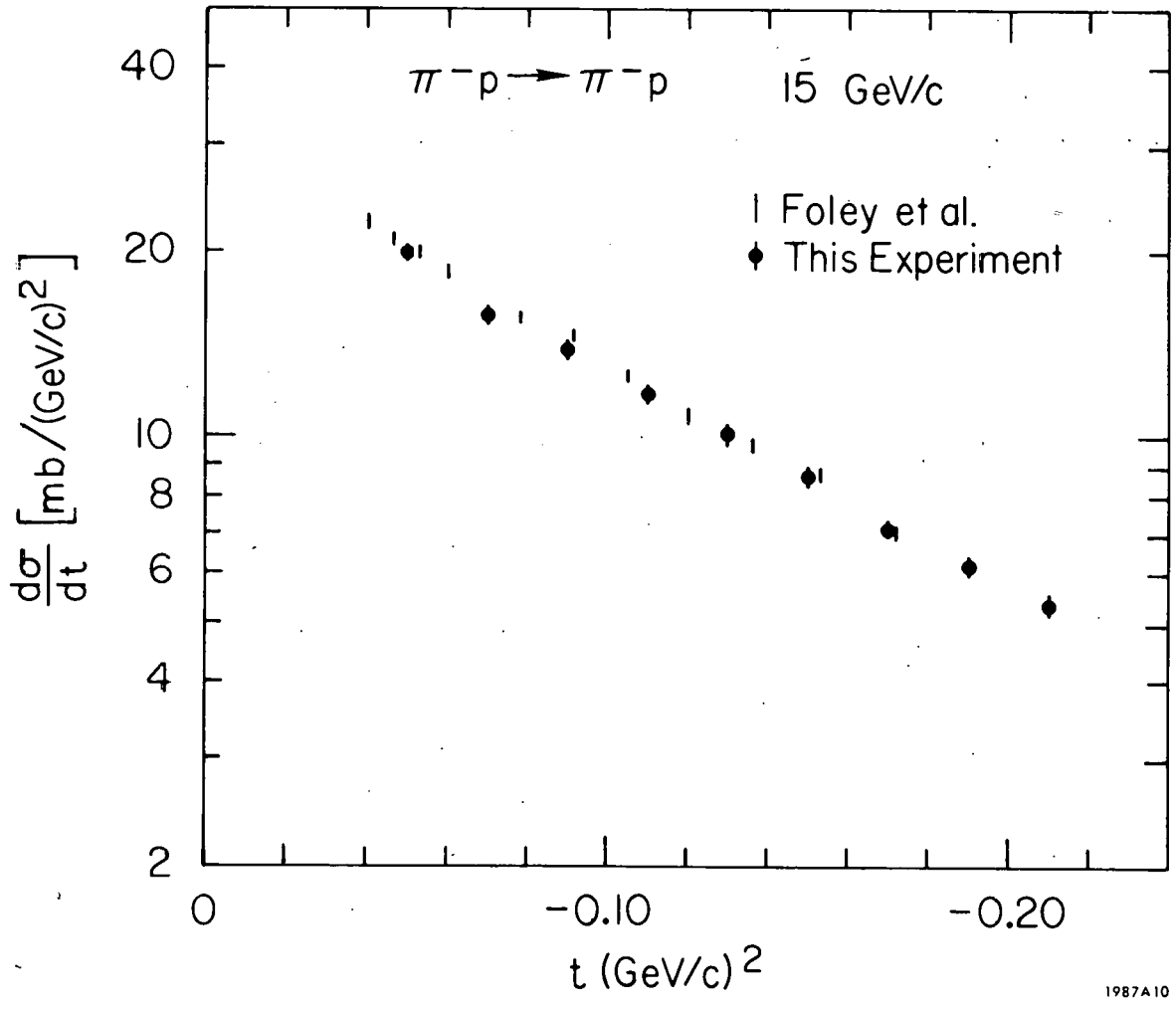

FIG. 12---A comparison of $d\sigma/dt$ ($\pi^- p \rightarrow \pi^- p$) measured in this experiment with the data of Foley et al.

CHAPTER V

ANALYSIS

A. The Method

The central problems in the analysis are the determination of the spin density matrix elements (ρ_{ij}) and the differential cross section ($d\sigma/dt$) in the region of the ρ^o for the reaction,

$$\pi^- p \rightarrow \pi^+ \pi^- n . \qquad (V.1)$$

These quantities can be directly obtained from the angular distribution and t spectrum of the dipions which are produced at the target. However, because the spectrometer system subtends only a fraction of the solid angle surrounding the target, the experimentally observed data (O) is actually given by the product of the detection efficiency of the spectrometer (E) and the produced dipion spectrum (D). This is,*

$$O = E \cdot D \quad . \qquad (V.2)$$

The quantities in Eq. (V.2) are functions of all the experimentally important kinematical variables in the problem. Since the polarization of the nucleon is not measured, four variables are required to describe the event. As a convenient choice we take the set (θ, ϕ, m, t). θ and ϕ are the polar and azimuthal angles, respectively, of the outgoing π^- in the dipion rest frame; m is the invariant mass of the dipion; and t is the square of the four-momentum transfer to the nucleon. Two different coordinate systems are quite generally used for the measurement of θ, ϕ. They correspond to different choices for the z axis in the dipion rest frame. The Jackson frame is

*Since the detection efficiency of the spectrometer contains statistical contributions, the quantities in Eq. (V.2) are actually expectation values.

defined with the z axis along the direction of the incident pion, whereas the z axis lies opposite to the direction of the neutron in the helicity frame. In both frames, the y axis is normal to the production plane.

Fits to the experimental data are done using Eq. (V.2), where D is replaced by the theoretical function T as follows:

$$O(\theta, \phi, m, t) = E(\theta, \phi, m, t) \cdot T(\theta, \phi, m, t) \quad . \qquad (V.3)$$

The fitting is performed using a maximum-likelihood technique which will be discussed shortly.

B. Efficiency

In order to perform the fitting implied by Eq. (V.3), it is necessary to understand the efficiency of the spectrometer well. The efficiency was calculated using standard Monte Carlo techniques. The calculating program consisted of two basic sections: (1) a control section which generated events and controlled program I/O; and (2) an apparatus simulation section (PASS) which determined whether the generated event would have passed through the experimental apparatus.

The operation of the program was as follows: For a given set of variables (θ, ϕ, m, t), a number of trial events was generated with randomly chosen incident beam angles, target vertex coordinates, and angle of rotation of the production plane about the incident beam particle. The momenta of the tracks from these events were then given to the PASS section of the program, which tracked the particles through the magnetic field and determined whether a given event was lost. The efficiency $E(\theta, \phi, m, t)$ was then defined to be the ratio of the number of events which passed through the spectrometer divided by the total number of trials.

Losses of events in PASS could occur in two different ways. First, the event could miss the active area of the spectrometer (geometrical loss). Second, the event could be lost through a random process (statistical loss).

The geometrical losses were the major source of the functional dependence of $E(\theta, \phi, m, t)$ on the given variables. The geometrical cutoffs of the spectrometer were largely determined by the size of the magnet aperture and the distance between the target and the magnet. There was also a cutoff due to the plugs in the beam region of the front chambers which prevented the observation of very asymmetric ρ^0 decays. This limitation of the plug was matched by the low-momentum cutoff of the magnet which also prohibited the observation of very asymmetric decays.

Statistical losses which were dependent on the event kinematics and which were sufficiently large to cause an observable effect were included in PASS. Such losses were of two kinds: (1) losses due to inefficiency in the spark-chamber and triggering-hodoscope systems, and (2) losses from pion absorption in the target.

As was mentioned previously, any inefficiency in the triggering counters was directly reflected as an event loss since a track was not reconstructed without a matching hodoscope at each end (see Chapter III.B). The trigger hodoscope efficiencies which were used to correct for this track loss were measured using the experimental data as was discussed in Chapter II.F. Experimentally, the efficiency of the spark chambers did not depend on the position or angle of the track. Nevertheless, overall spark chamber efficiency was dependent on track position, since a track could pass through a plug or miss a spark chamber and still be reconstructed, but with a lower efficiency than if it had passed through the active area in all chambers. This loss was

corrected by using the measured individual chamber efficiencies to calculate total reconstruction efficiencies for the possible configurations of tracks in the chambers. That is, overall efficiencies were calculated for situations where the track missed the active area of one or more of the chambers as well as when the track passed through all of them. These overall spark chamber efficiencies were then included in PASS.

Pion absorption in the target was large (typically 15%) and dependent on the vertex position and kinematics of the event so this source of event loss was also included in PASS. Tracks were discarded according to a Monte Carlo procedure where the total probability of a track being discarded depended on its momentum and path length through the liquid hydrogen.

Other random effects (e.g., pion decay and absorption in the spectrometer) were small and only weakly dependent on the location and momentum of the track. They were simply included in the overall normalization to the cross section as was discussed in Chapter IV.

In deriving efficiencies for an actual physical process, there was an additional important effect which has been neglected above. In order to discriminate against higher missing mass states in reaction (V.1), a cut was applied in the data sample for events with missing mass between 0.8 and 1.06 GeV. The missing mass resolution (σ) is $\simeq$ 85 MeV, so that a fraction of the good $\rho^{o}n$ events was lost on this cut. This loss would ordinarily be considered to be an overall cross section normalization correction. However, for this spectrometer, the missing mass resolution is a function of the decay angles. In particular, the resolution was worse (by $\sim$15 MeV) for asymmetric events than for symmetric ones, so that a larger fraction of such data events was discarded on the missing mass cut. This effect was corrected for by

simulating this cut process in the efficiency program. A model was developed which calculated the missing mass resolution for each trial event on the basis of the position and momenta of the tracks and the uncertainties in the measurements of their coordinates. Then a missing mass for the trial event was calculated randomly for a neutron with this resolution, and events whose missing mass lay outside the neutron cut were rejected. Detailed comparisons of this model were made with the data and the agreement was excellent.

In order to demonstrate the basic features of the detection efficiency, Fig. 13 shows the projections in the helicity frame onto $\cos\theta^H$ and ϕ^H for three different t regions. These efficiencies have been integrated over the mass region $0.665 < m_{\pi\pi} < 0.865$ GeV, using a P-wave Breit-Wigner plus a linear background, and correspond to the efficiencies which were used to obtain the ρ^o density matrix elements.

In general, the efficiencies are peaked near $|\cos\theta^H| = 0$, with shoulders extending out to $|\cos\theta^H| \sim 0.85$. The peak in the efficiency near $|\cos\theta^H| = 0$ is large for small t, but becomes progressively smaller as t increases. However, this change is rather uniform in t and, in particular, is small over narrow regions, such as the region from $-t=0$ to $-t=m_\pi^2$. The efficiency at $|\cos\theta^H| = 0.75$ remains rather steady as t increases. The efficiency in ϕ^H is uniform for small t, but develops some structure as t becomes larger.

When observing the absolute values of these efficiencies, it should be noted that they include not only the geometrical losses but also the statistical losses noted above. We emphasize that even though these statistical losses change somewhat for different kinematical variables, nearly all of the dependence of the efficiencies in Fig. 13 as a function of θ, ϕ, m, and t is due to the

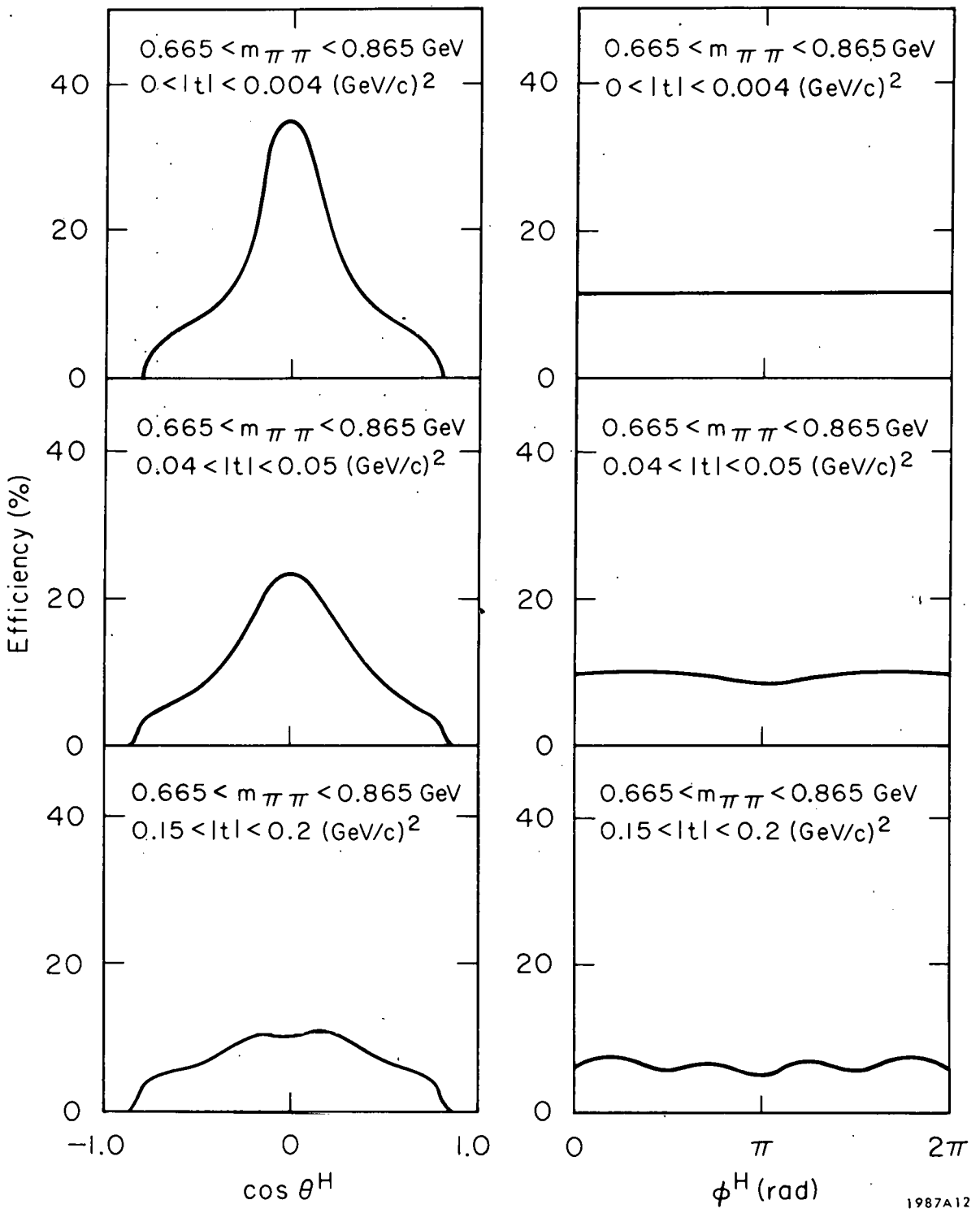

FIG. 13--Efficiencies in the helicity frame for the ρ^0 region, $0.665 < m_{\pi\pi} < 0.865$ GeV.

geometry of the spectrometer. The primary effect of the statistical losses is to lower the efficiencies by $\sim 40\%$ in absolute value.

C. Data

In order to select the experimental data sample which corresponds to reaction (V.1), it is necessary to reduce the amount of nonneutron background as much as possible. As was mentioned in the previous section, the missing mass was cut between 0.8 and 1.06 GeV in order to reject most of this background.

Additional background rejection was possible by using information from the target veto hodoscope which surrounded the target. In Fig. 14, we show a missing mass distribution for differing cuts on these veto counters. Histogram (a) shows the raw missing mass distribution for the ρ^o region. The neutron and N* bumps are clearly visible. Histogram (b) corresponds to the cut which was actually used to derive the data sample. The higher missing mass background has been reduced substantially. The background can be reduced still further by rejecting all events for which a veto hodoscope fires as is shown in histogram (c). However, we also note that a significant number of neutron events have been lost. The primary cause of this loss is that many of the neutron events are accompanied by a delta ray which fires an inner target counter. Additional neutron events are rejected because of neutron conversion in the counter assembly. The number of good $\rho^o n$ events eliminated by this cut depends on the kinematics of the event, and could create an efficiency bias.

To avoid this difficulty, we reject only those events for which ≥ 2 counters fired with at least one of these counters being in the outer layer (Fig. 14(b)). This cut allows nearly all delta-ray-accompanied neutron events to be retained.

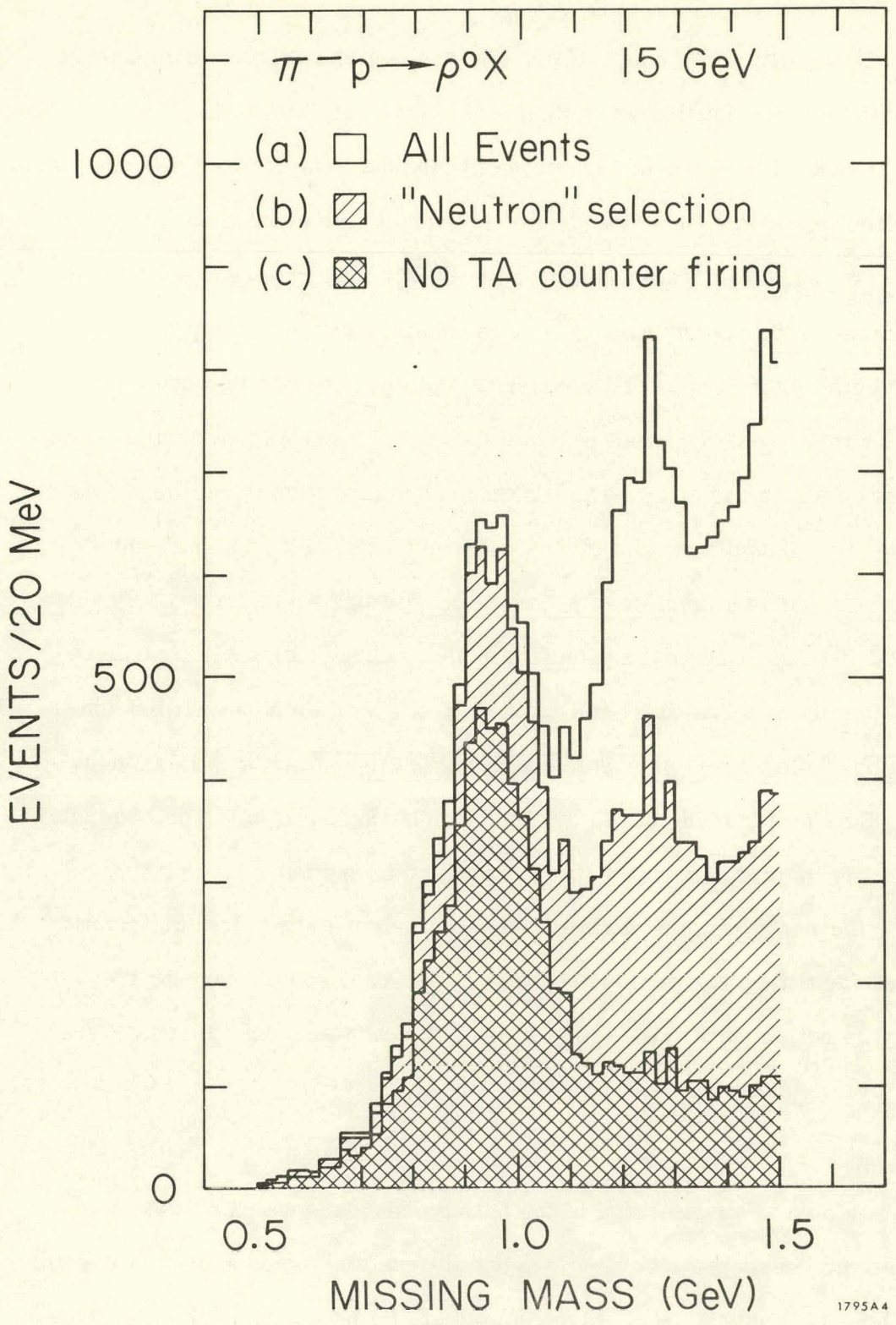

FIG. 14--Missing mass spectrum (M_X) for the reaction $\pi^- p \rightarrow \rho^o X$ for several different cuts on the target veto counters, (a) no TA cut, (b) TA cut used to select the $\rho^o n$ data sample (see text), (c) no TA counters allowed.

Effects such as neutron conversion in an outer counter with an accompanying delta ray in an inner counter are calculated to be negligible.

The amount of background remaining in the data sample after this cut had been applied was studied with the help of the target veto counters. The number of events lost underneath the neutron peak was plotted versus the number of events lost in the higher missing mass region for progressively more stringent cuts on the target-veto counters. For those cuts which could not reject a neutron event, this plot was quite linear. Therefore, a straight-line extrapolation was made to the zero background contribution using these cuts. In Fig. 15, we show the results of this determination. Little significant variation is noted as a function of t, so the background was corrected by an overall t-independent normalization factor of 12 ± 2%. This background consisted of the low missing mass tail from $\pi^+\pi^-\Delta^o$ events with a smaller contribution from the $K\pi$ and $p\pi$ events which passed the rather loose Cerenkov-counter selection for pions. The effect of this background on the determination of the density matrix elements will be discussed in Section F.

After the $\pi^+\pi^-$n sample had been defined as above, the actual distribution to be used for fitting was derived by running this data sample through the geometry selection portion of PASS, so both the efficiency and the data were subjected to the same geometrical cuts.

D. Fitting

We now turn to a discussion of the fitting procedure which was used to determine the density matrix elements and differential cross section. We will assume here that only S and P waves contribute in the region of the ρ^o. This assumption will be justified in detail later.

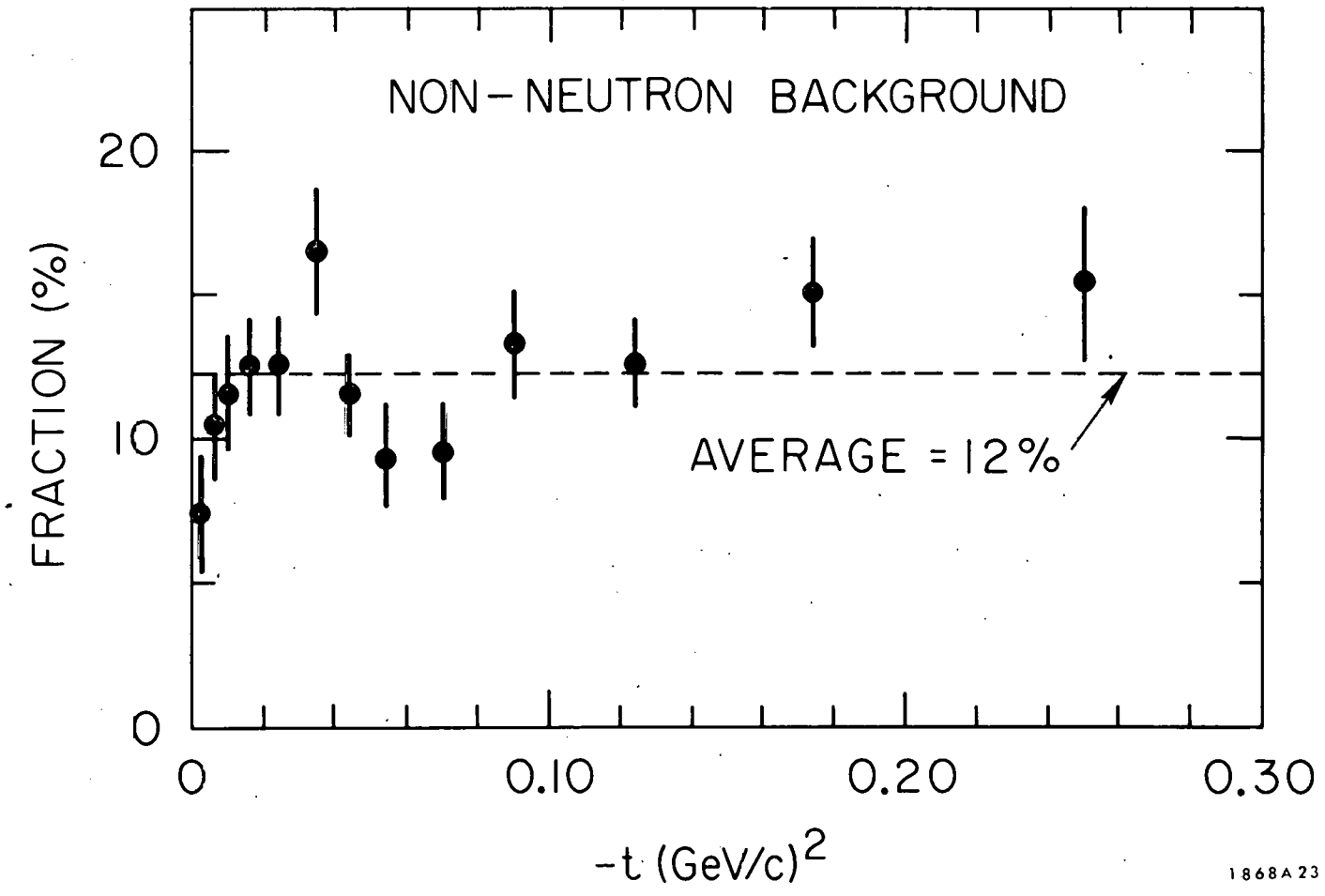

FIG. 15--Fraction of nonneutron background in data sample.

Under this assumption, a general theoretical function, which describes reaction (V.1) in our coordinate systems, can be written in terms of the spin density matrix elements as follows[38]:

$$T(\theta, \phi, m, t) = N(\theta, \phi, m, t)\, W(\theta, \phi, m, t) \quad , \tag{V.4}$$

where

$$\begin{aligned} W(\theta, \phi, m, t) = \frac{1}{4\pi} \Big\{ & 3\rho_{00}(m,t)\cos^2\theta + 3\rho_{11}(m,t)\sin^2\theta \\ & -3\sqrt{2}\,\mathrm{Re}\left[\rho_{10}(m,t)\right]\sin 2\theta\cos\phi - 3\rho_{1-1}(m,t)\sin^2\theta\cos 2\phi \\ & -2\sqrt{6}\,\mathrm{Re}\left[\rho_{1S}(m,t)\right]\sin\theta\cos\phi + 2\sqrt{3}\,\mathrm{Re}\left[\rho_{0S}(m,t)\right]\cos\theta + \rho^{S}_{00} \Big\} \end{aligned} \tag{V.5}$$

and N is some normalization constant. In this equation ρ_{1S} and ρ_{0S} represent interference terms between the S-wave and the transverse and longitudinal P-wave amplitudes, respectively, and ρ^{S}_{00} corresponds to the pure S-wave contribution. By use of the normalization condition,

$$\rho_{00} + 2\rho_{11} + \rho^{S}_{00} = 1 \quad , \tag{V.6}$$

ρ^{S}_{00} can be eliminated from Eq. (V.5). This yields

$$\begin{aligned} W(\theta, \phi, m, t) = \frac{1}{4\pi} \Big[& 1 + (\rho_{00} - \rho_{11})(3\cos^2\theta - 1) - 3\sqrt{2}\,\mathrm{Re}(\rho_{10})\sin 2\theta\cos\phi \\ & - 3\rho_{1-1}\sin^2\theta\cos 2\phi - 2\sqrt{6}\,\mathrm{Re}(\rho_{1S})\sin\theta\cos\phi + 2\sqrt{3}\,\mathrm{Re}(\rho_{0S})\cos\theta \Big] \end{aligned} \tag{V.7}$$

where $N(\theta, \phi, m, t)$ now becomes the number of events that were produced at the target. Since the density matrix elements are functions of both m and t, it would be desirable in the case of infinite statistics to fit the distributions in sufficiently small intervals in both m and t that any possible variations in

the density matrix elements could be observed. Rapid variation in the density matrix elements is expected in the small t region, however, so that very small t intervals are required and the experimental statistics are not sufficient to allow any additional cut on m. We therefore fit the observed data in one mass bin ($0.665 < m < 0.865$ GeV) centered about the ρ^0. This should not create any difficulty since the density matrix elements are expected to be slowly varying with m in the ρ region.

We derive the actual fitting form by integrating Eq. (V.3) over this mass interval and a small interval in t.

$$\int_{t_1-\frac{\Delta t}{2}}^{t_1+\frac{\Delta t}{2}} \int_{0.665}^{0.865} dt\, dm\, O(\theta, \phi, m, t) = \int_{t_1-\frac{\Delta t}{2}}^{t_1+\frac{\Delta t}{2}} \int_{0.665}^{0.865} dt\, dm\, E(\theta, \phi, m, t)\, T(\theta, \phi, m, t) \tag{V.8}$$

We assume that the m dependence of T is well represented by a Breit-Wigner plus a linear background term. Such a form fits the experimental data very well, though it differs somewhat from the form we will use when discussing the ρ cross section normalization. However, the efficiency is smooth and slowly varying across the ρ region, so that the density matrix elements are essentially independent of the exact form chosen in any case. The only important effect caused by a change in the assumed mass shape is a small change in the normalization which is easily taken into account in the final results.

Finally, rewriting Eq. (V.8) in somewhat simpler notation, we have the form which was used to find the dipion density matrix elements,

$$O(\theta, \phi, t_1) = N(t_1)\, E(\theta, \phi, t_1)\, W(\theta, \phi, t_1) \quad . \tag{V.9}$$

t_1 is a fixed value of t and the form of W is given by Eq. (V.7).

Fits to Eq. (V.9) are performed using a binned maximum-likelihood technique. For each interval in t, the data are placed in sufficiently small cos θ, ϕ bins that the right-hand side of Eq. (V.9) varies nearly linearly across the bin width. The probability of λ events in a given bin (cos θ_i, ϕ_j) is then assumed to follow a Poisson distribution with mean n.

$$P(\lambda_{ij}) = \frac{e^{-n_{ij}} (n_{ij})^{\lambda_{ij}}}{\lambda_{ij}!} \qquad (V.10)$$

The mean in this case is given by the right-hand side of Eq. (V.9) times the bin width.

$$n_{ij} = N E_{ij} W_{ij} \Delta \cos \theta_i \, \Delta\phi_j \quad . \qquad (V.11)$$

The likelihood function is simply the product of the Poisson probabilities for each bin.

$$\mathscr{L} = \Pi_{i,j} P(\lambda_{ij}) \qquad (V.12)$$

with the best fit being defined as that function of W for which $\mathscr{L}$ is maximized. In practice, $\mathscr{L}$ is most conveniently maximized by minimizing the quantity -log $\mathscr{L}$. Minimization was performed using a general ravine stepping procedure.[39] The error on a parameter was calculated by changing the value of that parameter while minimizing the value of -log $\mathscr{L}$ until -log $\mathscr{L}$ changed by 0.5 from its absolute minimum. The value of the parameter at this point then defined the 1 σ error.

E. Results

Using the fitting procedure outlined above, the density matrix elements shown in Figs. 16 and 17 and listed in Tables I and II were obtained. Fits were done independently in both the Jackson and helicity frames, and the

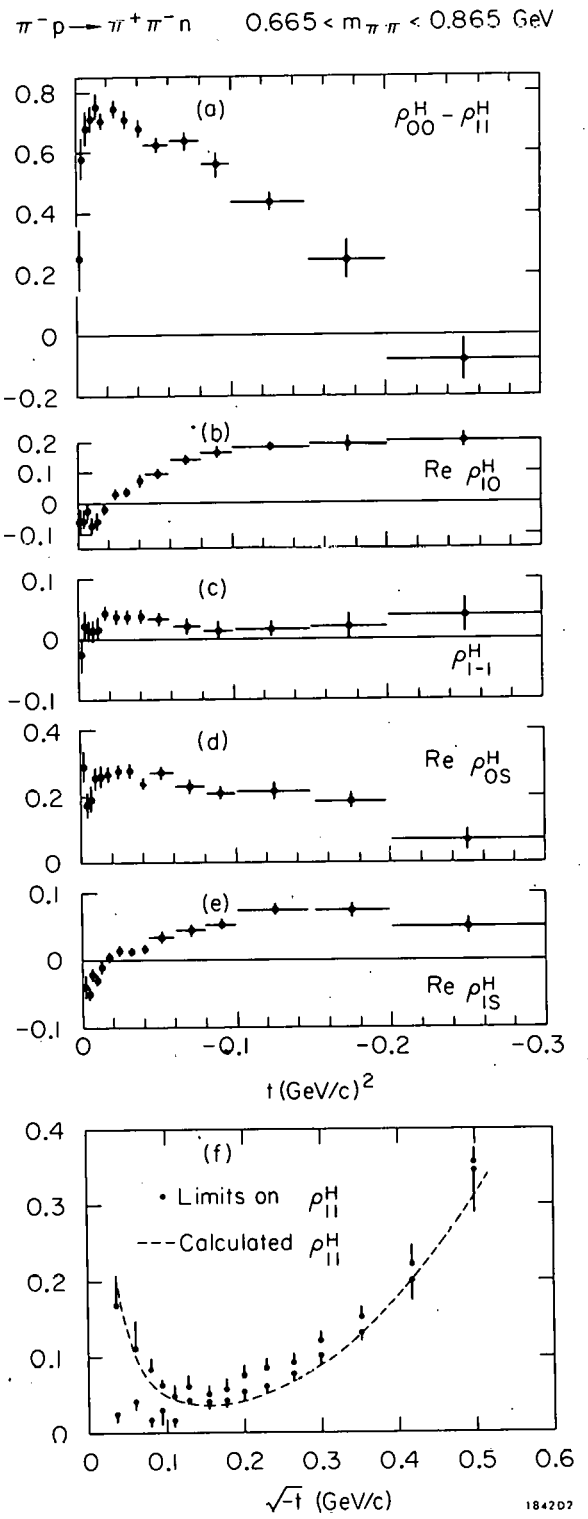

FIG. 16--(a-e) Density matrix elements in the helicity frame for the reaction $\pi^- p \to \pi^+ \pi^- n$ with $0.665 < m_{\pi\pi} < 0.865$ GeV, (f) upper and lower limits on ρ^H_{11} determined from the requirement that the density matrix be positive definite. The curve is the calculated ρ^H_{11} assuming the S wave is given by the scaled $\pi^- p \to \pi^0 \pi^0 n$ data.

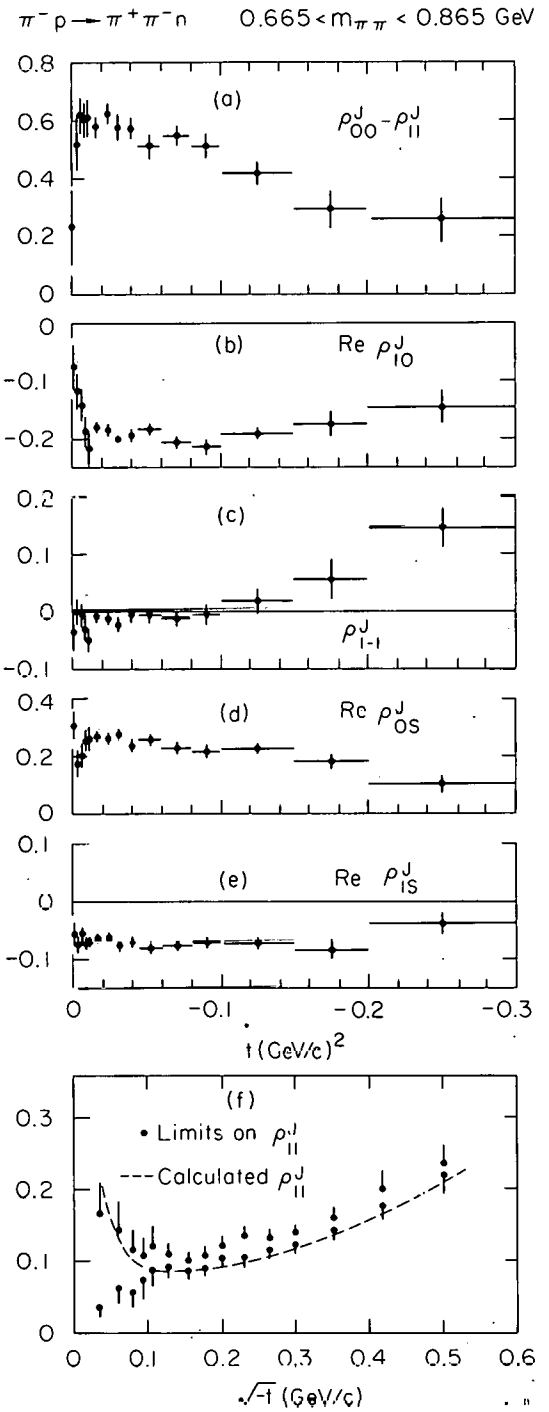

FIG. 17--(a-e) Density matrix elements in the Jackson frame for the reaction $\pi^- p \to \pi^+ \pi^- n$ with $0.665 < m_{\pi\pi} < 0.865$ GeV, (f) upper and lower limits on ρ^J_{11} determined from the requirement that the density matrix be positive definite. The curve is the calculated ρ^J_{11} assuming the S wave is given by the scaled $\pi^- p \to \pi^0 \pi^0 n$ data.

TABLE I

Density Matrix Elements Evaluated in the Helicity Frame for $\pi^- p \to \pi^+ \pi^- n$, $.665 < m_{\pi\pi} < .865$ GeV

$-t$ (GeV/c)^2	$\rho^H_{00}-\rho^H_{11}$	Re ρ^H_{10}	ρ^H_{1-1}	Re ρ^H_{0S}	Re ρ^H_{1S}	$\rho^{H\ *}_{11}$
t_{min} - .0025	.248 ± .127	-.067 ± .040	-.025 ± .033	.296 ± .048	-.038 ± .021	.228 ± .042
.0025 - .0050	.595 ± .080	-.053 ± .031	.023 ± .020	.180 ± .045	-.048 ± .012	.097 ± .027
.0050 - .0075	.699 ± .061	-.034 ± .030	.015 ± .020	.202 ± .042	-.022 ± .011	.054 ± .020
.0075 - .0100	.734 ± .054	-.079 ± .028	.014 ± .016	.257 ± .037	-.029 ± .010	.038 ± .018
.0100 - .0125	.778 ± .045	-.068 ± .035	.015 ± .016	.268 ± .038	-.010 ± .009	.024 ± .015
.0125 - .0200	.722 ± .033	-.020 ± .010	.044 ± .010	.280 ± .020	.005 ± .006	.038 ± .011
.0200 - .0275	.760 ± .028	.028 ± .013	.038 ± .010	.280 ± .020	.017 ± .005	.031 ± .009
.0275 - .0350	.734 ± .036	.037 ± .015	.039 ± .011	.283 ± .023	.012 ± .007	.034 ± .012
.035 - .045	.705 ± .035	.078 ± .016	.040 ± .012	.247 ± .023	.022 ± .007	.040 ± .012
.045 - .060	.644 ± .034	.098 ± .014	.035 ± .012	.274 ± .021	.037 ± .007	.057 ± .011
.060 - .080	.656 ± .033	.145 ± .013	.023 ± .011	.240 ± .020	.045 ± .006	.061 ± .011
.080 - .100	.580 ± .047	.174 ± .017	.017 ± .018	.219 ± .026	.057 ± .009	.079 ± .016
.100 - .150	.454 ± .039	.186 ± .012	.019 ± .016	.225 ± .020	.077 ± .008	.123 ± .013
.150 - .200	.250 ± .073	.203 ± .020	.024 ± .027	.194 ± .012	.077 ± .012	.197 ± .024
.200 - .300	-.086 ± .099	.211 ± .022	.041 ± .034	.077 ± .033	.053 ± .016	.306 ± .033

*Note: The values of ρ^H_{11} are not directly measured and depend on certain assumptions concerning the S-wave. See discussion in text.

TABLE II

Density Matrix Elements Evaluated in the Jackson Frame for $\pi^- p \rightarrow \pi^+ \pi^- n$, $.665 < m_{\pi\pi} < .865$ GeV

$-t(GeV/c)^2$	$\rho^J_{00} - \rho^J_{11}$	$Re\rho^J_{10}$	ρ^J_{1-1}	$Re\,\rho^J_{0S}$	$Re\,\rho^J_{1S}$	ρ^J_{11}*
t_{min} - .0025	.231 ± .131	-.073 ± .042	-.032 ± .034	.299 ± .050	-.055 ± .021	.232 ± .044
.0025- .005	.518 ± .091	-.114 ± .030	.001 ± .022	.167 ± .046	-.070 ± .015	.124 ± .030
.005 - .0075	.621 ± .057	-.134 ± .029	-.007 ± .019	.186 ± .039	-.052 ± .010	.082 ± .019
.0075- .010	.601 ± .061	-.185 ± .027	-.029 ± .018	.243 ± .037	-.070 ± .012	.084 ± .020
.010 - .0125	.603 ± .066	-.211 ± .033	-.047 ± .021	.263 ± .038	-.068 ± .009	.083 ± .022
.0125- .020	.575 ± .034	-.178 ± .011	-.006 ± .011	.268 ± .015	-.061 ± .005	.088 ± .011
.020 - .0275	.618 ± .032	-.184 ± .016	-.011 ± .011	.258 ± .028	-.059 ± .007	.079 ± .011
.0275- .035	.574 ± .042	-.195 ± .013	-.016 ± .013	.267 ± .022	-.078 ± .009	.088 ± .014
.035 - .045	.576 ± .034	-.196 ± .016	-.007 ± .015	.228 ± .019	-.069 ± .008	.085 ± .011
.045 - .060	.505 ± .038	-.184 ± .013	-.009 ± .012	.257 ± .020	-.079 ± .008	.104 ± .013
.060 - .080	.546 ± .035	-.207 ± .013	-.014 ± .015	.222 ± .020	-.073 ± .008	.097 ± .012
.080 - .100	.508 ± .044	-.214 ± .012	-.008 ± .018	.208 ± .023	-.067 ± .009	.103 ± .015
.100 - .150	.416 ± .038	-.194 ± .007	.015 ± .016	.232 ± .021	-.072 ± .008	.137 ± .013
.150 - .200	.293 ± .063	-.178 ± .022	.056 ± .035	.182 ± .026	-.081 ± .016	.182 ± .021
.200 - .300	.247 ± .079	-.144 ± .029	.145 ± .031	.102 ± .031	-.035 ± .020	.195 ± .026

*Note: The values ρ^J_{11} are not directly measured and are dependent on certain assumptions concerning the S-wave. See discussion in text.

consistency of the results was checked by rotating from one frame to the other. The error bars shown are statistical only. Systematic errors, which could result if there were small unknown biases in the apparatus or event reconstruction, are estimated to be less than the statistical errors.

The fact that Re ρ_{0S} and Re ρ_{1S} do not vanish is conclusive evidence that the dipion system may not be described by a pure P wave. Many of the density matrix elements exhibit structure for small values of momentum transfer ($-t < m_\pi^2$). In particular, there is a striking dip in $\rho_{00}-\rho_{11}$ in both frames. The Re ρ_{10}^J has a sharp rise at small t, whereas Re ρ_{1S}^H and Re ρ_{10}^H cross through zero at $t=-m_\pi^2$.* We also note that ρ_{1-1}^H is small and positive everywhere, whereas ρ_{1-1}^J is similar to zero for small t.

While VDM calculations require a knowledge of ρ_{11}, the fits to the angular distribution in this experiment directly determine only the combination $\rho_{11}+\frac{1}{3}\rho_{00}^S$. In order to derive the value of ρ_{11}, it is necessary to determine both the t dependence and the absolute normalization of the S-wave background using additional information which is available from several different sources.

The fact that the density matrix must be positive definite places significant limits on the value of ρ_{00}^S, since the off-diagonal terms are rather large. In particular, the following inequalities must be satisfied:

$$0 \leq \rho_{11} \leq 0.5$$

$$0 \leq \rho_{00} \leq 1$$

$$0 \leq \rho_{00}^S \leq 1$$

*A superscript J(H) refers to density matrix elements in the Jackson (helicity) frame.

$$\left.\begin{aligned} \rho_{00}\rho_{11} &\geq (\mathrm{Re}\,\rho_{10})^2 \\ \rho_{11}\rho^S_{00} &\geq (\mathrm{Re}\,\rho_{1S})^2 \\ \rho_{00}\rho^S_{00} &\geq (\mathrm{Re}\,\rho_{0S})^2 \\ \rho_{11} &\geq |\rho_{1-1}| \end{aligned}\right\} \text{Schwartz inequalities}$$

$$\rho_{00}(\rho_{11}-\rho_{1-1}) \geq 2(\mathrm{Re}\,\rho_{10})^2$$

$$\rho^S_{00}(\rho_{11}-\rho_{1-1}) \geq 2(\mathrm{Re}\,\rho_{1S})^2$$

$$\rho_{00}\rho_{11}\rho^S_{00} + 2(\mathrm{Re}\,\rho_{1S})(\mathrm{Re}\,\rho_{0S})(\mathrm{Re}\,\rho_{10}) \geq \rho_{11}(\mathrm{Re}\,\rho_{0S})^2 + \rho^S_{00}(\mathrm{Re}\,\rho_{10})^2 + \rho_{00}(\mathrm{Re}\,\rho_{1S})^2$$

$$\rho_{00}\rho^S_{00}(\rho_{11}-\rho_{1-1}) + 4(\mathrm{Re}\,\rho_{1S})(\mathrm{Re}\,\rho_{0S})(\mathrm{Re}\,\rho_{10}) \geq (\rho_{11}-\rho_{1-1})(\mathrm{Re}\,\rho_{0S})^2 + 2\rho^S_{00}(\mathrm{Re}\,\rho_{10})^2 + 2\rho_{00}(\mathrm{Re}\,\rho_{1S})^2 . \quad \text{(V.13)}$$

These conditions allow one to establish upper and lower limits on ρ_{11}, ρ_{00}, and ρ^S_{00}. The variance matrix of the fitted constants can then be propagated to estimate the errors on these limits. The limits on ρ_{11} calculated in this manner are shown in Figs. 16(f) and 17(f). It should be noted that these limits are quite restrictive in both normalization and shape with the exception of the very small t region ($-t < m_\pi^2/2$).

Independent information on ρ^S_{00} (and hence ρ_{11}) may be obtained from existing $\pi^- p \to \pi^o\pi^o n$ data. Figures 18(a) and 18(b) show data on this reaction from the experiments of Shibata et al.,[40] and Sonderegger and Bonamy.[41] Both experiments clearly show a similar t dependence and, in particular, a forward dip for $-t < m_\pi^2$. The curves in Fig. 18 are fits to these data,

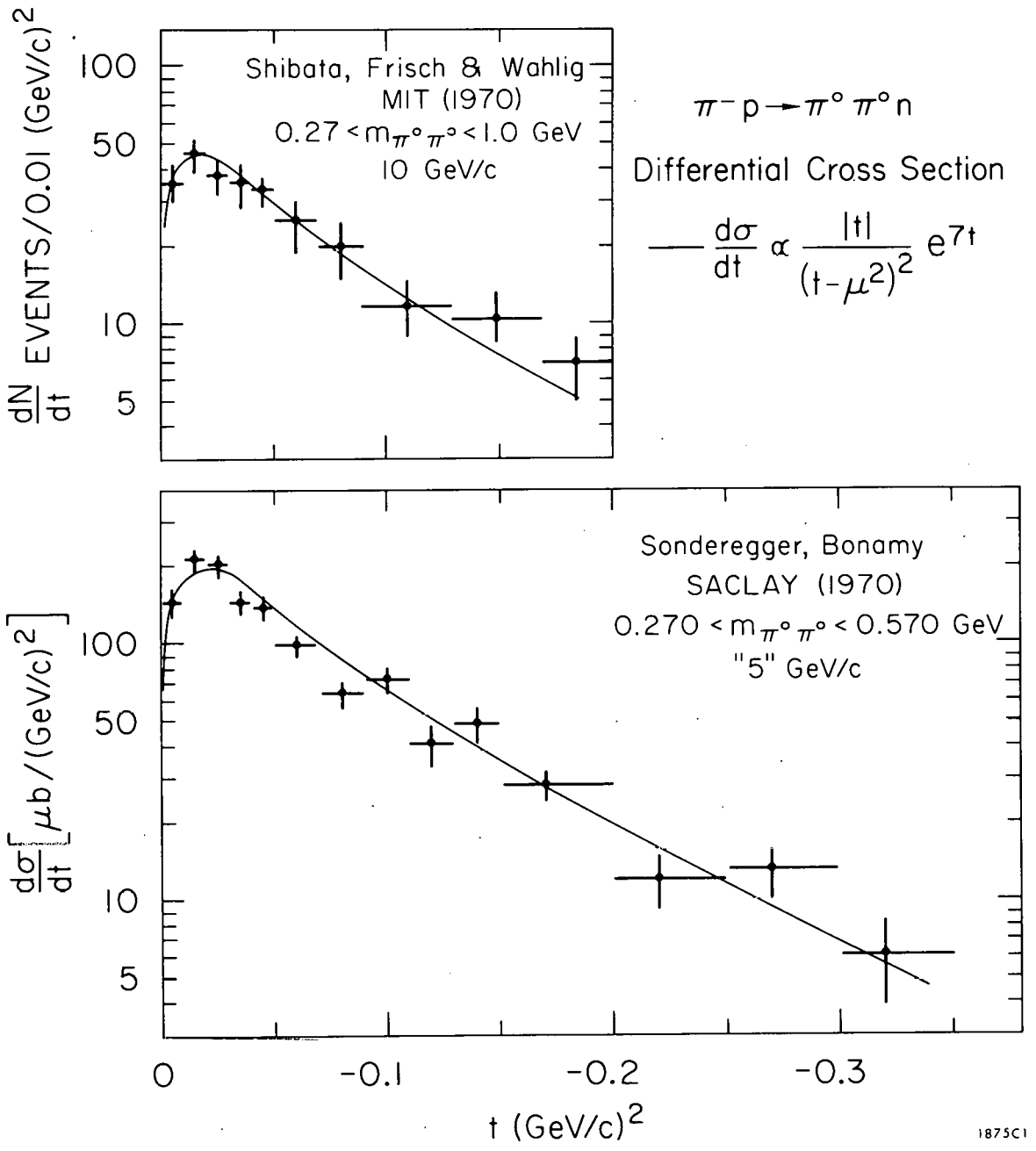

FIG. 18--Differential cross sections as functions of momentum transfer for the reaction $\pi^- p \rightarrow \pi^0 \pi^0 n$.

assuming

$$\frac{d\sigma}{dt}(\text{S-wave}) \propto \frac{|t|\, e^{7t}}{(t - m_\pi^2)^2} \cdot \qquad (V.14)$$

This is the form expected in several modified one-pion-exhange models[27,42] at high energy and clearly fits the observed t dependence very well. Sonderegger and Bonamy have studied the energy dependence of the cross section from 3 to 18 GeV and show that it is well represented by a $1/P_{lab}^2$ falloff.

Using the t dependence of Eq. (V.14) and the normalization obtained by scaling the data of Sonderegger and Bonamy to 15 GeV, we obtain the values of ρ_{11} indicated by the dotted lines in Figs. 16(f)and 17(f). The agreement with the limits described previously is quite good. The amount of S-wave indicated corresponds to $\sim 12\%$ for $-t < m_\pi^2$.

As an alternative method for determining the S-wave cross section, we can use a model-dependent approach.[27,42] In particular, the absorption modified one-pion-exchange model of P. K. Williams fits our data on $\pi^+\pi^-n$ very well for small values of momentum transfer where sharp structure is observed in the density matrix elements and differential cross section. The results of these fits are described in detail elsewhere[43] and we simply quote the fitted values for the S-wave background. The amount of S wave in the region $-t < m_\pi^2$ required to fit the data is $\sim 10\%$ where the form of the S-wave cross section in this model is identical to Eq. (V.14).

We can also calculate the values of ρ_{11} taking the amount of S wave from our fits to the $\pi^+\pi^-$ mass spectrum (see below) and assuming the t dependence of Eq. (V.14). The amount of S wave required for $-t < m_\pi^2$ is $11 \pm 2\%$, which agrees very well with the other determinations above.

The consistency of the above determinations for the S-wave background is excellent. Taking the t dependence from Eq. (V.14) as suggested by the absorption-modified one-pion-exchange model and the $\pi^o\pi^o n$ data, the amount of S wave required by all of these methods is $\sim 11\%$ with a range of approximately ± 1-2%. For the purposes of this thesis, we take the value of ρ_{00}^S to be 12% as given by the scaled $\pi^o\pi^o n$ data. However, there are no important qualitative changes in the data for any value of ρ_{00}^S in the allowed range. Moreover, the strong peaking of ρ_{11} in the forward direction does not depend strongly on the details of the S-wave t dependence. To show this explicitly, consider the following: The $\pi^o\pi^o n$ data are actually observed to fall by only 25% from $-t = m_\pi^2$ to $t = t_{min}$ rather than vanishing at t=0, as predicted by Eq. (V.14). Of course, this neglects resolution and bin width effects, but if the S wave is assumed to fall only this amount, the peak in ρ_{11} is decreased by only $\sim 20\%$.

The total differential cross section $\frac{d\sigma}{dt}(\pi^- p \to \pi^+\pi^- n)$, and the transversely polarized cross section in the helicity frame, $2\rho_{11}^H \frac{d\sigma}{dt}(\pi^- p \to \pi^+\pi^- n)$, are shown in Fig. 19 for the mass interval $0.665 < m_{\pi\pi} < 0.865$ GeV. The longitudinal and transverse cross sections for the Jackson frame are shown in Fig. 20 and the cross sections are listed in Table III. The overall normalization uncertainty of $\sim 7\%$ (see Chapter IV.B) is not included in the given errors. We observe a strong forward peak in the helicity transverse cross section as predicted by the VDM. On the other hand, the total cross section shows a sharp forward dip and the transverse cross section in the Jackson frame is approximately flat.

The total ρ cross section, which is shown in Fig. 21, has been obtained from the $\pi^+\pi^-$ cross section by subtracting the S wave and correcting for the

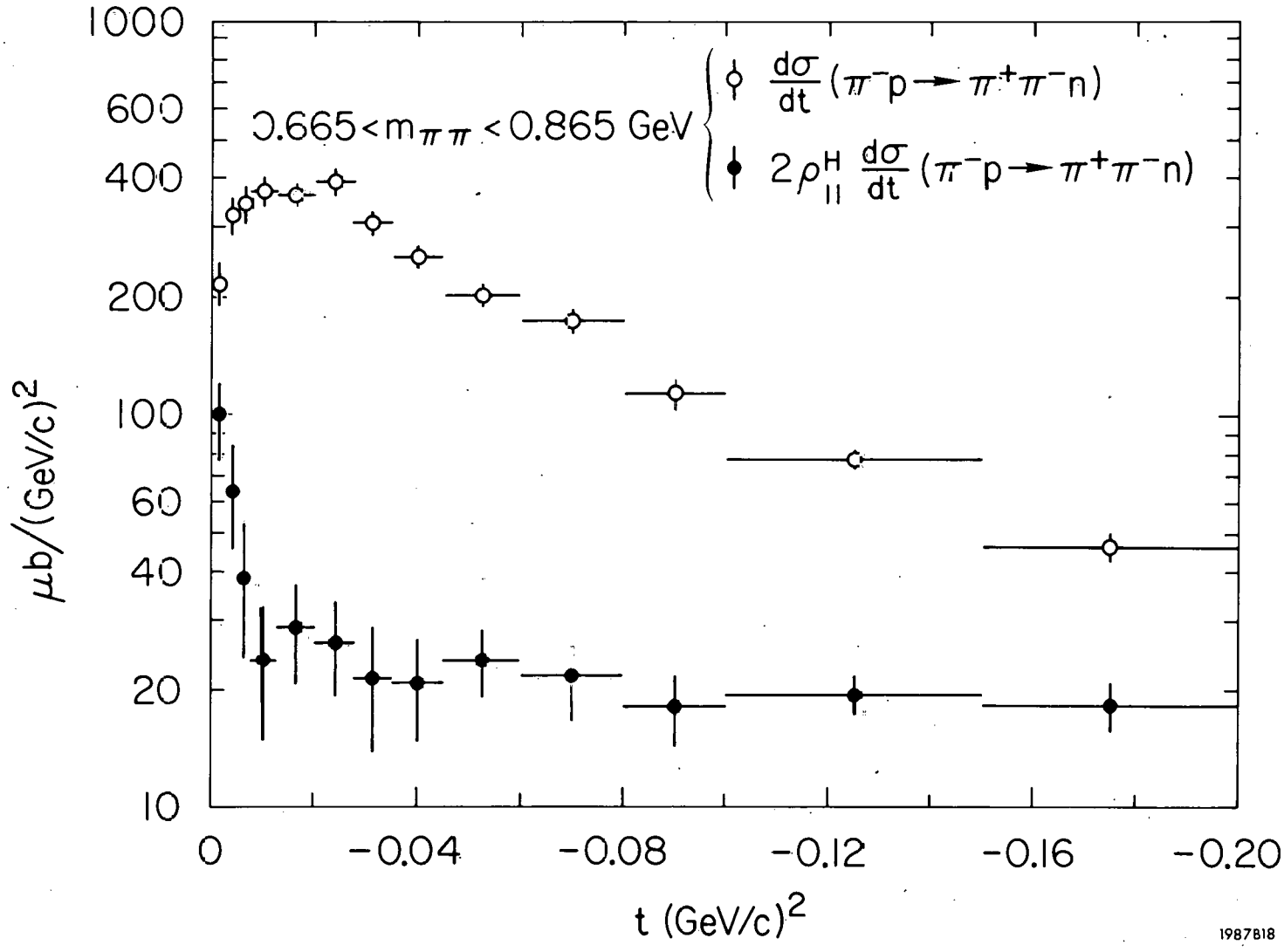

FIG. 19--The total and transverse (helicity) differential cross sections as functions of momentum transfer for $\pi^- p \to \pi^+ \pi^- n$, $0.665 < m_{\pi\pi} < 0.865$ GeV.

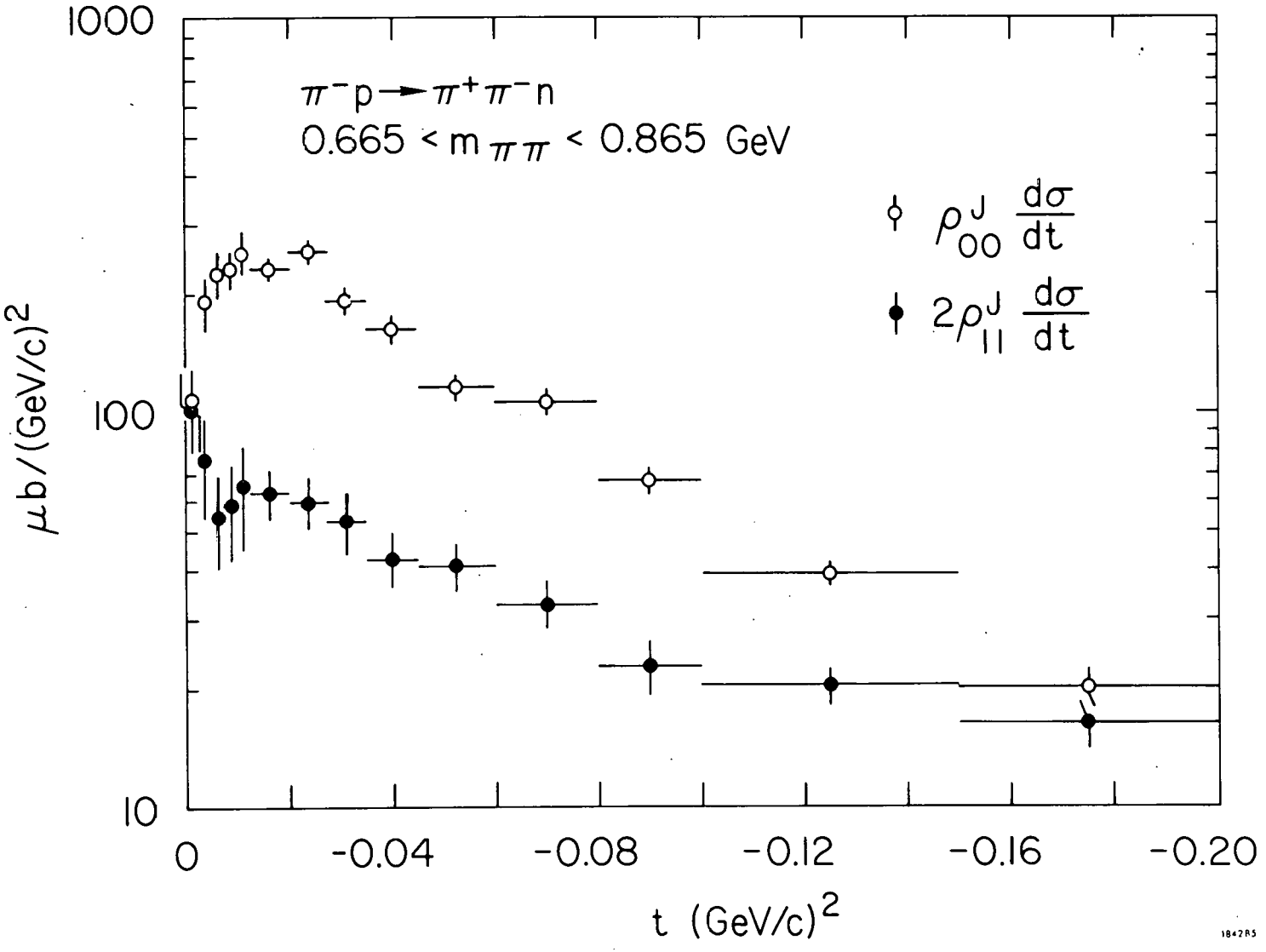

FIG. 20--The longitudinal and transverse differential cross sections in the Jackson frame as functions of momentum transfer for $\pi^- p \rightarrow \pi^+ \pi^- n$, $0.665 < m_{\pi\pi} < 0.865$ GeV.

TABLE III

Differential Cross Sections for $\pi^- p \to \pi^+ \pi^- n$

$-t$ $(GeV/c)^2$	$\frac{d\sigma}{dt}(\pi\pi)$ $\mu b/(GeV/c)^2$	$\rho_{11}^H \frac{d\sigma}{dt}(\pi\pi)$ * $\mu b/(GeV/c)^2$	$\rho_{11}^J \frac{d\sigma}{dt}(\pi\pi)$ * $\mu b/(GeV/c)^2$	$\frac{d\sigma}{dt}(\rho)$ * $\mu b/(GeV/c)^2$
t_{min} - .0025	221 ± 29	50.5 ± 11.4	51.2 ± 12.1	368 ± 51
.0025 - .005	307 ± 36	29.9 ± 8.9	37.9 ± 10.5	487 ± 65
.005 - .0075	332 ± 36	17.9 ± 7.0	27.3 ± 7.2	511 ± 65
.0075 - .010	344 ± 36	13.0 ± 6.3	28.9 ± 7.8	521 ± 64
.010 - .0125	377 ± 38	9.2 ± 5.8	31.3 ± 9.0	574 ± 68
.0125 - .020	355 ± 17	13.6 ± 4.0	31.2 ± 4.5	531 ± 30
.020 - .0275	375 ± 23	11.7 ± 3.5	29.6 ± 4.4	572 ± 41
.0275 - .035	301 ± 21	10.1 ± 3.7	26.5 ± 4.7	448 ± 38
.035 - .045	250 ± 17	10.0 ± 3.0	21.3 ± 3.3	368 ± 30
.045 - .060	195 ± 12	11.2 ± 2.3	20.3 ± 2.8	284 ± 22
.060 - .080	168 ± 10	10.2 ± 1.9	16.3 ± 2.2	252 ± 18
.080 - .100	111 ± 8.5	8.7 ± 1.8	11.4 ± 1.8	162 ± 15
.100 - .150	74.1 ± 3.9	9.1 ± 1.1	10.2 ± 1.1	109 ± 7.0
.150 - .200	44.7 ± 3.5	8.8 ± 1.3	8.1 ± 1.1	67.0 ± 6.3
.200 - .300	20.5 ± 1.7	6.3 ± 0.8	4.0 ± 0.6	30.5 ± 3.0

$$\frac{d\sigma}{dt}(\pi\pi) \equiv \frac{d\sigma}{dt}(\pi^- p \to \pi^+ \pi^- n), \quad .605 < m_{\pi\pi} < .865 \text{ GeV}$$

$$\frac{d\sigma}{dt}(\rho) \equiv \frac{d\sigma}{dt}(\pi^- p \to \rho^0 n)$$

*Note: The values of $\rho_{11}^H \frac{d\sigma}{dt}$, $\rho_{11}^J \frac{d\sigma}{dt}$, and $\frac{d\sigma}{dt}(\rho)$ are not directly measured and depend on certain assumptions concerning the S-wave. See discussion in text.

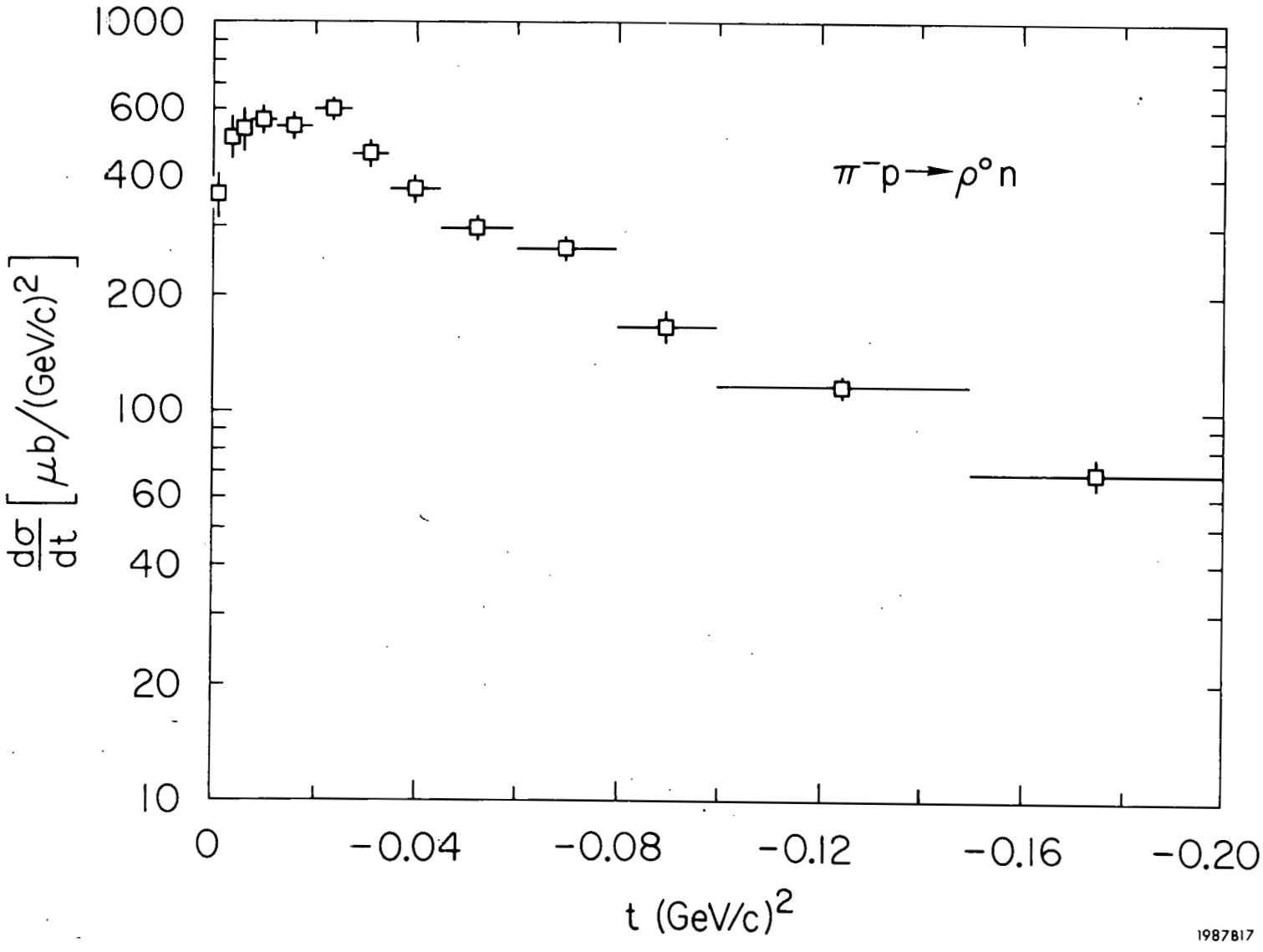

FIG. 21--The differential cross section as a function of momentum transfer for the reaction $\pi^- p \rightarrow \rho^0 n$.

fraction of the ρ mass spectrum outside our mass interval. The normalization error is ±25%, the dominant contribution coming from the uncertainty in the ρ line shape, as described below.

In order to determine the normalization of the ρ^o cross section, it is necessary to know both the amount of $\pi^+\pi^-$ background and the total fraction of the ρ^o meson which lies within the mass interval $0.665 < m_{\pi\pi} < 0.865$ GeV. Detailed knowledge of both the ρ^o and background mass shapes is required to determine accurate values for these quantities. Unfortunately, there exists very little information about the background mass shape and even the shape of the ρ^o is not well known as $m_{\pi\pi}$ becomes large. Consequently, from a purely phenomenological point of view, we have a great deal of freedom in choosing our fitting forms. For example, we can get a reasonable fit to the data by using any one of several common Breit-Wigner forms and using a simple polynomial to describe the background (see, e.g., Chapter VII). As a consistency check of our results, however, it is of interest to fit the mass distribution using only a P-wave resonance and an S-wave background which has approximately the mass shape of the $\pi^o\pi^o$n data, since this was the background used to determine the amount of S wave in the density matrix elements and differential cross section. If we are able to get consistent results, it will increase our confidence that the previous determinations of the background were reasonable.

With this view in mind, we fit the mass spectrum shown in Fig. 22 from 0.4 - 0.9 GeV. The fit is done in the small t region ($-t < 0.02$) to avoid possible complications from ρ-ω interference effects. The P wave is parameterized by a Breit-Wigner form which was used by Pisut and Roos[44]

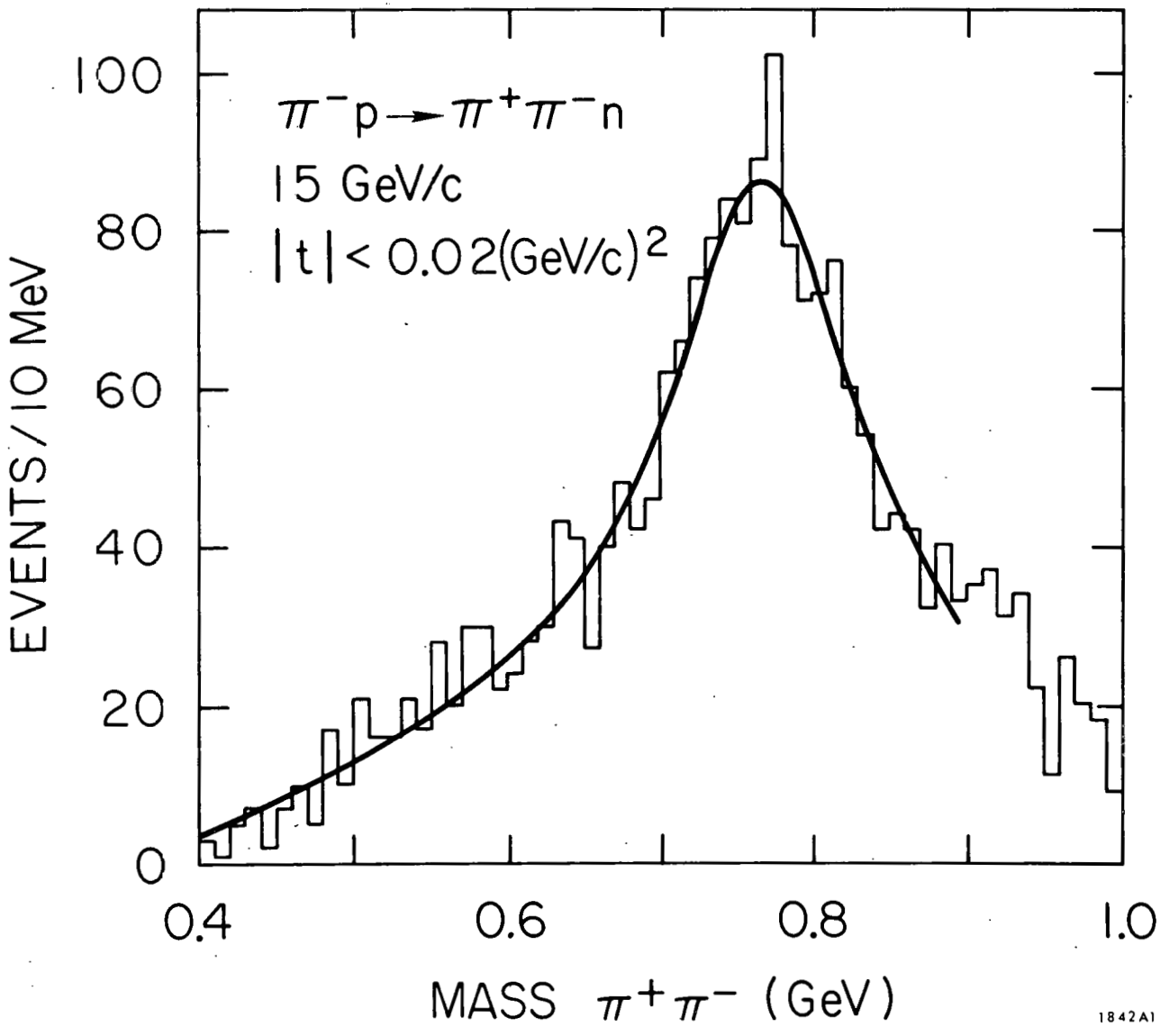

FIG. 22--The observed $\pi^+\pi^-$ mass spectrum for $|t| < 0.02$ $(GeV/c)^2$. The curve represents the fit described in the text after it has been folded with the acceptance.

to fit both $\rho^{\pm}$ and ρ^{o} mass distributions at lower energies:

$$\frac{d\sigma}{dm} \propto \frac{1}{q} \frac{m^2 m_0^2 \Gamma_\ell^2(m)}{\left(m_0^2 - m^2\right)^2 + m_0^2 \Gamma_\ell^2(m)} \int_{t_{min}(m)}^{T} e^{At} dt \qquad (V.15)$$

where $\Gamma_\ell(m) = \Gamma_0 \left(\frac{q}{q_0}\right)^{2\ell+1} \frac{m_0}{m} \frac{1+R^2 q_0^2}{1+R^2 q^2}$; ℓ = angular momentum of resonance,

$$q = \left(\frac{m^2}{4} - m_\pi^2\right)^{1/2}$$

$$q_0 = \left(\frac{m_0^2}{4} - m_\pi^2\right)^{1/2}$$

m_0, Γ_0 = the mass and width,

A is the slope of $d\sigma/dt$ $(\pi^- p \rightarrow \rho^o n)$,

$t_{min}(m)$ is the kinematical lower limit of t ,

T is the upper limit of |t| for the event sample, and

R is a parameter which corresponds to the range of the interaction.

The S-wave contribution is also parameterized by the above form with an assumed mass of 0.7 GeV and width of 0.4 GeV; this is consistent with the $\pi^o\pi^o$ mass distribution.[41] The fit yields a rho mass and width $M_\rho = 0.771 \pm 0.004$ GeV, $\Gamma_\rho = 0.160 \pm 0.014$ GeV, and $R^2 = 4.8 \pm 3.2\,(\text{GeV/c})^{-2}$. The amount of S wave required is $11 \pm 2\%$ which agrees well with the 12% predicted by scaling the $\pi^o\pi^o n$ data. Other acceptable fits to the mass spectrum may also be obtained by changing R or by choosing different Breit-Wigner functions, such as the standard P-wave form discussed by Jackson.[45] Although these forms are indistinguishable within the interval 0.4 - 0.9 GeV, the high mass behavior results in normalizations differing by ±20%. Since this region is

complicated by the presence of other resonances, it is difficult to distinguish between the forms by extending the fits to higher masses.

F. Background and Fitting Checks

1. Higher Partial Waves

In order to derive the above density matrix elements, the data were assumed to contain only S and P waves. Recently, Biswas et al.[46] have suggested that higher partial waves than ℓ=1 may also be present. They find that their 4-GeV data are inconsistent with the relation $\langle\cos 2\phi\rangle = -\frac{3}{4}\rho_{1-1}\sin^2\theta$, which is valid if only S and P waves are present, and they also find ρ_{1-1} to be strongly mass dependent. Our data show no evidence of these discrepancies: $\langle\cos 2\phi\rangle$ is consistent with $-\frac{3}{4}\rho_{1-1}\sin^2\theta$ (χ^2 = 16.5 for 18 degrees of freedom) and there is no evidence for a mass dependence of ρ_{1-1} over our mass interval (χ^2 = 10.6 for 10 degrees of freedom).

As an additional check, we have studied the χ^2 distributions for our fits to the angular distribution. If higher partial waves were present, the fit would be expected to deviate from the data in particular regions of cos θ or ϕ and the χ^2 contribution would be anomalously large there. Figure 23 shows the projections of the χ^2 distribution onto cos θ and ϕ. It is clear that there is no unusually large χ^2 value in any particular region as would be expected if D waves were present. We have also fit the decay angular distribution as a function of mass, including S, P, and D wave effects. For $m_{\pi\pi} < 0.9$ GeV, both the D wave and the P-D interference components are consistent with zero. Hence, we conclude that partial waves with $\ell \geq 2$ are not required to describe our decay angular distribution.

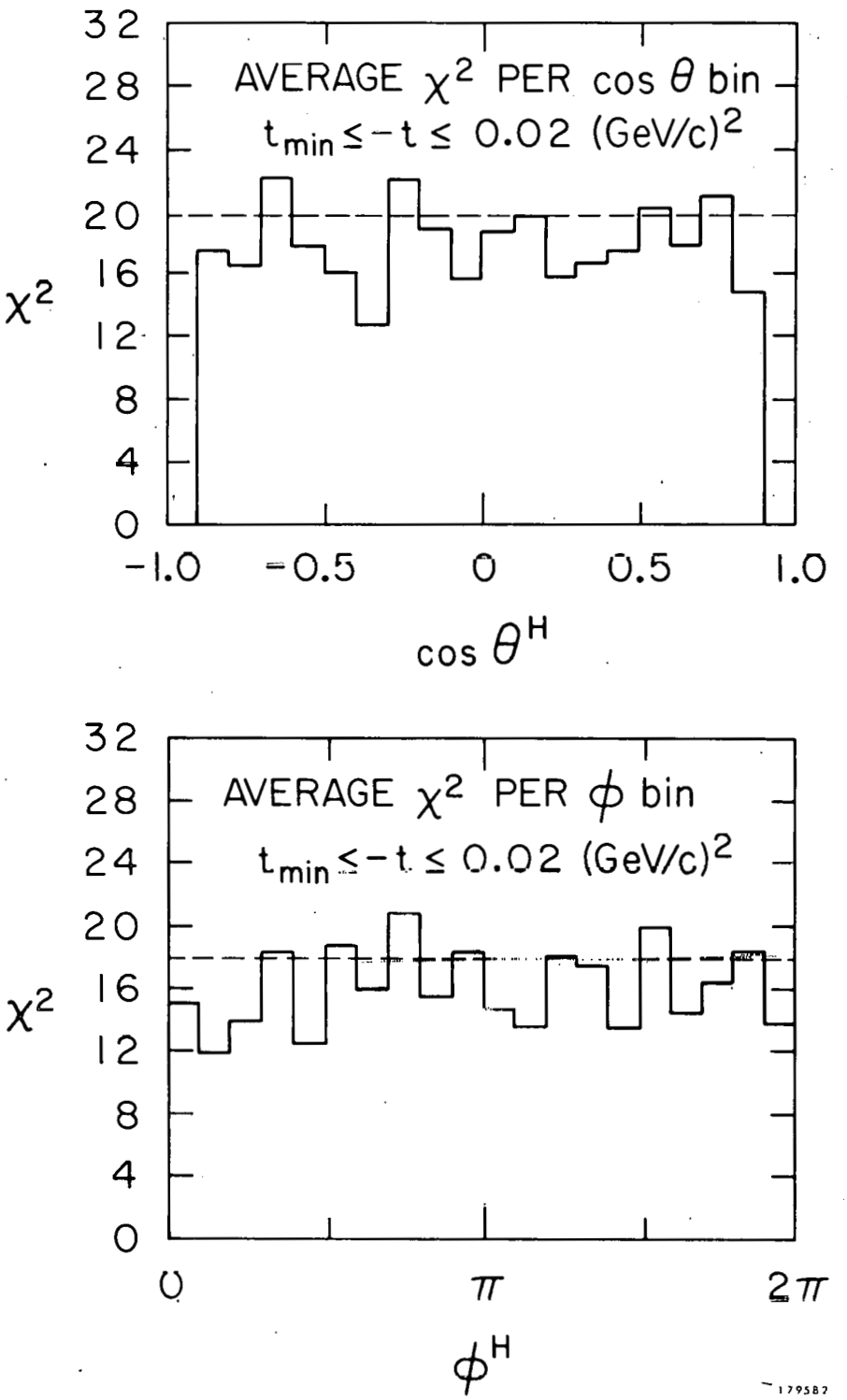

FIG. 23--χ^2 projections of the fits to the dipion decay angular distribution onto the cos θ and ϕ axes.

2. Higher Missing Mass Background

As was mentioned previously, the data sample which was used for fitting the density matrix elements contained an $\sim 12\%$ background contribution in the missing mass. In order to demonstrate that this background did not significantly affect the fitted values of the density matrix elements, we have refitted the density matrix using different cuts on the missing mass in order to change the relative amount of the higher missing mass states. For example, in Fig. 24 we compare the helicity-frame density matrix elements and differential cross section for a missing mass between 0.8 and 1.0 GeV with the density matrix elements and $d\sigma/dt$ obtained previously for a cut between 0.8 and 1.06 GeV. No significant difference is noted between the two fits, so we conclude that the background does not significantly affect the quoted values for ρ_{ij} and $d\sigma/dt$.

3. Efficiency Calculation

Because of the direct way in which the efficiency calculation enters the results, it is clearly very important to make checks of the Monte Carlo in order to insure its reliability. Many such checks have been made and some of the more important ones are discussed below.

One important check of the efficiency calculation was performed by generating events according to the fitted density matrix elements. These events were then tracked through PASS and the resulting distributions in the angular variables compared to the real data. In addition, the geometrical constraints of the apparatus were studied by comparing the Monte Carlo track distributions with the distribution of real data events at several locations in the spectrometer. The agreement was excellent.

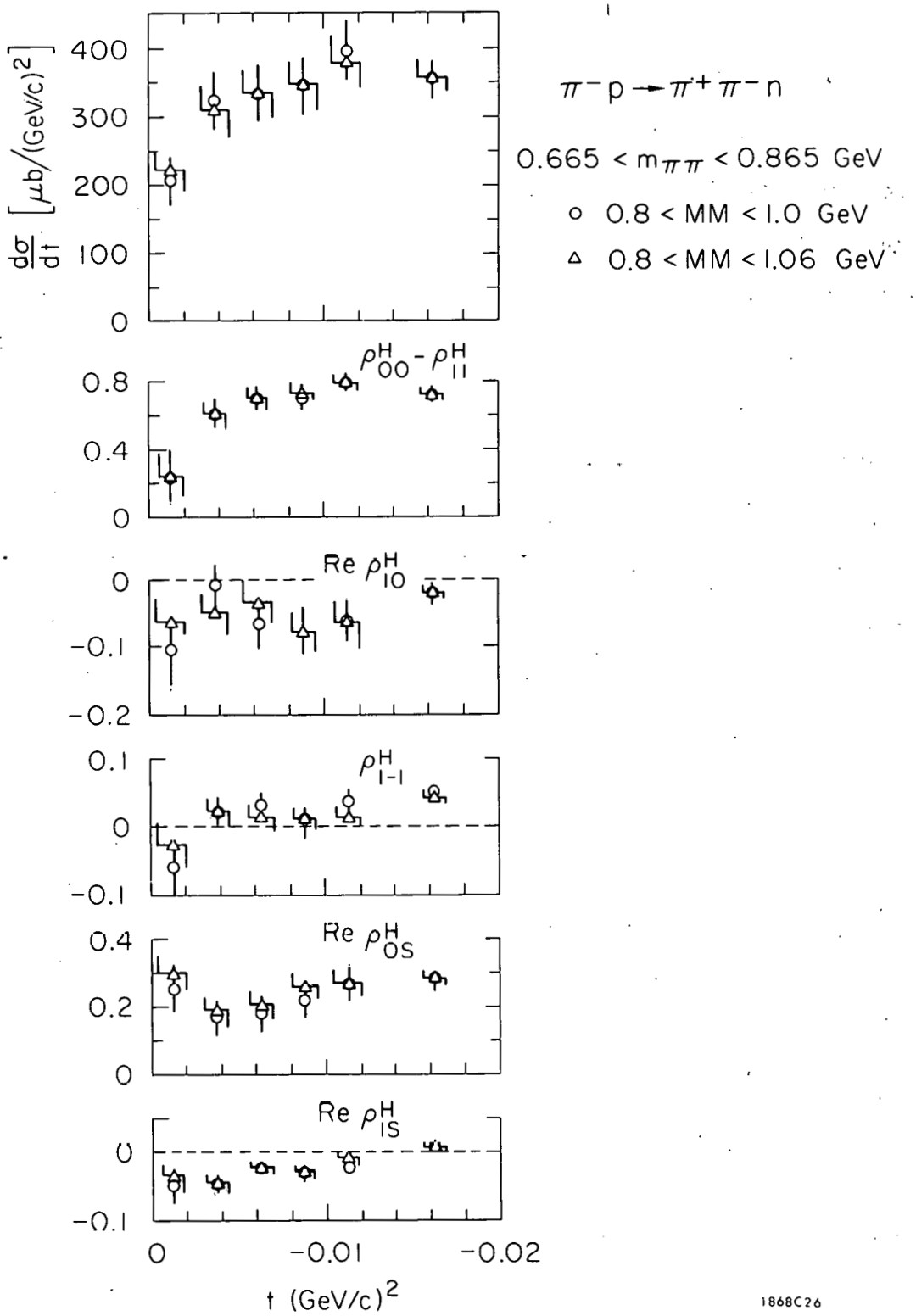

FIG. 24--Comparison of the $\pi^+\pi^-$ density matrix elements and differential cross section in the ρ^0 region ($0.665 < m_{\pi\pi} < 0.865$ GeV) for two different cuts on the missing mass; $0.8 < MM < 1.0$ GeV and $0.8 < MM < 1.06$ GeV.

As another check of the efficiency calculation, we redetermined the density matrix elements using more restrictive geometrical cutoffs than were actually imposed by the apparatus. For example, Fig. 25 compares the results obtained in Section D with those obtained when only tracks which lay outside the plug in all of the front chambers were allowed. The comparison is shown only at small t, since plug effects will be less important elsewhere. The agreement is clearly very good. Additional studies of this type were carried out in which large changes were made in the sizes of the magnet gap and spark chamber plugs. These results were also in good agreement.

The efficiency calculation was also checked by refitting the data while ignoring regions for which the efficiency was less than a given cutoff value (EFFCUT). Figure 26 shows the results of such a fit in the Jackson frame with EFFCUT = 0.1 compared to the results obtained previously. For small values of t, this is approximately equivalent to fitting only the angular region for which $|\cos \theta^J| < 0.5$ (see Fig. 13). The agreement is remarkably good in view of the severe restriction of the fitted angular decay region.

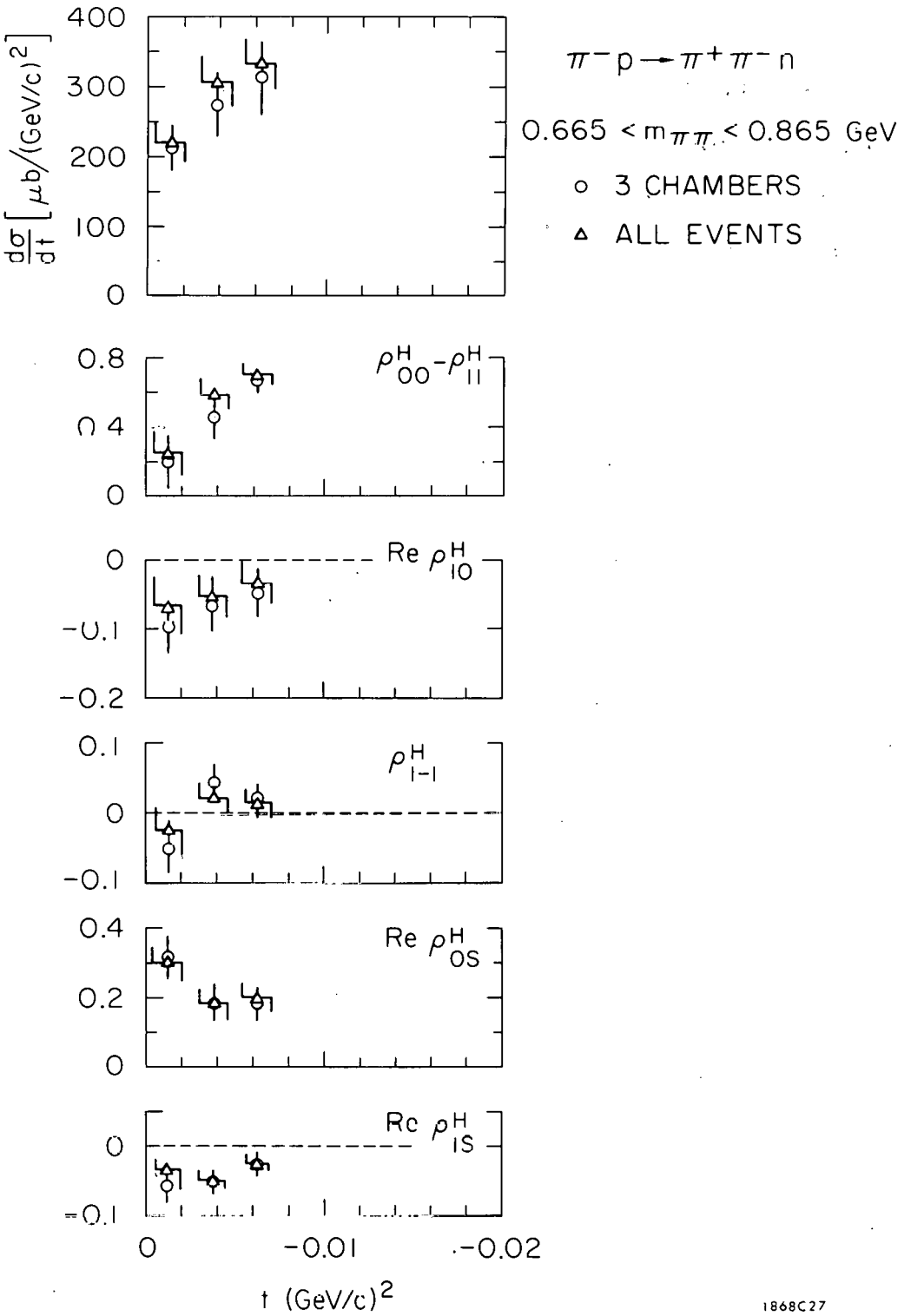

FIG. 25--Comparison of the $\pi^+\pi^-$ density matrix elements and differential cross section in the ρ^0 region ($0.665 < m_{\pi\pi} < 0.865$ GeV) for two different cuts on the spectrometer geometry; the standard event selection and one which allowed no plug hits in the front chambers.

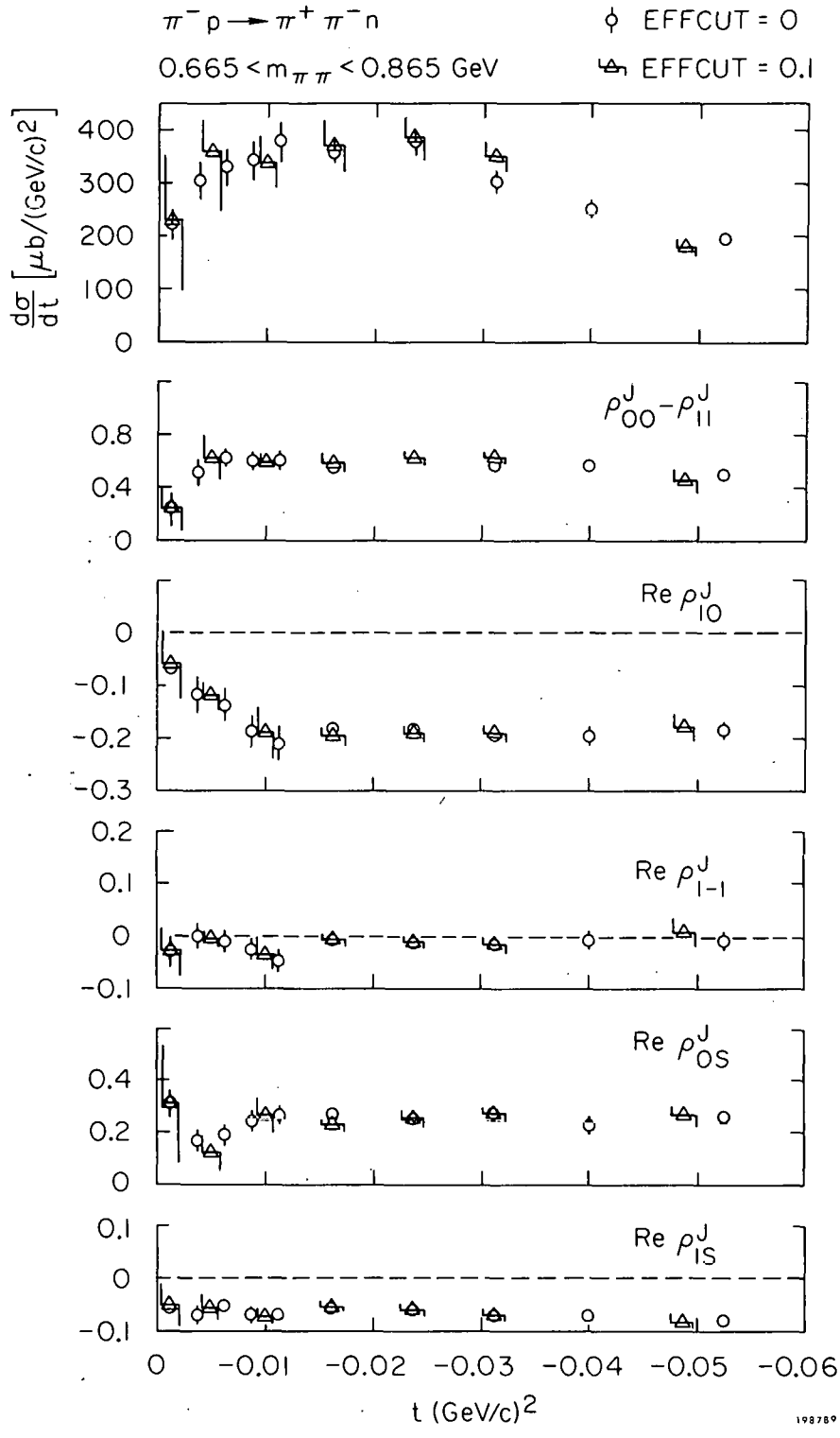

FIG. 26--Comparison of the $\pi^+\pi^-$ density matrix elements and differential cross section in the ρ^0 region ($0.665 < m_{\pi\pi} < 0.865$ GeV) for two different cuts on the efficiency; EFFCUT = 0.0 and EFFCUT = 0.1.

CHAPTER VI

THE VECTOR DOMINANCE MODEL

A. Introduction

We now turn to a comparison of the above data with single-pion photoproduction as a test of the vector dominance model[47] (VDM). Before discussing the results, we present the equations which will be used for these comparisons and discuss the previous work in somewhat greater detail than in Chapter I. Excellent reviews of the previous experiments have been presented at several recent conferences.[18,48]

The VDM predicts the following relationship between the amplitudes for single-pion photoproduction and vector meson production by pions [see Eq. (I.5)]:

$$T(\gamma N \to \pi N) = \sum_{V=\rho,\omega,\phi} \frac{e}{2\gamma_V} T(\pi N \to V_{Tr} N) \quad . \tag{VI.1}$$

Since the experimental results are given in terms of cross sections, we must square both sides of Eq. (VI.1). In general, the vector meson amplitudes can interfere with one another so that the comparison between the cross sections[11] becomes

$$\frac{d\sigma}{dt}(\gamma N \to \pi N) = \frac{1}{2} \sum_{V=\rho,\omega,\phi} \left[\frac{e^2}{4\gamma_V^2} \frac{d\sigma}{dt}(\pi N \to V_{Tr} N) + \text{interference terms} \right] \quad . \tag{VI.2}$$

The extra factor of 1/2 on the right-hand side comes from the average over the initial photon spins. The relative phase space factor has been neglected since its value is approximately one at high energies.

There is no a priori reason to expect that the magnitude of the interference terms will be small. In fact, there is considerable isovector-isoscalar interference in the single-pion photoproduction data[15] which in the VDM implies an interference between the isovector ρ and the isoscalars ω and ϕ. A ρ-ω interference effect is also seen in this experiment (see Chapter VII). The behavior of the interference terms is difficult to calculate so the most reliable procedure is to consider combinations of cross sections where the interference terms cancel. Because of isospin invariance, the relative sign of the isoscalar and isovector amplitudes changes when a π^+ is substituted for a π^-. So when the sum of π^+ and π^- photoproduction is taken in Eq. (VI.2) the ρ-ω and ρ-ϕ interference terms cancel. The coupling of the ϕ to non-strange mesons is small, so we can neglect its contribution in the direct term and in ω-ϕ interference. Equation (VI.2) then becomes[11]

$$\frac{1}{2}\left[\frac{d\sigma}{dt}(\gamma p\to\pi^+ n)+\frac{d\sigma}{dt}(\gamma n\to\pi^- p)\right] = \frac{\pi\alpha}{\gamma_\rho^2}\left[\rho_{11}\right]_\rho \frac{d\sigma}{dt}(\pi^- p\to\rho^o n)+\frac{\pi\alpha}{\gamma_\omega^2}\left[\rho_{11}\right]_\omega \frac{d\sigma}{dt}(\pi^- p\to\omega n) \tag{VI.3}$$

where $\left[\rho_{11}\right]_\rho\left(\left[\rho_{11}\right]_\omega\right)$ is the density matrix element which projects out the transversely polarized $\rho^o(\omega)$ mesons. The photon-vector-meson coupling constants have been measured to be in the ratio[49] $\left(1/\gamma_\rho^2\right):\left(1/\gamma_\omega^2\right) =$ $(7.51\pm 1.52):1$ and $(d\sigma/dt)\,(\pi^- p\to\rho^o n):(d\sigma/dt)\,(\pi^- p\to\omega n)$ is approximately 10:1 in the forward direction at 8 GeV.[50] Assuming that this ratio does not change greatly* at 15 GeV/c, the second term in Eq. (VI.3) contributes only a few percent compared with the ρ^o term and can be ignored. Equation (VI.3)

*The energy dependence of $\sigma(\pi^- p\to\omega n)$ and $\sigma(\pi^+ n\to\omega p)$ is well represented by $1/P^{2.25}$ for energies below 8 GeV (see Chapter VII.D), but the cross section has not been measured at higher energies.

then becomes

$$\frac{(1+R)}{2}\frac{d\sigma}{dt}(\gamma p \to \pi^+ n) = \frac{\pi\alpha}{\gamma_\rho^2}\rho_{11}^H \frac{d\sigma}{dt}(\pi^- p \to \rho^o n) \quad , \qquad \text{(VI.4)}$$

where

$$R = \frac{d\sigma}{dt}(\gamma n \to \pi^- p)/\frac{d\sigma}{dt}(\gamma p \to \pi^+ n)$$

is taken from the π^-/π^+ ratio on deuterium.[15]

The value of the coupling constant $\left(\gamma_\rho^2/4\pi\right)$ can be measured in several different types of experiments.[51] The assumption implicit in the VDM is that $\gamma_\rho^2/4\pi$ is independent of the particular process which is used for its determination or of the mass of the photon at the γ-ρ vertex. However, experimentally the value of the $\gamma_\rho^2/4\pi$ appears to vary by approximately a factor of two for different methods of its determination. Reactions which deal with hadrons in general (e.g., ρ^o production by pions or Compton scattering) seem to require a value between 0.3 and 0.45. On the other hand, values of $\gamma_\rho^2/4\pi \approx 0.7$ are found by ρ photoproduction experiments from complex nuclei. Traditionally, the "canonical" value has been taken from the Orsay[49] storage ring experiment where the photon is on the ρ mass shell. This experiment yields* $\gamma_\rho^2/4\pi = 0.52 \pm 0.03$ which splits the difference between the extremal values rather neatly.

The situation is very confused (and confusing) and the "correct" value to use in making the following comparisons is by no means clear. It would appear that the VDM is violated quantitatively in the simplest possible way; i.e., through a $\gamma_\rho^2/4\pi$ which depends on the process being observed. Yet the model is qualitatively very successful in describing many reactions and even

*Preliminary results from a more recent experiment at Orsay[52] yield the value $\gamma_\rho^2/4\pi = 0.64 \pm 0.06$.

appears to work rather well quantitatively within a factor of 2-3 uncertainty in the normalization. It thus remains of great interest to compare the t dependence of our ρ^o data with single-pion photoproduction in the forward region where the sharp structure should make the differences and similarities in the t dependences very apparent. We will use the value $\gamma_\rho^2/4\pi = 0.5$ for these comparisons. The uncertainty in this value should be remembered when observing the normalization agreement between the two sets of data.

Previous tests of the VDM using Eq. (VI.4) have shown general agreement when the value $\gamma_\rho^2/4\pi \approx 0.4$ is used. For example, Diebold and Poirier[20] find excellent agreement at 4 and 8 GeV/c using the value $\gamma_\rho^2/4\pi = 0.45$ whereas Dar et al.[19] use the value $\gamma_\rho^2/4\pi = 0.4$ and find excellent agreement at 3.4 GeV/c. Many other comparable tests have been published[11,21] with similar results. However, all such tests have been at rather low energies. Moreover, the ρ^o data were not sufficient to determine whether the transverse ρ^o cross section has a forward peak for $-t < m_\pi^2$. Therefore, the previous comparisons have not been sensitive tests of the similarities in the t dependence of the cross sections though they have been quite sensitive to differences in normalization and in the value of $\gamma_\rho^2/4\pi$.

In addition to the above comparison of the ρ^o production data with unpolarized photoproduction, it is also possible to project out the components of linear polarization for the ρ^o which may then be compared with photoproduction data obtained with linearly polarized photons. The VDM then predicts[11,22,23]

$$\frac{1}{2}\left[\frac{d\sigma_\perp}{dt}(\gamma n \to \pi^- p) + \frac{d\sigma_\perp}{dt}(\gamma p \to \pi^+ n)\right] = \frac{\pi\alpha}{\gamma_\rho^2}\left(\rho_{11}^H + \rho_{1-1}^H\right)\frac{d\sigma}{dt}(\pi^- p \to \rho^o n) \tag{VI.5}$$

and

$$\frac{1}{2}\left[\frac{d\sigma_{\parallel}}{dt}(\gamma n \to \pi^- p) + \frac{d\sigma_{\parallel}}{dt}(\gamma p \to \pi^+ n)\right] = \frac{\pi\alpha}{\gamma_\rho^2}\left(\rho^H_{11} - \rho^H_{1-1}\right)\frac{d\sigma}{dt}(\pi^- p \to \rho^o n) \tag{VI.6}$$

where $\sigma_\perp$ ($\sigma_\parallel$) denotes the cross section $d\sigma/dt$ for pions produced in a plane perpendicular (parallel) to the electric vector of the photon, and where we have neglected the small contribution of the other vector mesons as before. Equations (VI.5) and (VI.6) correspond to processes with natural and unnatural-parity exchanged in the t channel.[53]

A consequence of Eqs. (VI.5) and (VI.6) is

$$\frac{\rho^H_{1-1}}{\rho^H_{11}} = \frac{A^+ + RA^-}{1+R}\ , \tag{VI.7}$$

a comparison which is independent of the normalization of the two sets of data; and the value of the rho-photon coupling constant. The asymmetry parameters are defined by

$$A^\pm = \frac{\sigma_\perp^\pm - \sigma_\parallel^\pm}{\sigma_\perp^\pm + \sigma_\parallel^\pm} \tag{VI.8}$$

where, for example, $\sigma_\perp^+$ is the cross section $d\sigma_\perp/dt$ for π^+ photoproduction.

Historically, the polarized photoproduction data were first compared with the ρ^o data using Eq. (VI.7). The comparisons[17,22] showed a very serious discrepancy at 4 GeV/c. The photoproduction asymmetry was found to be approximately 0.5 in the t range 0.2 - 0.4 whereas the ratio of the density matrix elements (ρ_{1-1}/ρ_{11}) was negative when evaluated in the helicity frame.

Several explanations were advanced for this discrepancy within the context of the VDM. Biswas et al.[46] pointed out that the 4 GeV/c data used in the

comparison were inconsistent with the relation $\langle \cos 2\phi \rangle = -3/4\ \rho_{1-1}\ \sin^2\theta$ which should be satisfied if only S and P waves were present. In order to explain this inconsistency, they suggested that a D-wave background contributed significantly to their data sample (see Chapter V.F). However, irrespective of its origin, the presence of this inconsistency in the data suggests that ρ^H_{1-1} may not be well measured which could explain at least part of the disagreement between the ρ^o and polarized photoproduction data.

The failure of Eq. (VI.7) was also explained in terms of frame ambiguities of the VDM. It had been pointed out some time earlier[54] that the frame in which the comparisons should be made was somewhat ambiguous since the helicity of a massive particle is not a Lorentz invariant. Bialas and Zalewski[55] then suggested that the VDM should not be considered to have failed unless no frame could be found which gave agreement. They showed that the asymmetry comparison worked reasonably well in the Donahue-Högassen* frame.

However, Diebold and Poirier[23] pointed out shortly thereafter that the natural-parity comparison [Eq. (VI.5)] is invariant under rotations about the production normal and is therefore independent of any frame ambiguity. They found that the ρ^o cross section at 4 GeV/c was nearly a factor of three smaller than the photoproduction when the value $\gamma_\rho^2/4\pi = 0.5$ was used.

Faced with these difficulties of the VDM, several theorists studied the question of frame ambiguities in detail. Some of these authors used model dependent arguments[56] while others studied the behavior of the invariant amplitudes.[57] Nearly all of these studies came to the same conclusion. In the high energy limit, the VDM relations should be exact provided that the

*Defined as the frame for which Re $\rho_{10} = 0$.

density matrix elements are expressed in the helicity frame. On the other hand, at lower energies some discrepancies would be expected and the frame in which the comparisons should be made is no longer well defined. The energy at which the helicity frame comparisons become correct is not well determined in a model independent way. However, several different models[56] suggest that the comparisons should work well at 15 GeV/c but will be badly violated at 4 GeV/c. Thus, the comparisons here, which use 15 GeV/c data, should be more definitive than the previous comparisons at lower energy.

B. Data

In Chapter V, we presented the density matrix elements for the reaction $\pi^- p \to \pi^+ \pi^- n$. The VDM comparisons, however, require the density matrix elements and differential cross section for the reaction $\pi^- p \to \rho^o n$. These were obtained from the measured dipion quantities by subtracting the S wave and imposing the new normalization condition

$$2\rho_{11} + \rho_{00} = 1 \quad .$$

As discussed previously, the S-wave cross section was assumed to be of the form

$$\frac{d\sigma}{dt}(\text{S wave}) = \frac{B|t|}{\left(t - m_\pi^2\right)^2} \; e^{7t} \qquad \text{(VI.9)}$$

as obtained from the data of Sonderegger and Bonamy[41] for the reaction $\pi^- p \to \pi^o \pi^o n$ and extrapolated to 15 GeV/c.

The ρ^o density matrix elements obtained in this manner are shown in Fig. 27. The general features are, of course, similar to those observed previously for the dipion system. In particular, ρ_{00}^H has a narrow forward dip for $-t < m_\pi^2/2$ and ρ_{11}^H has a sharp forward peak in the same t region.

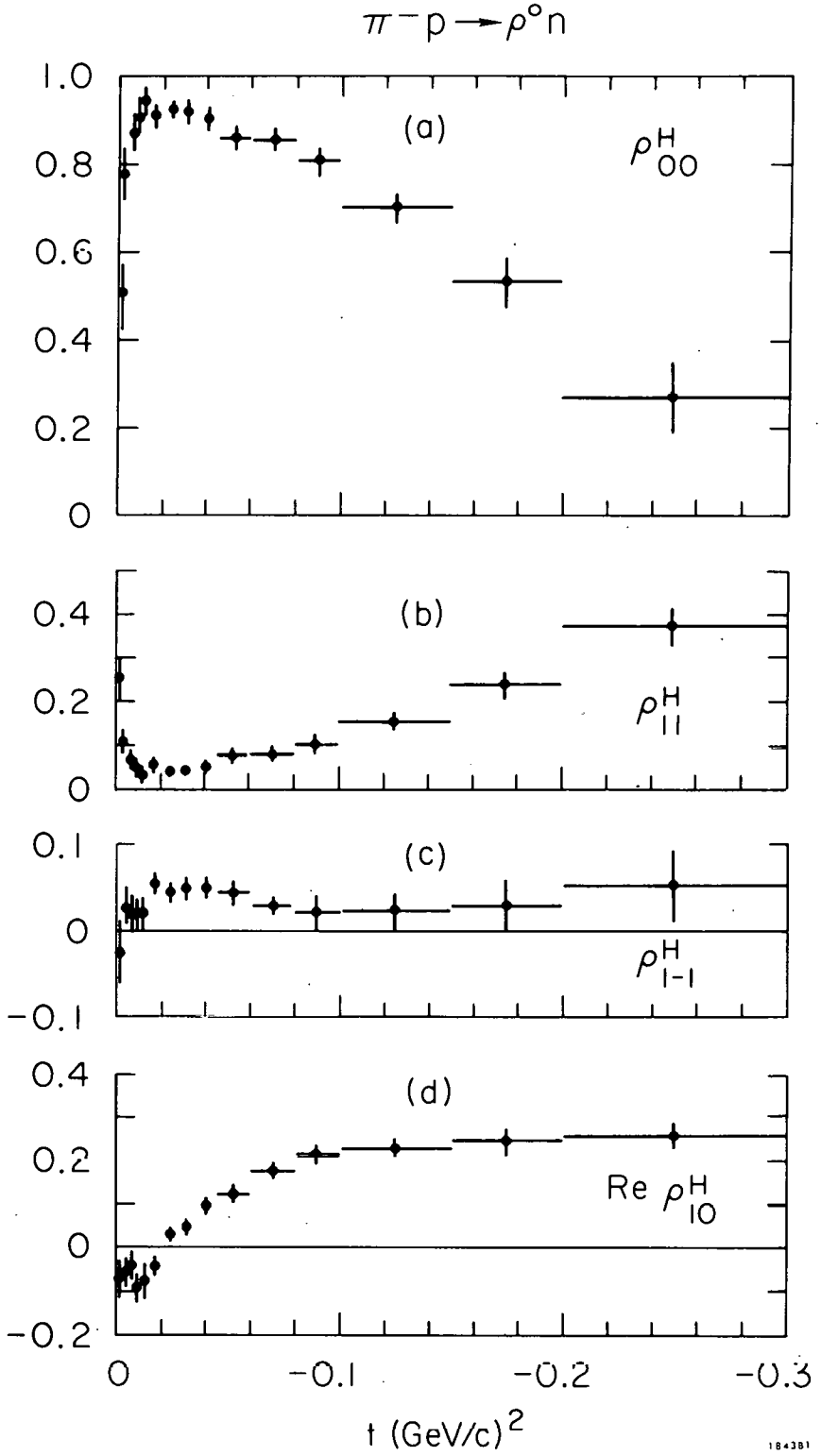

FIG. 27--The density matrix elements in the helicity frame for the ρ^0. The normalization condition is $2\rho_{11}+\rho_{00}=1$.

ρ^H_{1-1} is small and positive everywhere and Re ρ^H_{10} crosses the axis at $-t=m_\pi^2$. The precise values of these density matrix elements depend on the assumptions which were made regarding the S-wave t dependence and normalization (see Chapter V.F). In particular, the value of ρ^H_{11} can change by $\sim 30\%$ in the region around $-t \approx m_\pi^2$ for a different choice of the S wave. However, the remainder of the density matrix elements are essentially unchanged and the general qualitative features are identical for any reasonable choice for the background. The effect which variations in the S-wave subtraction have in the VDM comparisons will be discussed in detail in the following section.

The unpolarized photoproduction data used for the following comparisons were taken from the 16 GeV/c data of Boyarski et al.[15] "Complete" polarized photoproduction experiments have not yet been performed. Moreover, much of the available data is at low energies. The data to be used in this experiment were obtained by combining the measurements of the asymmetry parameter[16,17] [$A^\pm$, see Eq. (VI.8)] at 3.4 GeV/c with the unpolarized cross section at 16 GeV/c. The asymmetry parameter for π^- photoproduction (A^-) has not yet been measured for small values of t so we have assumed that $A^+=A^-$ in this region. Recently, Schwitters et al.[58] have measured A^+ at 12 GeV/c and their results are consistent with the lower energy data. These data were not used directly for the VDM comparison since no A^- measurements were available and since these data do not extend below $-t=0.04$ which is the important region in the present experiment.

C. Results

We now turn to a comparison of the ρ^o results with the single-pion photoproduction data. Figure 28 compares the unpolarized cross sections using Eq. (VI.4). The t dependence of the cross sections is qualitatively similar.

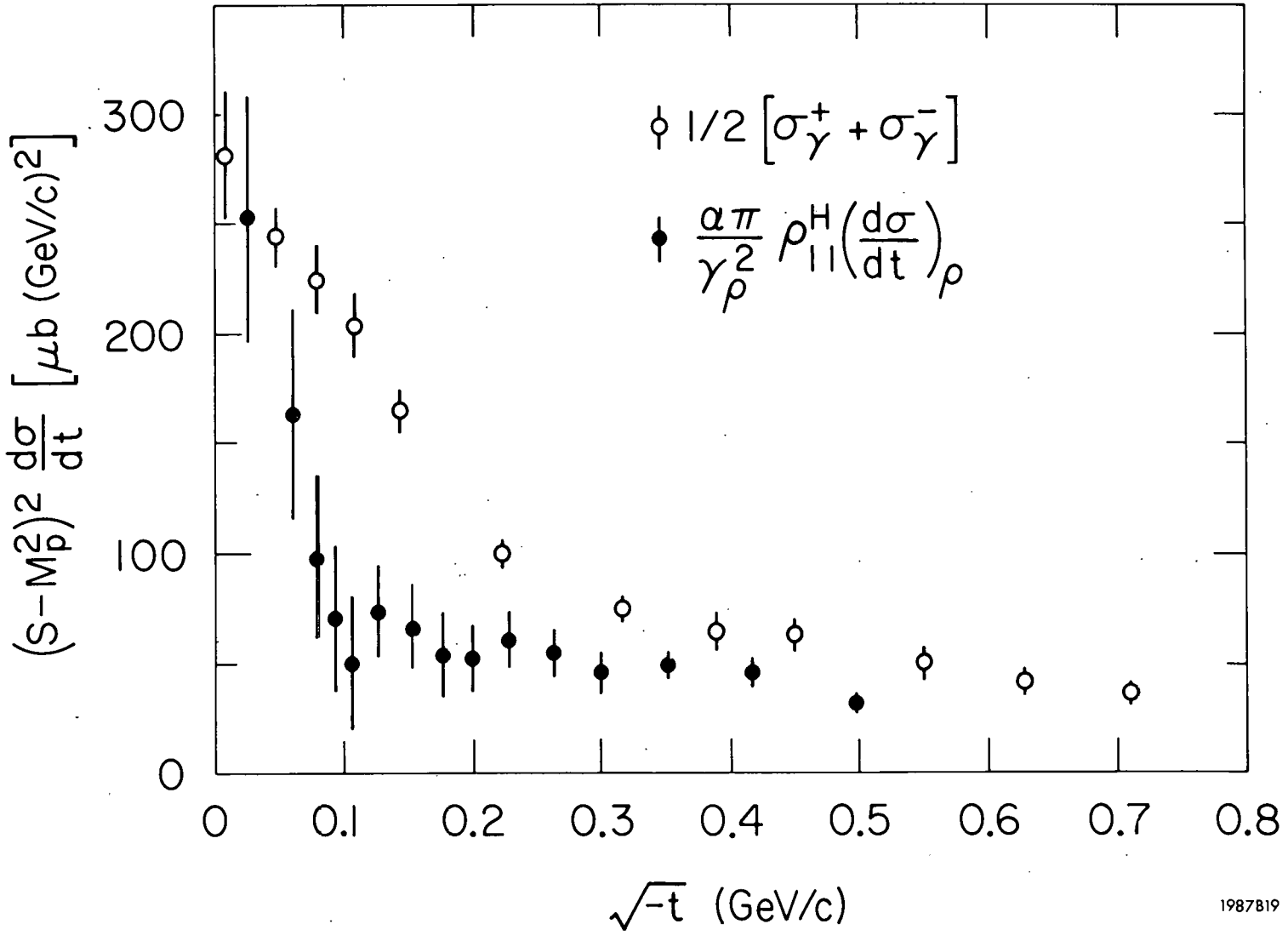

FIG. 28--Transverse differential cross section ($d\sigma/dt$) in the helicity frame for $\pi^- p \to \rho^0 n$ compared with unpolarized single-pion photoproduction data [Eq. (VI.4)].

In particular, both sets of data show a sharp rise in the forward direction. Quantitatively, the forward t=0 cross sections are in good agreement. However, over most of the t region, the ρ^o data lie somewhat below the photoproduction and the forward peak is sharper in the ρ^o data. It should be remembered, however, that there is a ±25% uncertainty in the ρ^o cross section with uncertainties in $\gamma_\rho^2/4\pi$ of at least this magnitude. So the normalization disagreement is rather insignificant.

The shape of the ρ^o forward peak can be brought into closer agreement with the photoproduction by a different choice for the S-wave background. The t region of the greatest sensitivity to the S-wave subtraction is the region $0.1 < \sqrt{t} < 0.2$ GeV/c. Since ρ_{11}^H is small here, any change in the amount of background subtracted will cause significant changes in ρ_{11}^H $(d\sigma/dt)$ in this region and thus will change the shape of the forward structure.

Given Eq. (VI.9), the S-wave normalization as scaled from Sonderegger and Bonamy[41] falls at the upper limits allowed by the condition that the density matrix must be positive definite. In order to demonstrate explicitly the effect of this choice for the normalization, Fig. 29 shows the unpolarized comparison [Eq. (VI.4)] when the S-wave normalization is chosen to be at the opposite extreme, i.e., at the lower limits allowed by the positive definiteness of the density matrix. This figure should be compared with Fig. 28. Little important difference is noted though the shapes of the forward peaks do agree somewhat better in Fig. 29.

The shapes of the cross sections shown in Fig. 29 would agree even more closely if the ρ^o data did not peak as sharply at the very forward points. As was previously noted in Chapter V, the $\pi^o\pi^o n$ data are not sufficient in the forward direction to show that the S-wave cross section goes to zero at t=0.

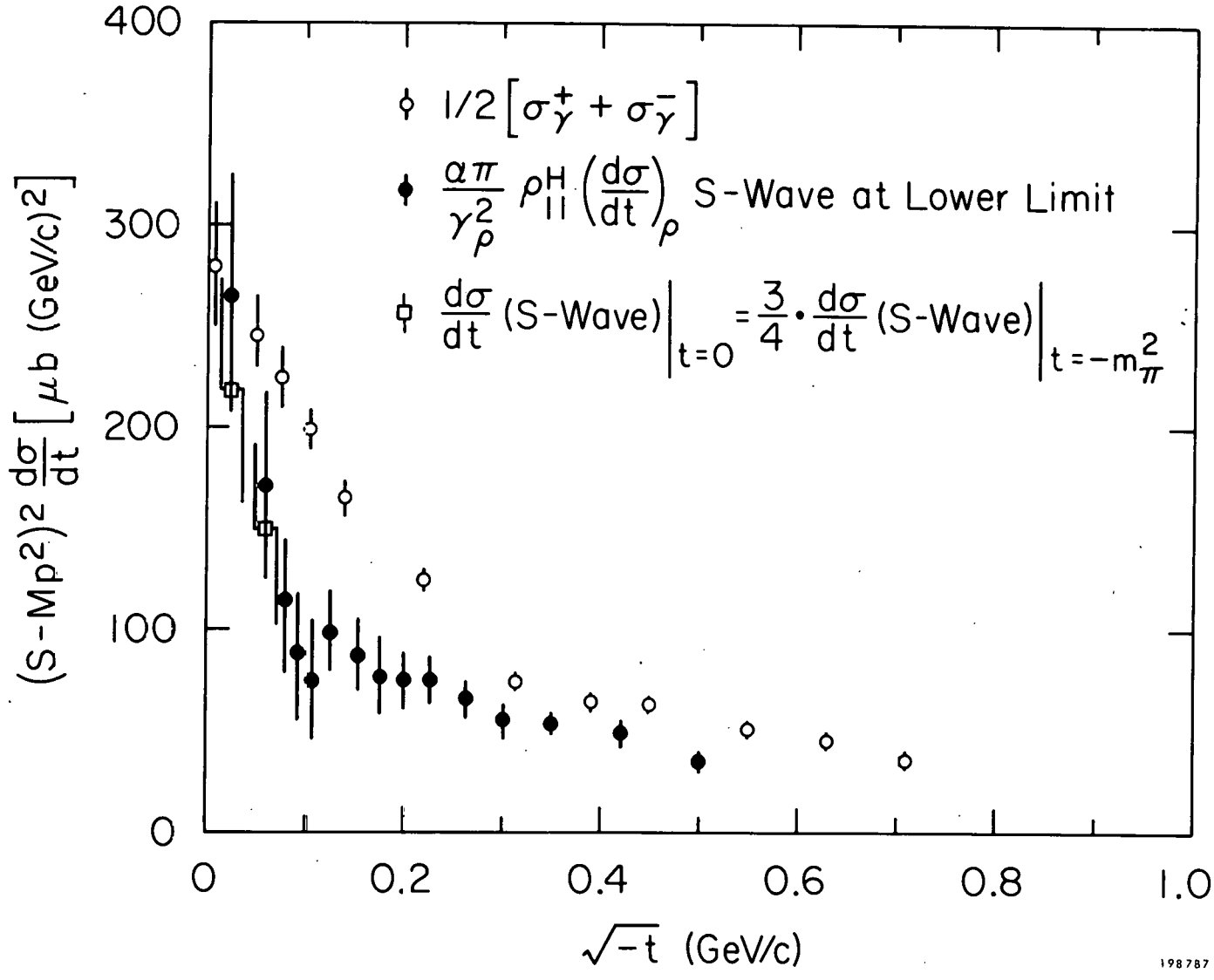

FIG. 29—Transverse differential cross section ($d\sigma/dt$) in the helicity frame for $\pi^- p \to \rho^0 n$ compared with unpolarized single-pion photoproduction data when the S-wave background is chosen to be at the lower limits allowed by the positive definiteness of the density matrix (see discussion in text).

In fact, these data are consistent with an S-wave cross section which only goes down by 25% from $-t=m_\pi^2$ to t=0. Using this as an estimate of the S-wave t dependence causes a change in ρ_{11}^H $(d\sigma/dt)$ at the smallest t values as shown in Fig. 29 and makes the shape of the forward peaks agree more closely. By changing the relative normalizations or the value of $\gamma_\rho^2/4\pi$, the overall agreement can then be made very good. We emphasize that in going from Fig. 28 to Fig. 29, we have made the largest change in the S-wave background that is allowed by this experiment and the $\pi^o\pi^o n$ data. In particular, the sharpness in the forward structure cannot be further reduced by changing the background.

The comparison with the polarized photoproduction data is shown in Figs. 30(a) and (b) which show the natural-[Eq. (VI.5)] and unnatural-[Eq. (VI.6)] parity-exchange contributions, respectively. Once again, the t=0 cross sections are in good agreement. The natural-parity-exchange cross section falls about a factor of two below the photoproduction. However, even this rather poor normalization agreement is better than was previously observed at lower energies.[23] The natural-parity-exchange cross sections display a qualitatively similar shape with the exception of the structure which occurs at $\sqrt{-t} \approx 0.1$ in the photoproduction data. The unnatural-parity-exchange cross section [Fig. 30(b)] shows a dramatic rise for $-t < m_\pi^2$ and the agreement is excellent for $-t < 2m_\pi^2$. For larger values of t, the ρ^o data lie above the photoproduction.

Another comparison using the polarized photoproduction data can be made which is independent of the relative normalizations of the two sets of data. This "asymmetry" comparison [Eq. (VI.7)] is shown in Fig. 31. Both sets of data show dramatic structure for $-t < m_\pi^2$ and the agreement is excellent

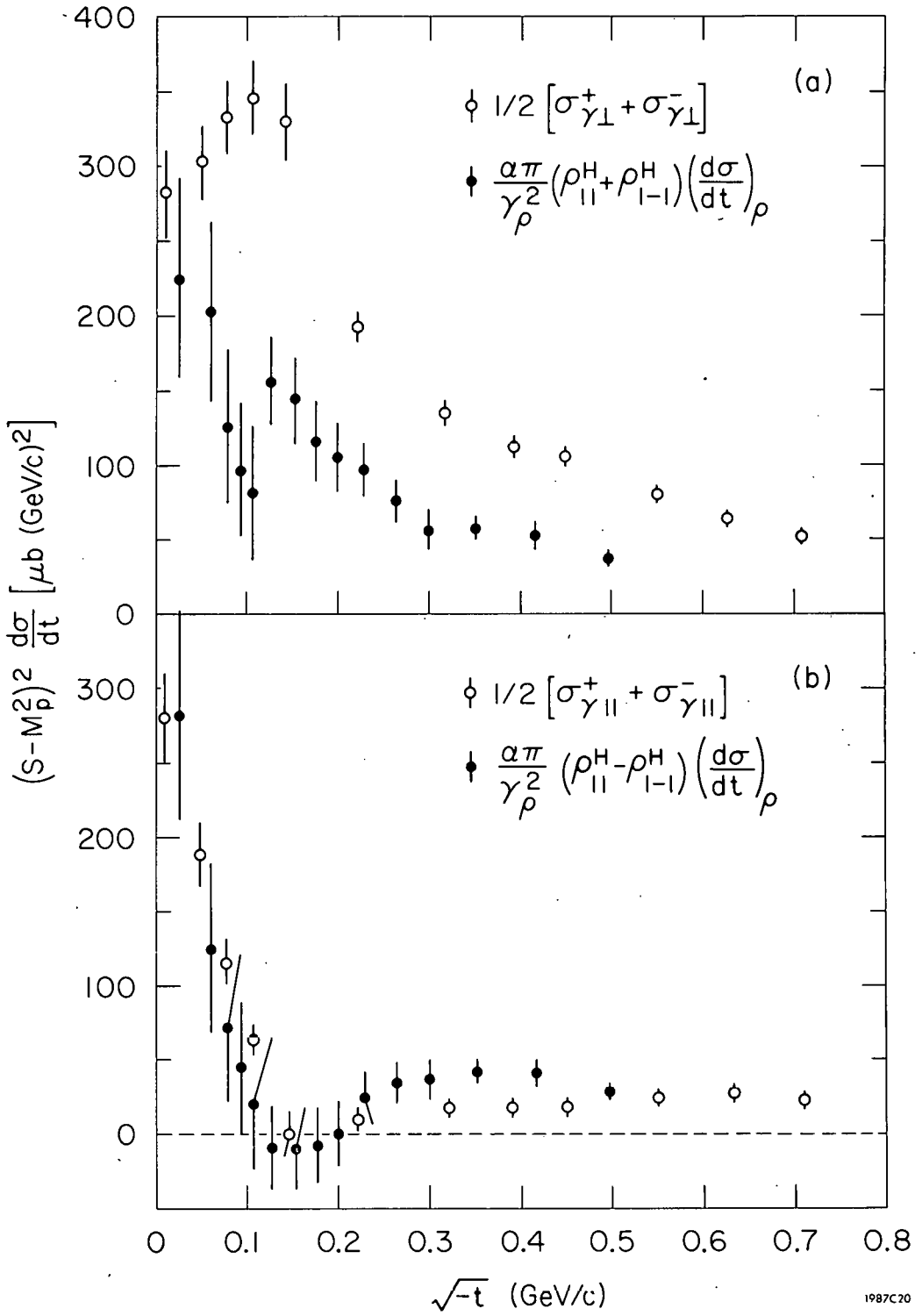

FIG. 30--Comparison of the differential cross sections ($d\sigma/dt$) for linear polarization components of single-pion photoproduction with the reaction $\pi^- p \rightarrow \rho^0 n$, (a) the natural-parity-exchange cross section [Eq. (VI.5)], (b) the unnatural-parity-exchange cross section [Eq. (VI.6)].

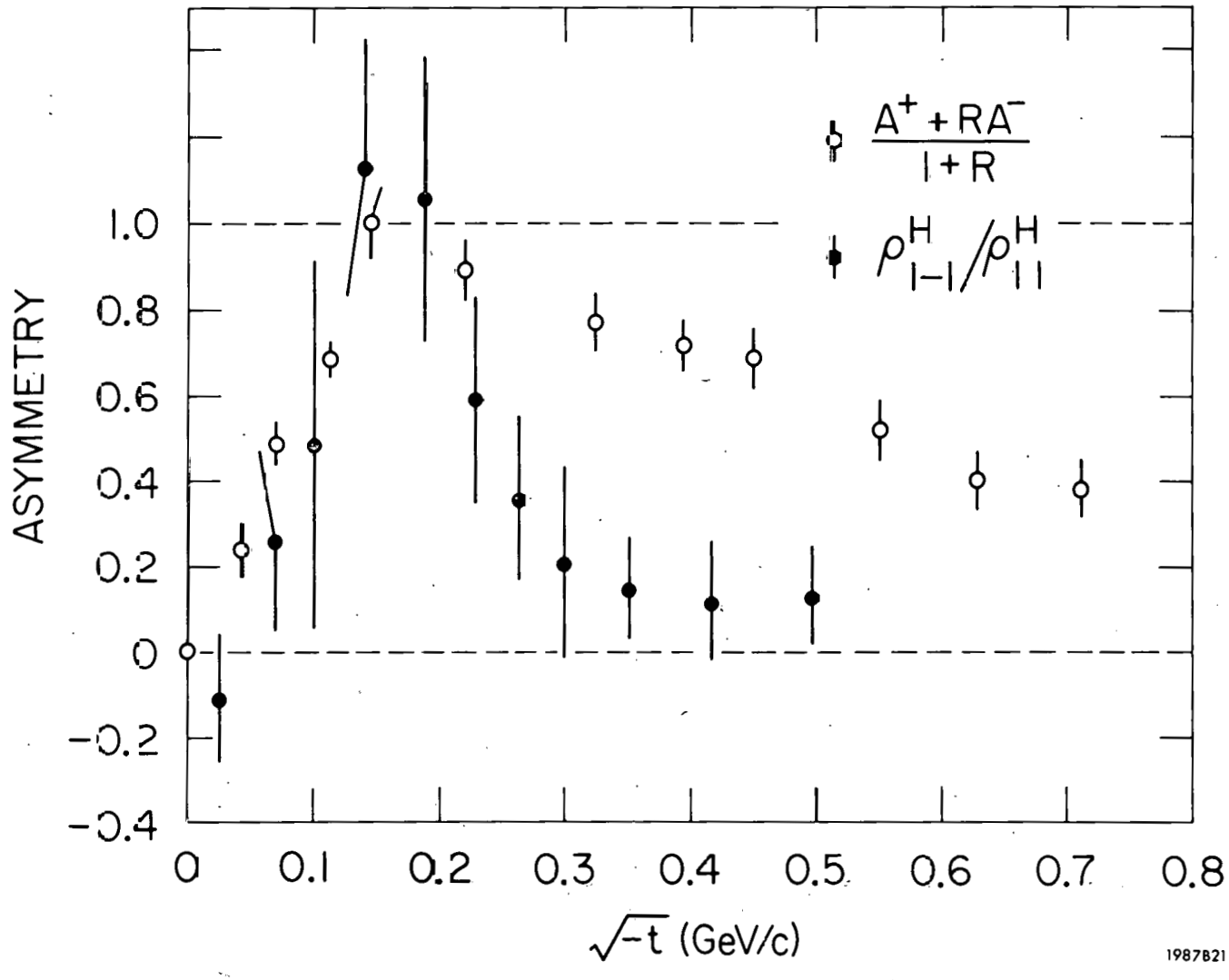

FIG. 31--Comparison of the asymmetries for single-pion photoproduction with $\pi^- p \to \rho^0 n$ [Eq. (VI.7)].

for $-t < 2m_\pi^2$. The asymmetry in the rho data falls more rapidly for larger t but the disagreement for large t is smaller than the previous results[22] at 4 GeV/c.

Considering all of the above comparisons together, we note an overall qualitative agreement. Moreover, the quantitative agreement of some of the comparisons can be dramatically improved if the relative normalizations (or $\gamma_\rho^2/4\pi$) are changed. In addition, some changes can be made in the S-wave subtraction which improve the agreement of the forward structure in the unpolarized comparison as was shown in Fig. 29. However, most of the comparisons cannot be made to agree over the whole t range in this way. For example, the disagreement in the asymmetry comparison (Fig. 31) at larger values of t cannot be changed since the S-wave subtraction has little effect for $-t > 2m_\pi^2$, and the comparison is independent of $\gamma_\rho^2/4\pi$. We thus conclude that in spite of its qualitative success, there is some inadequacy in the simple VDM description of the details of the ρ production process.

Cho and Sakurai[59] have extended the vector dominance model to predict the dominant longitudinal amplitudes for ρ production by pions in addition to the usual predictions of the transverse amplitudes. They assume that a particular set of invariant amplitudes (the Ball[60] amplitudes) are smooth in the vector meson mass and satisfy the constraints imposed by current conservation. These assumptions allow them to relate the longitudinal and transverse helicity amplitudes. Then, by using the VDM and a parameterization of photoproduction (the "pseudomodel" of Jackson and Quigg[61]), they are able to predict both the longitudinal and the transverse ρ cross section and the density matrix elements without any additional parameters.

In Fig. 32, we show both the transverse and total rho cross sections. The dotted line is the input to the calculation of Cho and Sakurai based on the single-pion photoproduction cross sections, while the solid line is their prediction for the total rho cross section. The agreement in the total cross section is good for $-t < 0.1$ (GeV/c)^2 even though the transverse cross sections appear to differ in normalization. Figure 33 shows the prediction of Cho and Sakurai for the ρ^o density matrix elements. The qualitative features are well described by the model though there are some differences in detail. In particular, $\rho^H_{00} - \rho^H_{11}$ has a sharp forward dip and Re ρ^H_{10} crosses the axis at $t \approx -m_\pi^2$ as observed in the data. The strongest disagreement seems to be for ρ^H_{1-1} where the model predicts too large a value. Overall, the agreement is remarkable especially since this model has no adjustable parameters.

D. Conclusion

The rho production results at 15 GeV/c show structure similar to the single-pion photoproduction data. The magnitudes of the forward cross sections are the same and both sets of data show a sharp forward peak and a rapid change in the asymmetry for $-t < m_\pi^2$. In detail, the unnatural-parity-exchange cross section agrees very well, as does the asymmetry for $-t < 2m_\pi^2$. However, as has been noted in previous experiments, the absolute rho cross sections appear to lie below the photoproduction when the value $\gamma_\rho^2/4\pi = 0.5$ is used. The normalization difference is most severe for the natural-parity-exchange cross section though the difference noted here is smaller than has previously been observed at lower energies. There are differences in the sharpness of the observed structure which may be reduced by another choice for the S-wave background. All of the comparisons cannot be made simultaneously to agree in detail, however, by changing the S-wave background or

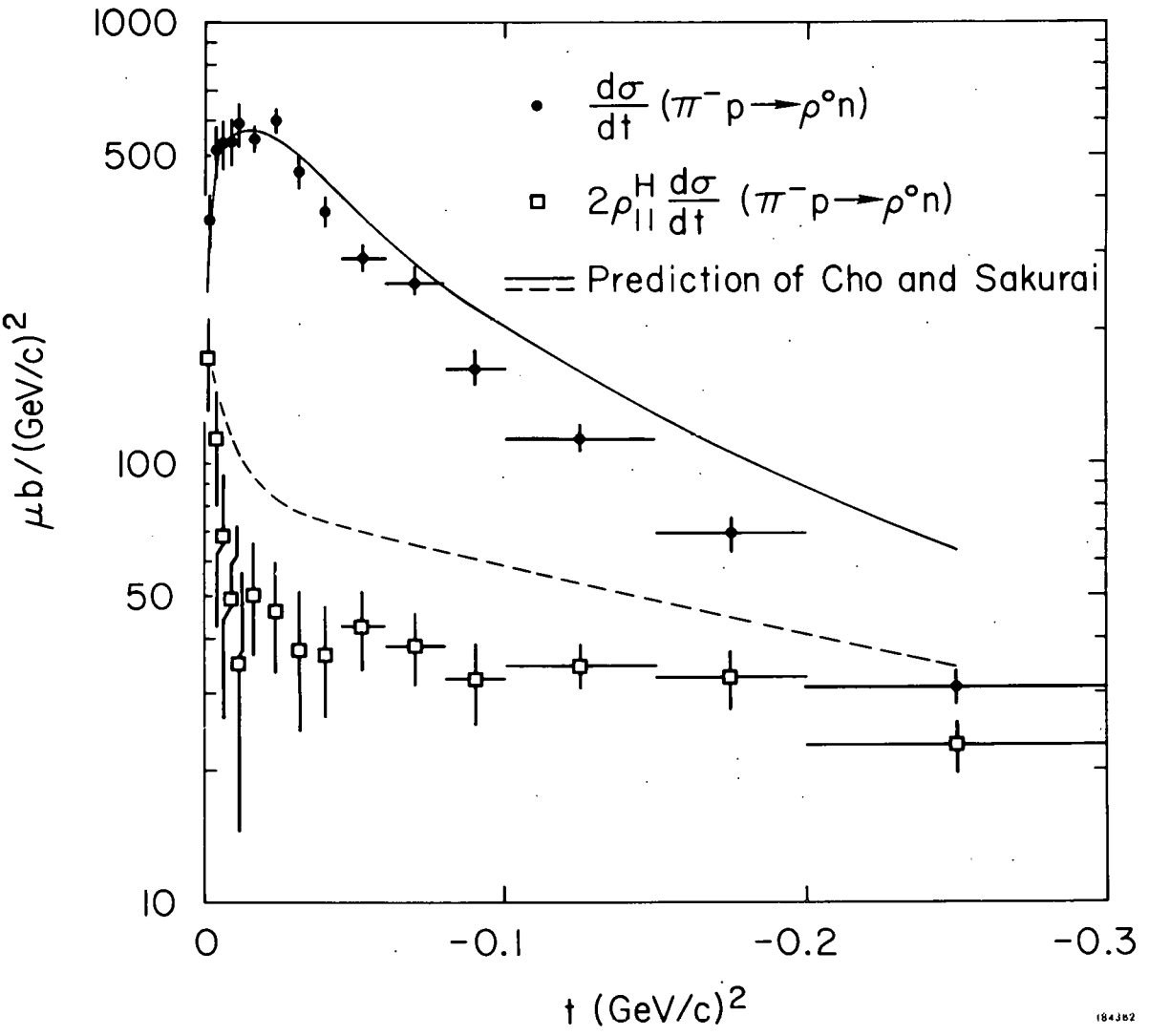

FIG. 32--Total and transverse differential cross sections for $\pi^- p \to \rho^0 n$. The solid line represents the prediction of Cho and Sakurai, and the dotted line represents the input to their calculation.

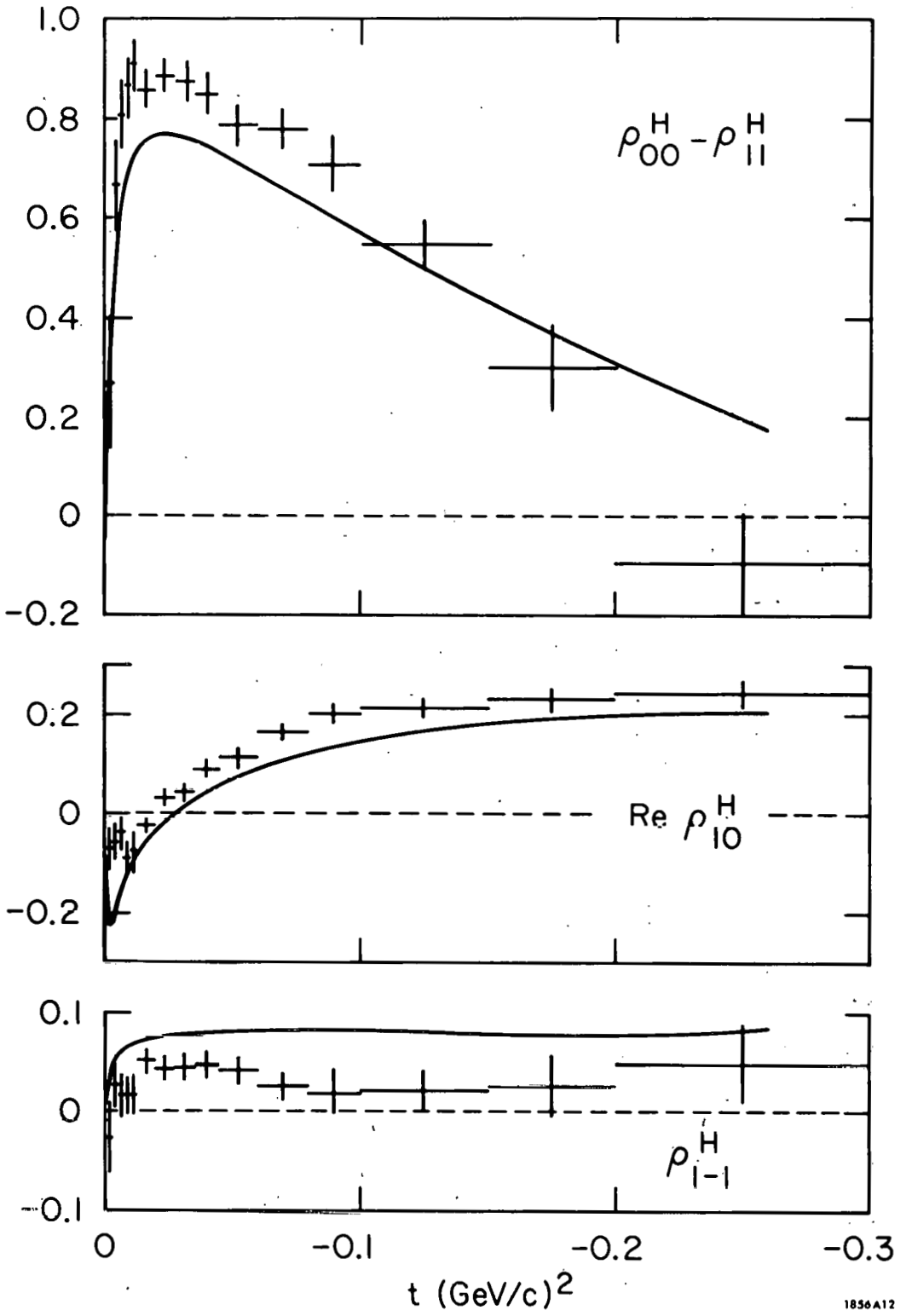

FIG. 33--Density matrix elements in the helicity frame for $\pi^- p \to \rho^0 n$. The solid lines represent the predictions of Cho and Sakurai.

by changing the relative normalization (e.g., change $\gamma_\rho^2/4\pi$) and therefore indicate some inadequacy in the simple VDM description of the details for the rho production process.

CHAPTER VII

ρ - ω INTERFERENCE

A. Introduction

Many theoretical papers[62-64] have dealt with the phenomena of ρ-ω mixing, since the possibility of this effect was first pointed out by Glashow[28] in 1961. There are several alternative approaches to the problem leading to essentially identical results. One of the first complete treatments was carried out by Bernstein and Feinberg[62], who used a time-dependent approach similar to that used earlier by Lee, Oehme, and Yang[65] to discuss the $K^0 - \bar{K}^0$ system. However, unlike the $K^0 - \bar{K}^0$ problem, we are not here interested in the precise time dependence of the amplitudes since the lifetimes of the particles with which we are dealing are so short. Experimentally, the available information is contained in the invariant mass of the dipion system. Bernstein and Feinberg obtain this mass dependence as the Fourier transform of the time dependence. A simpler approach is to view the problem as that of finding the propagator of a two-particle quasi-degenerate system. In this case, the problems reduce to a study of the properties of the mass matrix M. Though we will use a more phenomenological approach for the fitting of our experimental data, it is useful to give a short, simplified outline of this theory here to provide a framework in which to discuss the theoretical predictions.

The amplitude S for the production of a dipion final state can be written

$$S(\pi^+\pi^-) = (A_\rho \; A_\omega) \quad \frac{1}{M - mI} \begin{pmatrix} T_\rho \\ T_\omega \end{pmatrix}. \qquad \text{(VII.1)}$$

A_ρ and A_ω are the vector meson production amplitudes for the pure G-parity vector meson eigenstates $|\rho_0>$ and $|\omega_0>$. T_ρ and T_ω are the corresponding decay amplitudes for these pure states to decay into two pions. m is the

invariant mass of the dipion system and M is the symmetric 2×2 mass matrix

$$M = \begin{bmatrix} Q_\rho & -\delta \\ -\delta & Q_\omega \end{bmatrix} \qquad \text{(VII.2)}$$

with $Q_V = m_V - i\frac{\Gamma_V}{2}$.

In the absence of the electromagnetic interaction $\delta=0$ and the states of pure isospin, $|\rho_0\rangle$ and $|\omega_0\rangle$ are eigenvectors of M. However, in the presence of the electromagnetic interaction, this is no longer true. The physically observable $|\rho\rangle$ and $|\omega\rangle$ become, in this case, a superposition of the pure states,

$$\begin{aligned} |\rho\rangle &= |\rho_0\rangle - \epsilon|\omega_0\rangle \\ |\omega\rangle &= \epsilon|\rho_0\rangle + |\omega_0\rangle \end{aligned} \qquad \text{(VII.3)}$$

to lowest order in ϵ. These physically observable states are the eigenvectors of M so that

$$\epsilon = \frac{\delta}{Q_\rho - Q_\omega} \quad , \qquad \text{(VII.4)}$$

where we have kept only the lowest order term.

In order to find S, we carry out the indicated matrix operations and find

$$S(\pi^+\pi^-) = \frac{A_\rho T_\rho}{Q_\rho - m}\left[1 + \alpha e^{i\Phi}\frac{Q_\rho - m}{Q_\omega - m}\right] . \qquad \text{(VII.5)}$$

In deriving the above, we drop higher order terms and neglect the direct decay amplitude $T_\omega(\omega \to 2\pi)$, which is presumably second order in the electromagnetic coupling constant and hence small compared to the observed effect.

We also note that in the above

$$\alpha = \left| \frac{A_\omega}{A_\rho} \; \frac{\delta}{Q_\rho - Q_\omega} \right| \qquad \text{(VII. 6)}$$

and Φ is the overall phase between the ρ and ω amplitudes.

$$\Phi = \text{Arg} \left(\frac{A_\omega}{A_\rho} \right) + \text{Arg}\, \delta + \text{Arg} \; \frac{1}{Q_\rho - Q_\omega} \quad . \qquad \text{(VII. 7)}$$

In deriving Eq. (VII. 5) we have assumed that A_ω and A_ρ are coherent production amplitudes. This is not generally true in strong interaction experiments. In order to include the incoherent processes, we multiply the cross term in $S(\pi^+\pi^-)$ squared by a "coherency" parameter C whose value is between 0 and 1 [a more quantitative definition of C is given in Eq. (VII. 31) in the following section].

Even though Φ is the phase which is generally determined by experiment, theoretical predictions are made in terms of the relative production phase,

$$\beta = \text{Arg} \left(\frac{A_\omega}{A_\rho} \right) \quad . \qquad \text{(VII. 8)}$$

In order to compare these predictions with the results of experiment, it is necessary to know the value of the remaining terms in the expression for Φ. Several calculations[63, 66] have been made which suggest the phase of δ should be small. In addition,

$$\text{Arg} \; \frac{1}{Q_\rho - Q_\omega} \approx 106^\circ$$

with the variations depending on the choice which is made for the ρ mass and width. Thus, we can write

$$\Phi \approx \beta + 106^\circ \quad . \qquad \text{(VII. 9)}$$

One additional quantity of interest in testing theoretical predictions on the ρ-ω interference effect is the branching ratio for the decay $\omega \to 2\pi$, compared to $\omega \to 3\pi$. In terms of the mixing parameter, this can be written

$$\text{B.R.} = \frac{\Gamma(\omega \to 2\pi)}{\Gamma(\omega \to 3\pi)} = \epsilon^2 \frac{\Gamma_\rho}{\Gamma_\omega} \qquad \text{(VII.10)}$$

Expressing this in terms of the off-diagonal mass matrix element, we find that

$$\text{B.R.} \approx \frac{4\delta^2}{\Gamma_\rho \Gamma_\omega} \qquad \text{(VII.11)}$$

We now turn to the problem of estimating the size of the ρ-ω effect. Gatto[67] has calculated the partial width $\Gamma(\omega \to 2\pi)$ according to the vector dominance model picture,

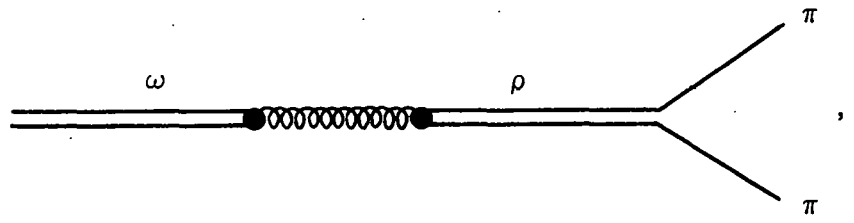

and obtains $\Gamma(\omega \to 2\pi) = 8$ keV. This gives the branching ratio for the direct $\omega \to 2\pi$ decay,

$$\text{B.R.} \approx 0.07\% \quad . \qquad \text{(VII.12)}$$

If this were the magnitude of the effect, it would not yet have been observed experimentally. The size of the observed effect corresponds to a branching ratio which is approximately a factor of 20 larger. Coleman and Glashow[68] have calculated the value of the off-diagonal mass matrix element in terms of the medium-strong SU(3)-breaking mass splitting for meson and baryon multiplets. They predict that $\delta \approx 2.5$ MeV. Using Eq. (VII.11), we see that this corresponds to a branching ratio,

$$\text{B.R.} \approx 1.5\% \quad . \qquad \text{(VII.13)}$$

Other authors[30, 63, 66] making somewhat different assumptions have estimated from SU(3) and SU(6) arguments that $\delta \approx 2.5 - 5.0$ MeV, which corresponds to a branching ratio in the range

$$\text{B.R.} \approx 1.5 - 3.0\% \quad . \tag{VII.14}$$

The relative phase between the ρ and ω production amplitudes in the strong interactions has been predicted by Goldhaber, Fox, and Quigg[64] on the basis of π-B exchange degeneracy. They assume that the reaction $\pi^- p \to \rho^0 N$ is dominated by π exchange whereas the corresponding reaction $\pi^- p \to \omega N$ is dominated by B exchange.* This latter assumption is not expected to hold well at high energies, since ρ exchange should become increasingly important. However, at low energies, the predictions might be expected to be valid. The relative production phase in the reaction $\pi^- p \to \pi^+ \pi^- n$ is then expected to be

$$\beta \approx -90^\circ \tag{VII.15}$$

which implies an overall phase

$$\Phi = \beta + 106^\circ \approx 16^\circ \quad . \tag{VII.16}$$

Hagopian et al.[32] have investigated this reaction at 2.3 GeV/c and have obtained a peak centered at the ω mass. The observation of a peak makes it difficult to determine a phase unambiguously since it is clearly impossible to experimentally distinguish between the cases where the coherency C=1 with $\Phi = 0$, and $C \approx 0$, Φ = anything. The phase is, however, well determined if $C \geq 0.4$ and takes on the value $\Phi = -15^\circ \pm 30^\circ$ in agreement with the prediction of Goldhaber, Fox, and Quigg. Results from two other $\pi^+ \pi^- n$ experiments[69] have been reported in preliminary form and the results are reported to agree with those of Hagopian et al. Dalpaiz et al. have presented data at 1.65 GeV/c,

*N denotes the missing baryon.

whereas Rangaswamy et al. have reported data from momenta between 3 and 5 GeV/c. Dalpaiz et al. quote a phase $\Phi = -4 \pm 20^{\circ}$; Rangaswamy et al. show a mass spectrum with a 3 σ bump in the 780 - 800 MeV mass bin. Since the results of both of these experiments have yet to be published, however, it is difficult to judge the significance of these observations.

Many other experiments have been reported for a wide variety of reactions. Essentially all of these experiments have been carried out below 7 GeV. Excellent reviews of the experimental situation, as well as a short theoretical discussion, are available in the reviews of Goldhaber,[30] Marshall,[66] and Roos.[70]

B. Fitting Formalism

We will now develop the general formalism which has been used to fit the ρ-ω data. Because of the nonuniform acceptance of the experimental apparatus, this formalism differs somewhat from that described in the literature. In order to make clear the various assumptions which have been made, we will derive our fitting forms in somewhat pedantic detail. It should be stated at the outset that we are here concerned only with the discovery and parameterization of an anomaly in the ω region. No attempt will be made to determine the "correct" parameters for the ρ^{o} meson. Indeed, it is well known, and we will again implicitly show, that the assumption of different background or ρ^{o} shapes can change the fitted ρ^{o} parameters substantially. Because of the narrowness of the ω meson, however, any interference effect is dominated by the ω shape. Thus, the fitted ρ^{o} mass and width are rather unimportant in determining the interference parameters.

A general amplitude for two-pion production can be written as

$$A_{2\pi} = A_{\rho} + A_{\omega} + A_{B} \quad . \tag{VII.17}$$

A_ρ (A_ω) represents the ρ^0 (ω) contribution to the amplitude and A_B is the background amplitude. If we suppress the spin variables, these amplitudes are in general functions of the dipion invariant mass (m), the polar (θ) and azimuthal (ϕ) angles in the dipion rest frame, and the momentum transfer (t). This is,

$$A_{2\pi} = A_{2\pi}(\theta, \phi, m, t) \quad . \tag{VII.18}$$

We now separate the decay mass shape out of the amplitudes.

$$\begin{aligned} A_\rho(\theta, \phi, m, t) &= a_\rho(\theta, \phi, m, t)\ M_\rho(m) \\ A_\omega(\theta, \phi, m, t) &= a_\omega(\theta, \phi, m, t)\ M_\omega(m) \\ A_B(\theta, \phi, m, t) &= a_B(\theta, \phi, m, t)\ M_B(m) \end{aligned} \tag{VII.19}$$

$M_v(m)$ is a Breit-Wigner amplitude similar to that defined by Pisut and Roos,[44]

$$M_\rho \propto \frac{m}{q}\ \frac{m_\rho \Gamma_\rho}{m_\rho^2 - m^2 - i m_\rho \Gamma_\rho} \tag{VII.20}$$

where the notation is given in Eq. (V.15). Because the ω is so narrow, we drop the m/q factor in the M_ω term, giving

$$M_\omega \propto \frac{m_\omega \Gamma_\omega}{m_\omega^2 - m^2 - i m_\omega \Gamma_\omega} \tag{VII.21}$$

with Γ_ω = constant. For simplicity, we assume here that the interaction range parameter ($\bar{R}$) equals zero. The form of the background amplitude is not known, so we will ignore its shape at this stage of the discussion.

The square of the amplitude is now given by

$$|A_{2\pi}|^2 = |a_\rho M_\rho|^2 + |a_\omega M_\omega|^2 + |a_B M_B|^2 + 2\,\mathrm{Re}(a_\rho^* M_\rho^* a_\omega M_\omega)$$

$$+ 2\,\mathrm{Re}(a_\rho^* M_\rho^* a_B M_B) + 2\,\mathrm{Re}(a_\omega^* M_\omega^* a_B M_B) \quad . \qquad \text{(VII.22)}$$

However, since the acceptance efficiency of the spectrometer system is smaller than one, the actual observed amplitude squared (O) is a product of the acceptance efficiency $E(\theta, \phi, m, t)$ and $|A_{2\pi}|^2$. That is,

$$O(\theta, \phi, m, t) = E(\theta, \phi, m, t) \cdot |A_{2\pi}(\theta, \phi, m, t)|^2 \quad . \qquad \text{(VII.23)}$$

Since in this case we wish to fit the observed distribution as a function of m only, we integrate over the remaining variables as follows:

$$O(m) = \int O(\theta, \phi, m, t)\, d\cos\theta\, d\phi\, dt = \int E|A_{2\pi}|^2\, d\Omega\, dt. \qquad \text{(VII.24)}$$

We now define

$$E_x(m) = \frac{\int E(\theta, \phi, m, t)\,|a_x|^2\, d\Omega dt}{\alpha_x^2} \qquad \text{(VII.25)}$$

with

$$\alpha_x^2 = \int |a_x|^2\, d\Omega dt \quad , \qquad \text{(VII.26)}$$

and consider the ρ-ω interference term in Eq. (VII.24). Using Eq. (VII.22), we have

$$\rho\text{-}\omega \text{ term} = 2\,\mathrm{Re}\left(\int E\, a_\rho^* a_\omega M_\rho^* M_\omega d\Omega dt\right) \qquad \text{(VII.27)}$$

where M_v is a function of m only. If we now introduce a phase angle $\Phi'_{\omega\rho}$ such that

$$a^*_\rho a_\omega = e^{i\Phi'_{\omega\rho}(\theta, \phi, m, t)} |a_\rho||a_\omega| \ . \qquad \text{(VII.28)}$$

Equation (VII.27) becomes†

$$\rho\text{-}\omega \text{ term} = 2 \text{ Re}\left[M^*_\rho(m)\ M_\omega(m) \int E\ |a_\rho||a_\omega|\ e^{i\Phi'_{\omega\rho}}\ d\Omega dt\right] . \qquad \text{(VII.29)}$$

We now note that

$$\int E|a_\rho||a_\omega|\ e^{i\Phi'_{\omega\rho}}\ d\Omega dt \le \left[\int E|a_\rho|^2\, d\Omega dt \cdot \int E|a_\omega|^2\, d\Omega dt\right]^{1/2} \qquad \text{(VII.30)}$$

so that by defining a coherency parameter ($C_{\omega\rho}$) which lies between zero and one and also an average phase angle ($\Phi_{\omega\rho}$), we can write the interference term (Eq. VII.27) as

$$\rho\text{-}\omega \text{ term} = C_{\omega\rho}\alpha_\rho\alpha_\omega\ \sqrt{E_\rho E_\omega}\ \text{Re}\left(e^{i\Phi_{\omega\rho}} M^*_\rho M_\omega\right) . \qquad \text{(VII.31)}$$

Finally, using analogous definitions for the other interference terms, we write the observed amplitude squared as follows:

$$\begin{aligned} O(m) = {} & \alpha^2_\rho E_\rho |M_\rho|^2 + \alpha^2_\omega E_\omega |M_\omega|^2 + \alpha^2_B E_B |M_B|^2 \\ & + 2C_{\omega\rho}\alpha_\rho\alpha_\omega\ \sqrt{E_\rho E_\omega}\ \text{Re}\left(e^{i\Phi_{\omega\rho}} M^*_\rho M_\omega\right) \\ & + 2C_{B\rho}\alpha_B\alpha_\rho\ \sqrt{E_B E_\rho}\ \text{Re}\left(e^{i\Phi_{B\rho}} M^*_\rho M_B\right) \\ & + 2C_{B\omega}\alpha_B\alpha_\omega\ \sqrt{E_B E_\omega}\ \text{Re}\left(e^{i\Phi_{B\omega}} M^*_\omega M_B\right) . \end{aligned} \qquad \text{(VII.32)}$$

†In terms of helicity amplitudes, a dependence of Φ on (θ or ϕ) arises because the different helicity amplitudes can have different relative phases between ρ and ω. It should be remembered that nucleon helicities have been suppressed.

In principle, the coefficients (α, C, Φ) can be functions of the mass. However, we will assume that they are slowly varying in the region of the ω meson. Equation (VII.32) has more parameters than can be determined by present-day experiments, especially in view of the lack of theoretical knowledge of the background distribution. Therefore, in order to derive a fitting function, some simplifying assumptions must be made.

Historically, there are two major sets of such assumptions which have been used. The more general formulation was first used by Flatté.[29]

Flatté assumed that the background distribution was slowly varying compared to the ρ and ω distributions. It was then noted that the behavior of an interference term is dominated by the most rapidly varying part of that term. This means that in practice the terms multiplied by $C_{\omega\rho}$ and $C_{B\omega}$ in Eq. (VII.32) are indistinguishable† and so can be combined. Secondly, it was pointed out that the imaginary part of a Breit-Wigner amplitude is essentially identical to a Breit-Wigner squared. This means that the product of the imaginary part in the interference terms can be combined with the squared terms.†† Under these assumptions we find

$$O(m) = \alpha_1 E_\rho |M_\rho|^2 + \alpha_2 E_\omega |M_\omega|^2 + \alpha_3 E_B |M_B|^2 + \alpha_4 \sqrt{E_\rho E_B}\, \mathrm{Re}(M_\rho) + \alpha_5 \sqrt{E_\rho E_\omega}\, \mathrm{Re}(M_\omega) \qquad \text{(VII.33)}$$

†If the ρ and ω have nearly identical masses, as they do in the present experiment when Eq. (VII.33) is used, then this is no longer a very good assumption. However, with the available statistics, the breakdown of the assumption is difficult to observe and is of minor importance in the fitting process so it will be neglected.

††Note that $\mathrm{Re}(AB) = \mathrm{Re}(A)\,\mathrm{Re}(B) - \mathrm{Im}(A)\,\mathrm{Im}(B)$.

where we have assumed implicitly that the efficiencies are approximately proportional in the ω region. This is well satisfied for the present experiment. We will call Eq. (VII.33) the F (Flatté) fitting form.

The major advantage of the above form is that it is capable of representing any degree of coherence of the amplitudes. However, it also has the strong disadvantage that two of the most interesting parameters which describe the interference effect, namely, the coherence between the ρ and ω amplitudes and the overall phase between them, are no longer available from the fit.

In order to determine these parameters, we assume that the background is incoherent with the ρ and ω amplitudes, i.e., the parameters $C_{B\rho}$ and $C_{B\omega}$ in Eq. (VII.32) are zero. It is known from the density matrix fits of Chapter V that $14 \pm 5\%$ S wave is required for $0.1 < |t| < 0.3\,(\mathrm{GeV/c})^2$, the region where the ρ-ω interference effect is most pronounced. This is very similar to the amount of background ($\sim 13\%$) required to fit the mass distribution when a simple polynomial background shape is assumed. Hence, it is quite reasonable that the background underneath the ρ is largely S wave and therefore incoherent with the P-wave vector mesons if the entire decay angular region is included with uniform efficiency. Since the efficiency across the angular distribution is not uniform, there could still be interference in this experiment. However, for reasonable decay angular distributions, the S-P interference in m will be small for symmetric cuts on the angular region. In addition, the background amplitude is much smaller than the ρ. Thus, we assume that we can neglect the terms multiplied by $C_{B\rho}$ and $C_{B\omega}$ in

Eq. (VII.32), giving

$$O(m) = \alpha_\rho^2 E_\rho |M_\rho|^2 + \alpha_\omega^2 E_\omega |M_\omega|^2 + \alpha_B^2 E_B |M_B|^2$$

$$+ 2C\alpha_\rho \alpha_\omega \sqrt{E_\rho E_\omega}\, \mathrm{Re}\left(e^{i\Phi} M_\rho^* M_\omega\right) \qquad \text{(VII.34)}$$

where we have changed notation such that $C=C_{\omega\rho}$ and $\Phi=\Phi_{\omega\rho}$. We call this the P(phase) form.

The actual mass spectrum is obtained by multiplying the experimental amplitude squared by a phase space factor, which in this case is proportional to the pion momentum in the dipion rest frame (q), and by the width of the data bins (Δm). Thus, the mass spectrum is given by

$$\frac{dN(m)}{dm} = q \cdot O(m) \cdot \Delta m \qquad \text{(VII.35)}$$

where O(m) is given by either Eq. (VII.33) or (VII.34).

At this point of the discussion, we have not yet defined the shape of the background mass distribution. As we have shown in Chapter V, it is possible to satisfactorily fit the mass distribution, assuming a broad resonance shape for the background. However, there is no strong justification here for so doing. In the fitting of the mass spectrum, the background interacts strongly with the determination of the ρ^o parameters but does not materially affect the significance or phase of any ρ-ω effect which may be present. Thus, for simplicity, we parameterize the background as a polynomial in mass

$$\alpha_B^2 \cdot |M_B|^2 = a + bm \quad . \qquad \text{(VII.36)}$$

In order to carry out the fits, a binned maximum-likelihood technique similar to that described in Chapter V is used. This allows fits to be done

with sufficiently small bin widths that bin size effects are negligible. Experimental resolution ($\sigma \sim 8$ MeV) is folded into the fitting function by numerical techniques.

E_ρ is calculated using the fitted ρ^0 density matrix elements from the experiment. For simplicity, the background efficiency is calculated assuming a uniform decay angular distribution. Since the $\omega \to 3\pi$ decay is not observed in this experiment, E_ω is calculated assuming the density matrix elements and $d\sigma/dt$ as determined by Matthews et al.[71] in the reaction $\pi^+ n \to \omega p$ at 7 GeV/c. In practice, these assumptions about the forms of the decay distributions are not important in the fitting process. This results from the fact that for any reasonable decay angular distribution, the efficiencies are approximately proportional in the ω region; i.e., $E_\rho(m) \propto E_\omega(m) \propto E_B(m)$. Hence, the significance of the ω signal and the values of the coherence and phase are insensitive to the angular distributions of the amplitudes. Only the branching ratio depends strongly on the efficiencies and the estimated systematic error due to this effect will be included in the results.

C. Data

The reaction of interest here is

$$\pi^- p \to \pi^+ \pi^- n \quad . \tag{VII.37}$$

The data sample which will be studied is identical to that described in Chapter V which was used to obtain the dipion density matrix elements. This sample contains ~ 8400 events for the mass range $500 < m_{\pi\pi} < 1000$ MeV. Because of the highly peripheral nature of the interactions and an experimental falloff of the acceptance for large values of momentum transfer, nearly all of the events (~ 8000) lie in the momentum transfer region $|t| < 0.3$ $(\text{GeV/c})^2$, which is

the region where the most dramatic ρ-ω interference effects have been observed previously. Because the acceptance of the spectrometer system is nonuniform, care must be exercised in drawing conclusions from the observation of the raw data distributions only. However, if the qualitative features of the acceptance are kept in mind, little difficulty ensues. In particular, the following features of the acceptance in the helicity frame should be noted:

1. The acceptance is ~ 0 for $|\cos \theta^H| > 0.8$ and has its largest value at $\cos \theta^H \approx 0$ with the result that the raw data distributions are enriched with transverse vector meson decays.
2. If the acceptance is averaged for $0.1 < |t| < 0.3$ $(\text{GeV/c})^2$ over a uniform distribution in t and ϕ, the acceptance increases by approximately a factor of two between $|\cos \theta^H| = 0.75$ and $\cos \theta^H = 0$.
3. The acceptance falls slowly with increasing mass. The slope of this falloff in the ω region is similar for different regions of (θ, ϕ) which implies that $E_\rho(m) \propto E_\omega(m) \propto E_B(m)$ as noted previously.

We show in Fig. 34 the $\pi^+\pi^-$ mass spectrum for reaction (VII.37). There is a hint of structure in the ω region. Its significance is low, however. The size of the structure is greatly enhanced for certain regions of momentum transfer. Figures 35(a) and (b) show the mass distribution for $|t| < 0.1$ $(\text{GeV/c})^2$ and $0.1 < |t| < 0.3$ $(\text{GeV/c})^2$, respectively. No effect is seen in the small t region $(|t| < 0.1)$. However, for $0.1 < |t| < 0.3$, a pronounced peak is observed, centered somewhat above the ω at about 790 MeV. There is also some evidence for a dip below the ω at about 775 MeV.

The observation that the interference effect has a dip below the ω and a peak above can be strengthened by making cuts on the angular distribution so

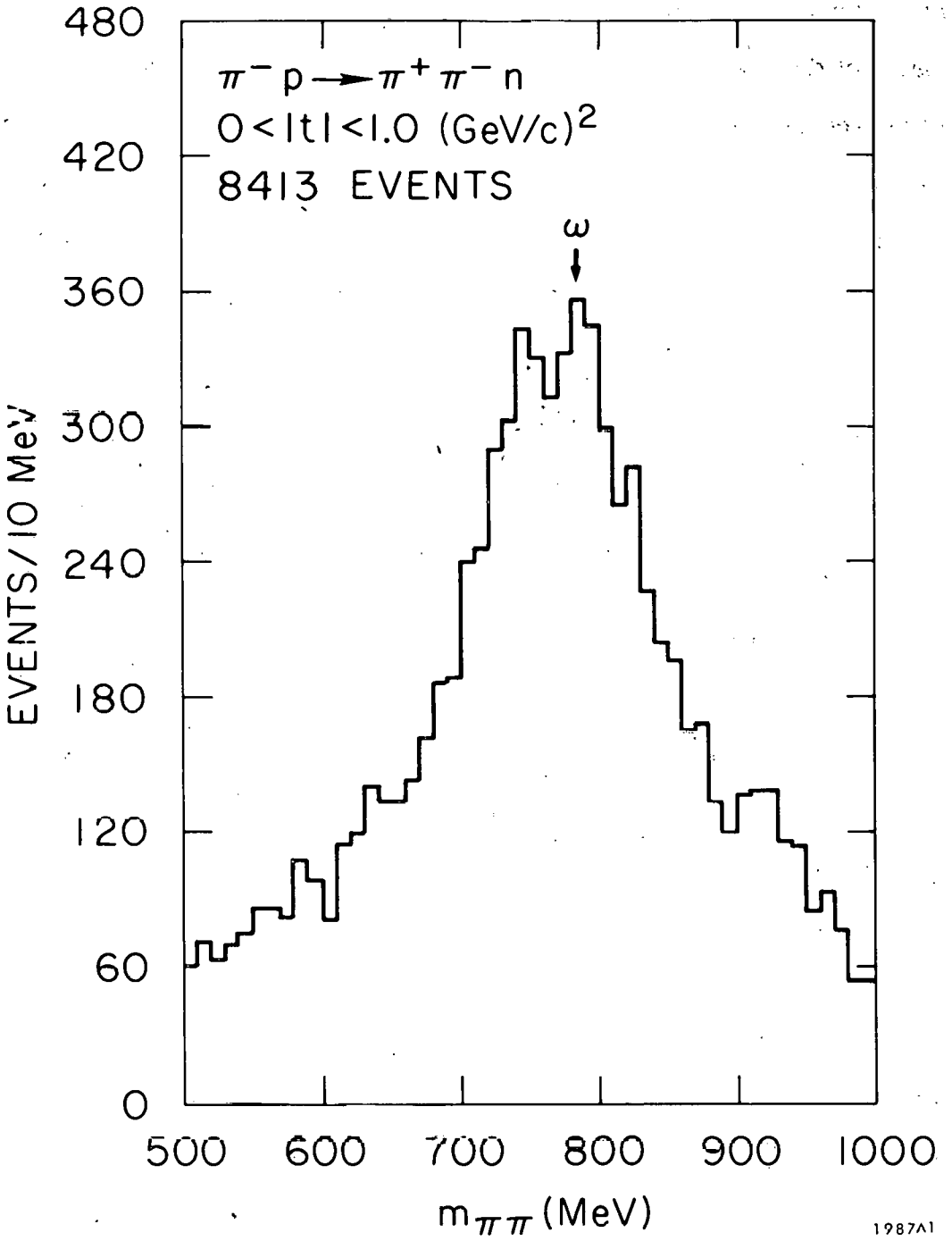

FIG. 34--Observed $\pi^+\pi^-$ mass spectrum for $0 < |t| < 1.0$ (GeV/c)^2.

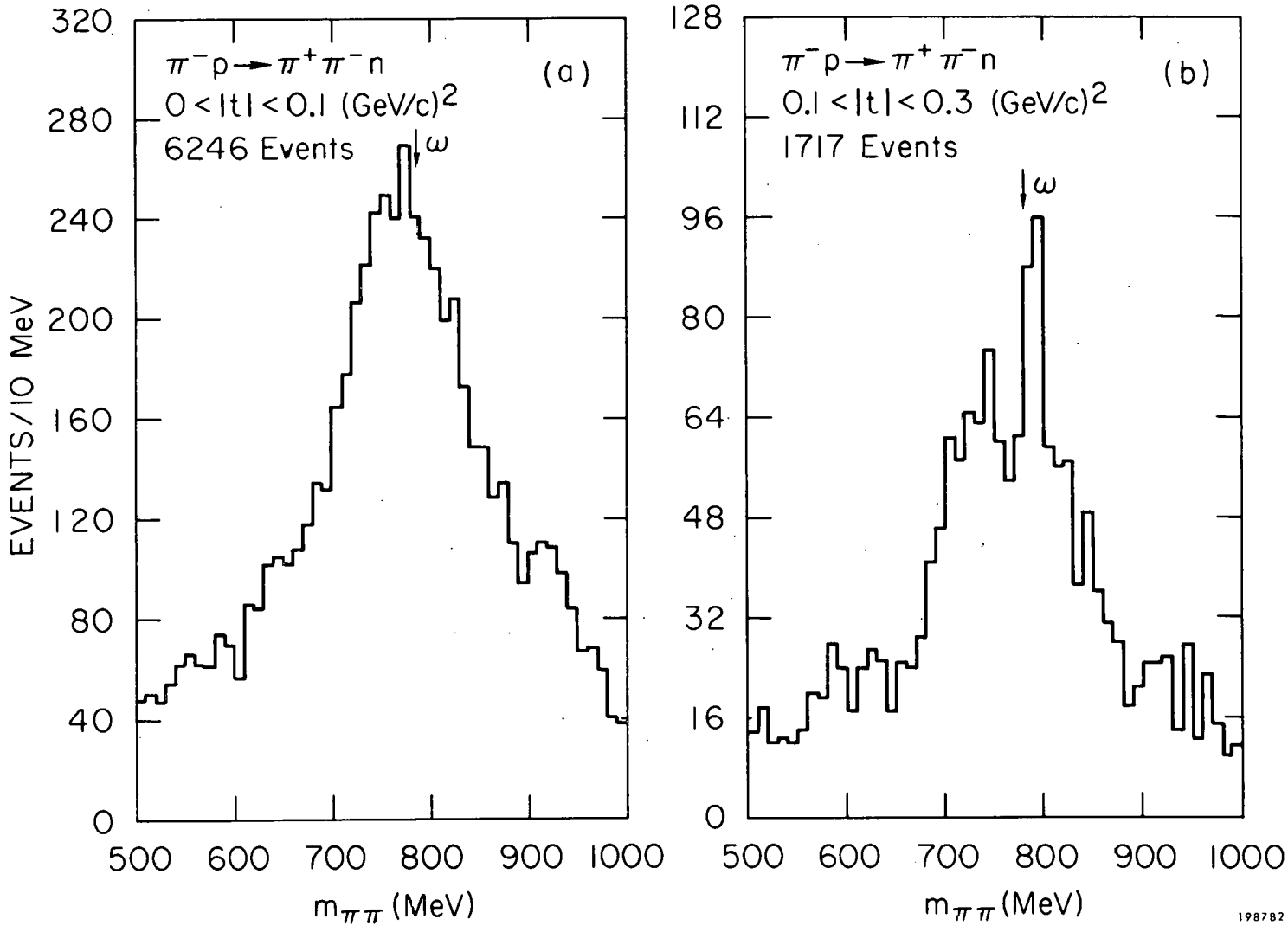

FIG. 35--Observed $\pi^+\pi^-$ mass spectrum for different regions of momentum transfer, (a) $0 < |t| < 0.1$ (GeV/c)^2, (b) $0.1 < |t| < 0.3$ (GeV/c)^2.

as to preferentially select transverse ρ^0 and ω production. Figure 36(a)shows two such cuts. The unshaded histogram shows data with $|\cos\theta^H| < 0.4$, whereas the shaded histogram is cut on $|\cos\theta^H| < 0.2$. The dip below the ω mass becomes extremely pronounced, and indeed the mass distribution looks almost like a split ρ^0 meson!* The inset shows the data for $|\cos\theta^H| < 0.4$ on a finer mass scale (5 MeV bins). The structure is well centered at the ω mass, with a dip and peak of rather equal size on either side. This is the interference shape which is expected if the phase between the amplitudes is $\sim -90^o$.

When the inverse cut is made on the helicity angle ($|\cos\theta^H| > 0.4$), both the size and shape of the interference change dramatically, as shown in Fig. 36(b). This qualitatively suggests that either the coherence or the phase angle, or both, are quite different for longitudinal, as compared to transverse, production. The most straightforward explanation of such behavior is that the ω is produced predominantly transversely as is observed in this t range at 7 GeV/c.[71]

If the $\pi^+\pi^-$ system is assumed to contain only S and P waves for $m_{\pi\pi} < 900$ MeV, we can correct the mass spectrum for the efficiency using a procedure similar to that described in Chapter V to find the density matrix elements and differential cross section as a function of t. That is, for each bin in mass we fit the observed angular distribution and find the cross section $d\sigma/dm$ for that mass bin.

*It is amusing to note that the dipole form used by the CERN spectrometer groups to describe the split A_2 meson[72] also fits the $|\cos\theta^H| < 0.2$ data from this experiment very well (χ^2/degree of freedom ≈ 1.0). When the dipole fit is compared to a fit using a simple Breit-Wigner, the χ^2 improves by approximately 20 in the region of the "split".

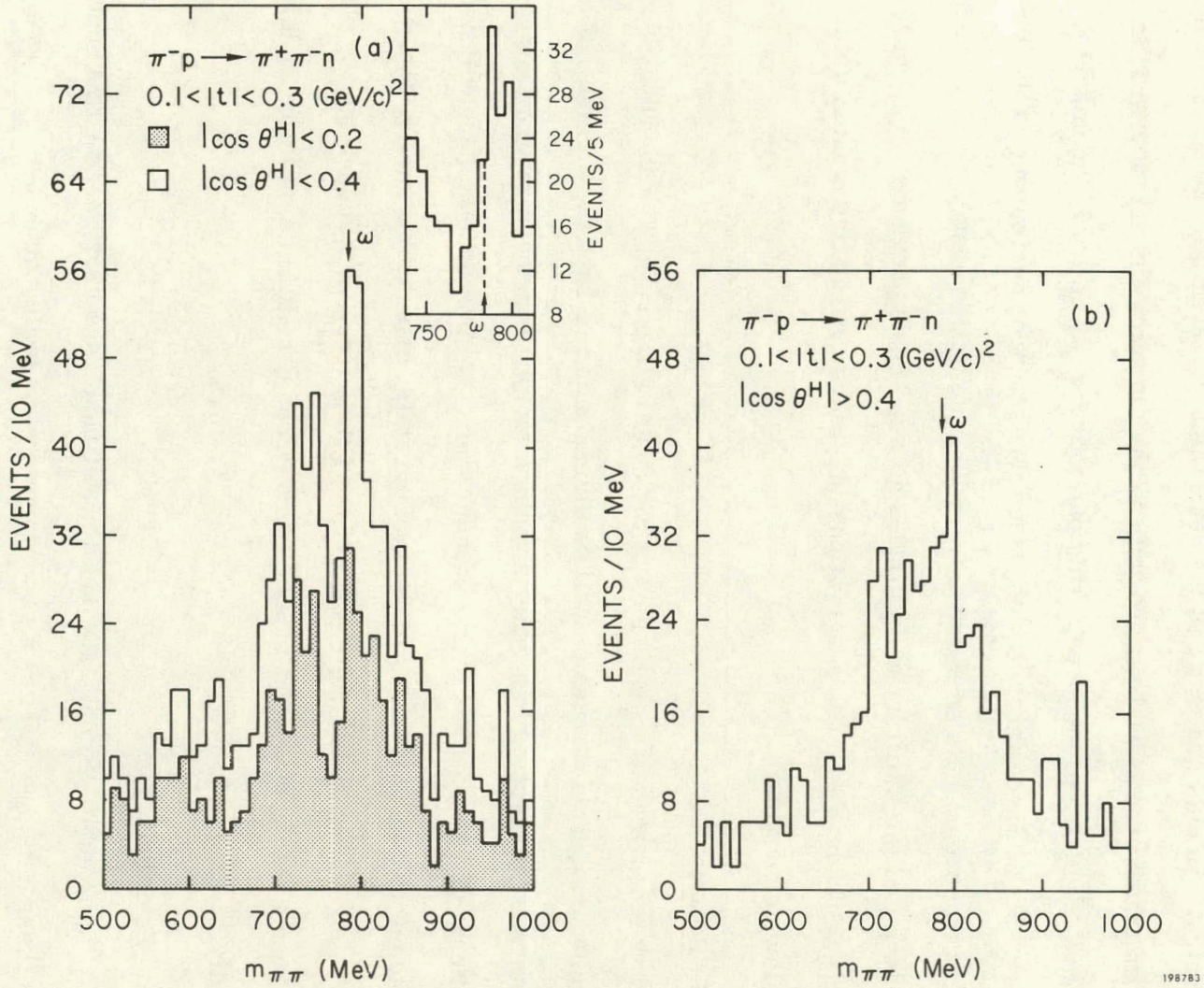

FIG. 36--Observed $\pi^+\pi^-$ mass spectrum for $0.1 < |t| < 0.3$ (GeV/c)^2: (a) The unshaded histograms contain data with $|\cos \theta^H| < 0.4$, whereas the shaded histogram includes data with $|\cos \theta^H| < 0.2$. The inset displays the $|\cos \theta^H| < 0.4$ data with smaller mass bins (5 MeV). (b) Data with $|\cos \theta^H| > 0.4$.

The resultant mass spectrum for $0.1 < |t| < 0.3$ $(GeV/c)^2$ is shown in Fig. 37. This distribution confirms the behavior which was seen above in the raw spectra. As cuts are made on the data which preferentially select more-and-more transverse ρ^o and ω production, the dip below the ω becomes progressively more pronounced. This can most easily be seen by comparing Figs. 37, 35(b) and 36(a), in order, since these figures correspond to increasingly transverse cuts on the data. Similar qualitative observations about the behavior of the interfering amplitudes as were made previously apply here. We shall return to these observations in a more quantitative fashion in the following section.

D. Results

We now turn to a discussion of the quantitative results of the fitting procedure. This discussion will be divided into two subtopics. First, the data will be analyzed in a general fashion simply to demonstrate that a significant anomaly indeed exists at the ω mass. In this analysis, we will not attempt to determine any of the experimentally important mixing parameters. Secondly, we will use the P form of the fitting function to determine the phase between the ρ and ω amplitudes, the coherence, and limits on the branching ratio.

1. Significance

In order to demonstrate that a significant ρ-ω interference effect occurs in these data, we will use a procedure similar to that discussed by Flatté.[29] Using Eq. (VII.33), a fit is made to the data with the terms representing the ω fixed at zero while the coefficients representing the ρ^o and the background are allowed to vary. This fit yields a goodness of fit parameter χ^2_ρ. Another fit is then made to the data in which the two parameters which multiply the

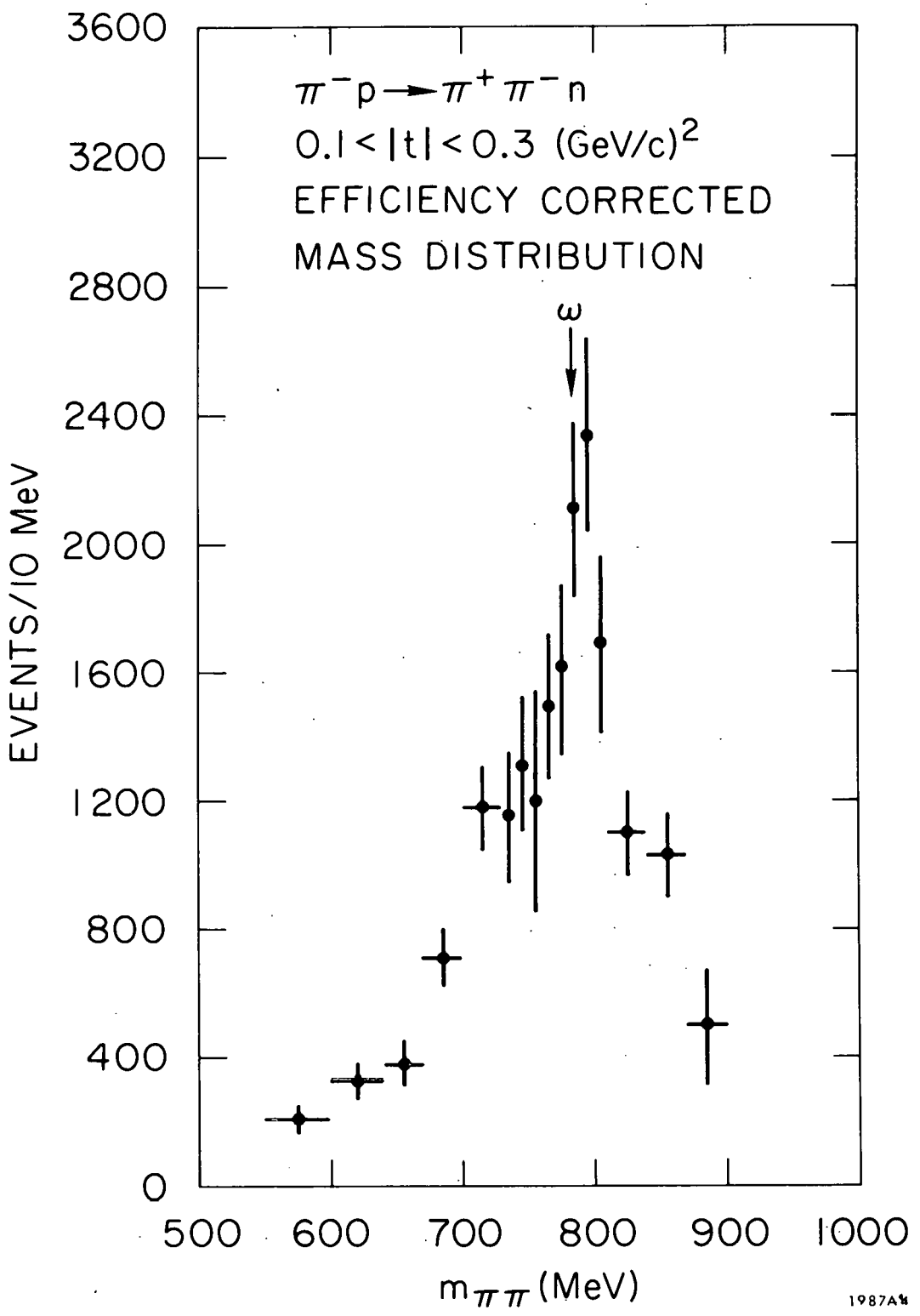

FIG. 37--Efficiency-corrected $\pi^+\pi^-$ mass spectrum for $0.1 < |t| < 0.3$ (GeV/c)^2.

ω terms are also allowed to vary. In doing this fit, the ω mass and width are fixed at their accepted values, 783.7 MeV and 11.9 MeV, respectively. This fit yields χ^2_ω for a fit with two less degrees of freedom than for the "ρ only" fit. The difference between the two parameters thus found, $\Delta\chi^2 = \chi^2_\rho - \chi^2_\omega$, is a direct measure of the significance of the ω signal in the data.

The $\Delta\chi^2$ formed above has approximately a χ^2 distribution for two degrees of freedom. We can thus utilize it to calculate the number of standard deviations that the ω signal lies away from zero, using standard tabulated chi-square probability distributions.

The results of this analysis are shown in Table IV for the t region in which the largest qualitative effect is observed $[0.1 < |t| < 0.3\ (\mathrm{GeV/c})^2]$. The mass spectrum is fit from 530 - 870 MeV. The data are analyzed both with and without resolution folded into the fit in order to demonstrate that the significance of the effect does not depend greatly on the resolution. We see that the ω signal is $\sim 5\sigma$ from zero in this data sample. However, we also note that the ρ mass and width change substantially when the ω effect is added. Experimentally, several of the parameters are strongly correlated in the fit so that the available data cannot determine them well.

In order to have more stable parameters and demonstrate that the significance of the effect is not largely due to a shift in the ρ^0 parameters, we have used the following procedure.

We fit the mass distribution, ignoring the ω region, for $|t| < 0.3\ (\mathrm{GeV/c})^2$ to both the F and P forms with the terms representing the ω set equal to zero. The values obtained using the P form are $m_\rho = 764 \pm 3$ MeV and $\Gamma_\rho = 157 \pm 8$ MeV, whereas for the F form, we find that $m_\rho = 781 \pm 7$ MeV and $\Gamma_\rho = 167 \pm 10$ MeV.

TABLE IV

Fits to $\pi^- p \rightarrow \pi^+ \pi^- n$ Mass Distribution with the ρ^0 Mass and Width Allowed to Vary.

Reference Number	Form	Momentum Transfer $(GeV/c)^2$	Resolution (MeV)	ω Included in Fit	M_ρ(GeV)	Γ_ρ(GeV)	χ^2/ν	$\Delta\chi^2$	Significance of ω Signal
1	F	$0.1 < \|t\| < 0.3$	0	NO	0.786 ± 0.006	0.177 ± 0.017	86.1/62	--	--
2	F	$0.1 < \|t\| < 0.3$	0	YES	0.763 ± 0.020	0.147 ± 0.016	57.9/60	28.2	4.9σ
3	F	$0.1 < \|t\| < 0.3$	8	NO	0.782 ± 0.005	0.167 ± 0.015	86.8/62	--	--
4	F	$0.1 < \|t\| < 0.3$	8	YES	0.747 ± 0.020	0.142 ± 0.019	57.0/60	29.8	5.0σ

We note that these values are well within the range seen in most ρ^0 experiments. We emphasize, however, that these numbers are dependent on the forms which were chosen for the ρ^0 and the background. The use of different forms can shift the mass and width values by ~ 15 - 20 MeV even though the quality of fit is essentially unchanged. As was noted previously, such shifts have little effect on the determination of the interference parameters and will be ignored in the following analysis.

Using these values for m_ρ and Γ_ρ, we have carried out the analysis described above for 3 different t regions. The results are shown in Table V. For comparison purposes in the region $0.1 < |t| < 0.3\,(\mathrm{GeV/c})^2$. We also show in the same table similar results using the P form with the coherency parameter set equal to one. A representative sample of these fits to the data is shown in Fig. 38. We note that the fits to the data for $|t| < 0.1\,(\mathrm{GeV/c})^2$ are excellent and that there is no evidence for an ω in this range of t. On the other hand, a 4.2 - 4.6 σ effect exists for $0.1 < |t| < 0.3\,(\mathrm{GeV/c})^2$. Comparison with Table IV shows that the measured significance of the ω anomaly has been lowered slightly by fixing the ρ mass and width but that a large effect still remains. We can also infer from Table V that the measured significance of the ω anomaly varies little with radically different assumptions as to the form of the background or the ρ^0 mass and width.

It is clear from the raw mass spectra that the ρ-ω interference effect exists largely for transverse vector meson production. In Table VI, we show fits to different regions in $\cos\theta^H$ which confirm this impression. Fits 13-16 show that a large effect (4.4 σ) indeed exists for $|\cos\theta^H| \leq 0.4$ whereas there is no significant effect for $|\cos\theta^H| > 0.4$. We see this same effect in another way by fitting the efficiency-corrected mass spectrum as

TABLE V

Fits to $\pi^- p \rightarrow \pi^+ \pi^- n$ Mass Distribution with the ρ^0 Mass and Width Fixed.

Reference Number	Form	Momentum Transfer (GeV/c^2)	Resolution (MeV)	ω Included in Fit	M_ρ(GeV)	Γ_ρ(GeV)	χ^2/ν	$\Delta\chi^2$	Significance of ω Signal
5	F	$0.0 < \|t\| < 0.02$	8.0	NO	0.781 (fixed)	0.167 (fixed)	54.5/65	--	
6	F	$0.0 < \|t\| < 0.02$	8.0	YES	0.781 (fixed)	0.167 (fixed)	53.6/63	0.9	$< 1\ \sigma$
7	F	$0.02 < \|t\| < 0.1$	8.0	NO	0.781 (fixed)	0.167 (fixed)	59.5/65	--	
8	F	$0.02 < \|t\| < 0.1$	8.0	YES	0.781 (fixed)	0.167 (fixed)	59.1/63	0.4	$< 1\ \sigma$
9	F	$0.1 < \|t\| < 0.3$	8.0	NO	0.781 (fixed)	0.167 (fixed)	86.3/65	--	
10	F	$0.1 < \|t\| < 0.3$	8.0	YES	0.781 (fixed)	0.167 (fixed)	65.4/63	20.9	$4.2\ \sigma$
11	P	$0.1 < \|t\| < 0.3$	8.0	NO	0.764 (fixed)	0.157 (fixed)	88.7/65	--	
12	P	$0.1 < \|t\| < 0.3$	8.0	YES	0.764 (fixed)	0.157 (fixed)	63.3/63	25.4	$4.6\ \sigma$

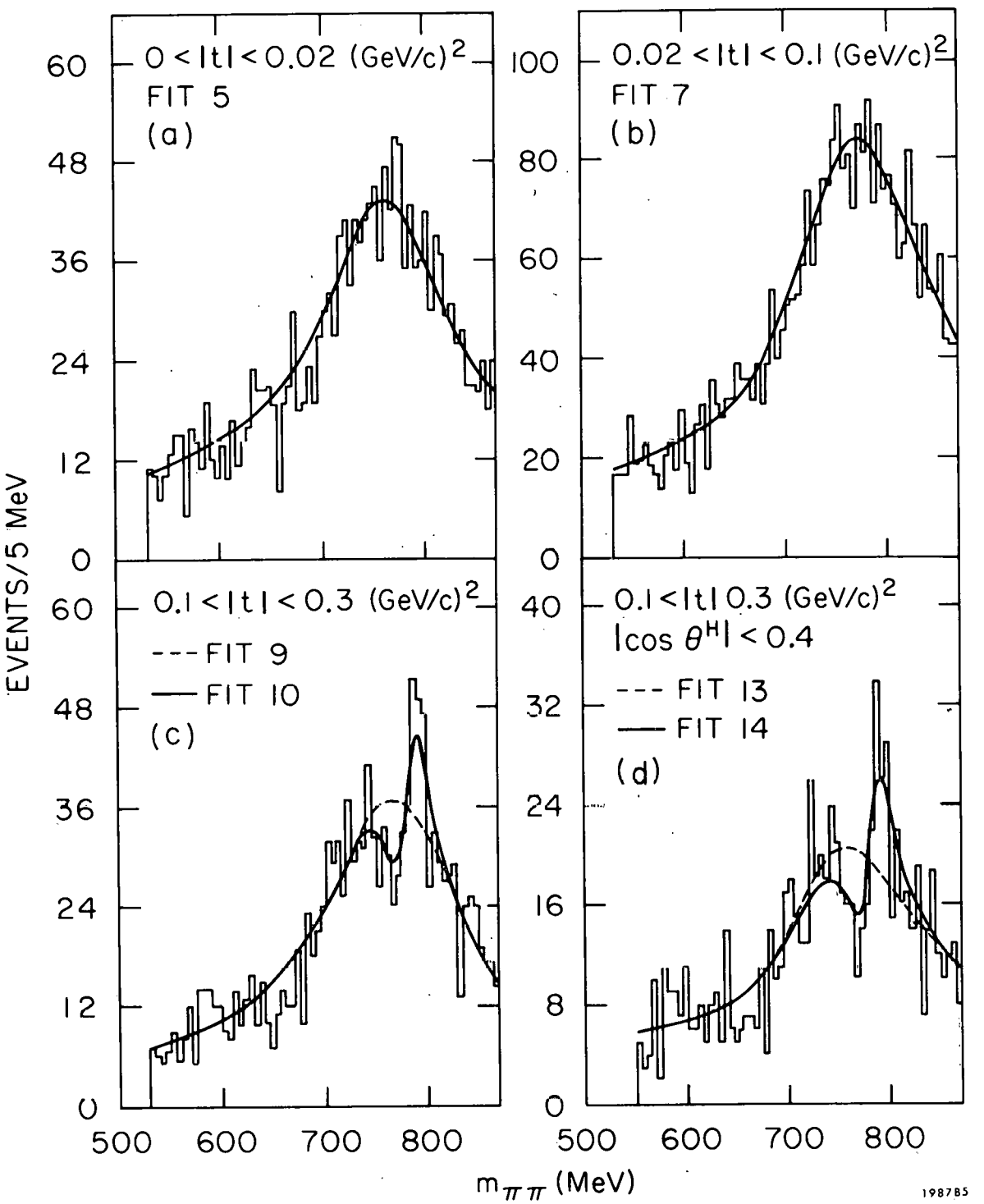

FIG. 38--Observed $\pi^+\pi^-$ mass spectra for several regions of momentum transfer and decay angle. The lines represent fits to the data described in the text, (a) $0 < |t| < 0.02$ (GeV/c)^2, (b) $0.02 < |t| < 0.1$ (GeV/c)^2, (c) $0.1 < |t| < 0.3$ (GeV/c)^2, (d) $0.1 < |t| < 0.3$ (GeV/c)^2 with $|\cos \theta^H| < 0.4$.

TABLE VI

Fits to $\pi^- p \rightarrow \pi^+ \pi^- n$ Mass Distribution for Cut ($|\cos \theta^H| < 0.4$) and Efficiency Corrected Angular Ranges.

$0.1 < \|t\| < 0.3 (\text{GeV/c})^2$; P form is used with $M_\rho = 0.764$ and $\Gamma_\rho = 0.157$ GeV; Resolution = 8 MeV					
Reference Number	Angular Range	ω Included in Fit	χ^2/ν	$\Delta\chi^2$	Significance of ω Signal
13	$\|\cos\theta^H\|<0.4$	NO	89.8/62	--	
14	$\|\cos\theta^H\|<0.4$	YES	66.2/60	23.6	4.4 σ
15	$\|\cos\theta^H\|>0.4$	NO	51.4/62	--	
16	$\|\cos\theta^H\|>0.4$	YES	49.0/60	2.4	1.0 σ
17	Corrected	NO	25.7/12	--	
18	Corrected	YES	13.0/10	12.7	3.1 σ

shown in fits 17-18. A 3.1 σ effect is observed. In general, one would expect the measured significance of the effect to be lower for the corrected distribution than for the raw data distribution if the interference effect changes with cos θ^H.

2. Interference Parameters

It is clear from the preceding section that there is a significant ρ-ω interference effect only for $0.1 < |t| < 0.3\,(\mathrm{GeV/c})^2$, so it is this t region with which we are here concerned. As mentioned previously, the experiment of Hagopian et al.[32] in this reaction at 2.3 GeV/c is unable to determine the coherence parameter since a peak is seen at the ω mass. However, in the present experiment, a dip-peak structure is seen which enables lower limits to be placed on the coherence and allows the phase to be determined without assuming any value for the coherence.

In general, the best fit is found when C=1. However, for all fits there is a rather large region of C space lying below one for which there is little change in χ^2. The errors on C are therefore quite non-gaussian. In addition, the values of C and Φ are correlated in the fits. In order to display this most effectively, we will show $\Delta\chi^2$ plots in (C,Φ) space where we define $\Delta\chi^2$ to be the change in χ^2 from the best fit value.

Figure 39(a) shows a contour plot from a fit to the entire data sample with $0.1 < |t| < 0.3\,(\mathrm{GeV/c})^2$. The nonlinearity of the error on C is obvious. The correlation between the values of C and Φ should also be noted. For comparison purposes, it is convenient to quote a value for Φ with one-standard-deviation errors and we will do so below. The nonlinear character of the errors should be remembered, however, and in particular, it should be noted that the "2σ" errors are less than twice the "1σ" errors.

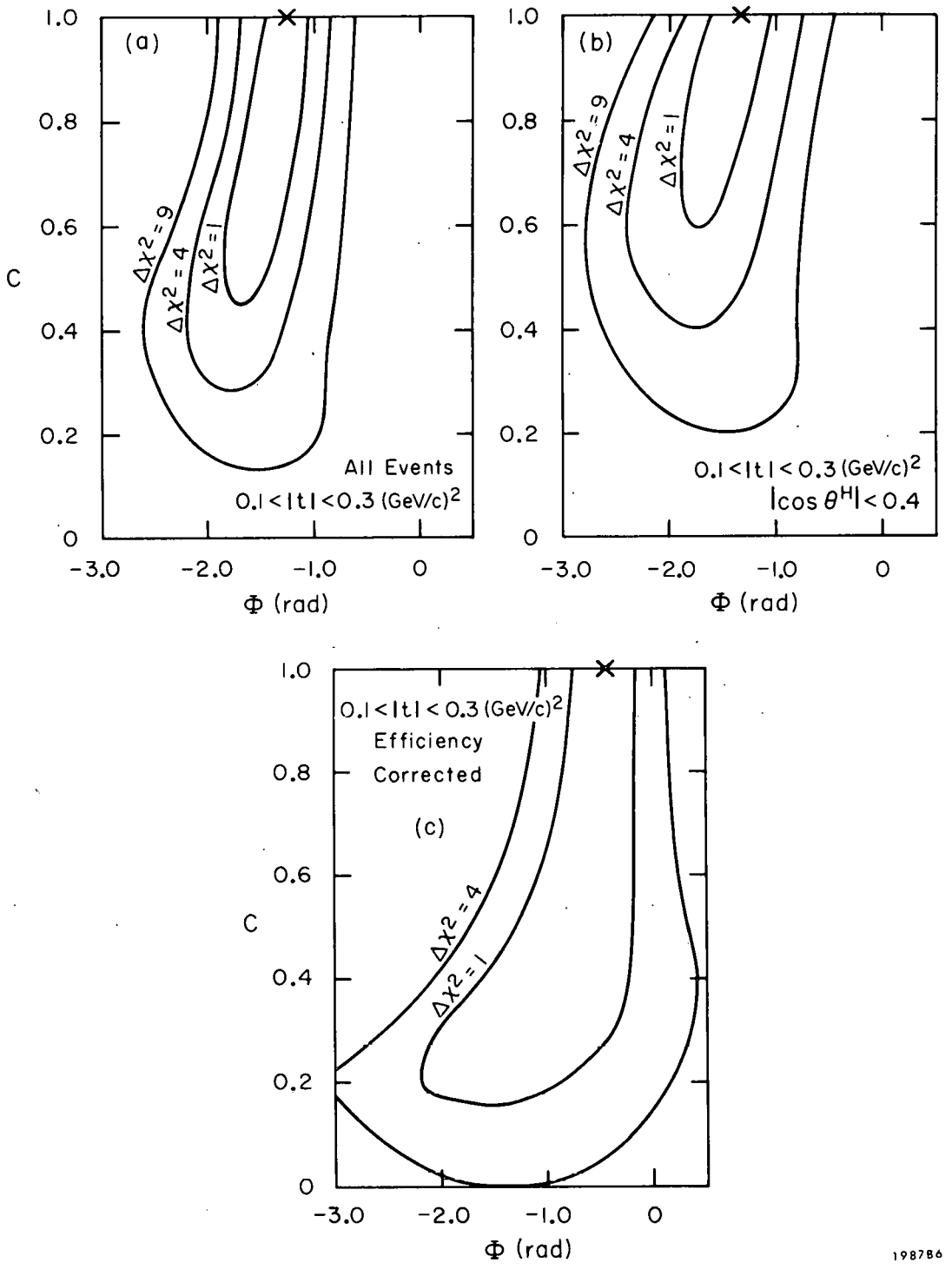

FIG. 39--χ^2 contours in (C, Φ) space for the ρ-ω fits described in the text, (a) $0.1 < |t| < 0.3$ (GeV/c)^2, (b) $0.1 < |t| < 0.3$ (GeV/c)^2 with $|\cos\theta^H| < 0.4$, (c) $0.1 < |t| < 0.3$ (GeV/c)^2 and efficiency corrected.

The $\Delta\chi^2$ contours of Fig. 39(a) do not include any contribution for the uncertainty in the knowledge of the mass scale (~ 2.0 MeV) or resolution (~ 1 MeV). The contribution of these errors has been studied extensively and has been shown to be small. The net effect of these uncertainties is a small increase in the errors which we included below.

For the entire raw data sample with $0.1 < |t| < 0.3$ $(\text{GeV}/c)^2$, we find from Fig. 39(a) that

$$C > 0.30 \quad (95\% \text{ CL})$$

and

$$\Phi = -1.40 \pm 0.45 \quad (\text{rad}) \quad .$$

It was noted previously that if we cut the data so as to preferentially select transverse vector mesons ($|\cos \theta^H| < 0.4$), the dip below the ω becomes much more pronounced. We therefore expect to derive a large value for C from these data since incoherent amplitudes cannot produce any dip structure. The $\Delta\chi^2$ contour plot for the fit to this region is shown in Fig. 39(b). It is clear that C is significantly larger here than for the entire data sample. With the same qualifications concerning errors that were stated above, we find that

$$C > 0.41 \quad (95\% \text{ CL})$$

$$\Phi = -1.45 \pm 0.45 \quad .$$

We note that the phase $\simeq -\pi/2$ seen in the above data sample, when transverse production is preferentially included, differs both from the prediction of Goldhaber, Fox, and Quigg,[64] and the lower energy data of Hagopian et al.[32] by $\simeq -\pi/2$. This result is not surprising, since the B-exchange contribution, which was the basis of the theoretical argument and which has been invoked to

explain the unnatural-parity-exchange contribution to low-energy ω production, would be expected to become less important at higher energies.

It has been previously observed that the raw data suggest that the ω is produced more transversely than the ρ^0 in our data. The change in coherency which is observed above, as different fractions of the angular distribution are accepted, is also consistent with transverse ω production. Completely transverse ω production is expected in a simple exchange model since natural-parity-exchange (ρ) would be expected to dominate ω production at large energies. It is clear from the data of Matthews et al.[71] that some unnatural parity exchange* (e.g., B) must still be present at 7 GeV/c, since $\rho_{00} \neq 0$. On the other hand, the ω is already quite transverse at 7 GeV $\left[\rho_{11}^H \sim 0.39 \right.$ for $\left. 0.1 < |t| < 0.3 \text{ (GeV/c)}^2\right]$ and is more transverse than our ρ^0 is in this region.

We thus infer that the data in this experiment is large dominated by transverse ω production so that we are insensitive to any longitudinal production contribution. The phase determined above thus suggests that the phase between the transverse amplitudes themselves is $\approx -\pi/2$.

Because the $\pi^+\pi^-$n experiment of Hagopian et al.[32] observes a peak structure, it is of interest to fit the efficiency-corrected mass distribution since we also see a peak structure here and since this is the distribution which is observed in a 4π detector such as a bubble chamber. From Fig. 39(c), we see that, as expected, the value of C is not well determined. In addition, Φ is well determined only if C is large. If we assume, for example, that

*Since natural parity exchange cannot contribute for decays in the production plane, it is possible to partially isolate the natural- and unnatural-parity-exchange contributions in the present data by making cuts on ϕ. The rapidly varying acceptance with ϕ in this t range makes quantitative observations difficult. It is clear qualitatively, however, that the ρ-ω interference effect has a weak dependence on ϕ which suggests that both natural- and unnatural-parity exchange contribute.

$C \geq 0.6$ (Hagopian et al. assumed $C \geq 0.4$) then $\Phi = -0.60 \pm 0.45$ (rad) in good agreement with the value $\Phi = -0.26 \pm 0.52$ (rad) from the lower energy experiment!

Another interesting aspect of the above fits is that they provide information on the branching ratio

$$\text{B.R.} = \frac{\Gamma(\omega \rightarrow 2\pi)}{\Gamma(\omega \rightarrow 3\pi)} \quad . \tag{VII.38}$$

In order to calculate this number, we must know the cross section $d\sigma(\omega)/dt$ for the reaction $\pi^- p \rightarrow \omega^0 n$ at 15 GeV/c. Little information exists on this reaction. However, several experiments have studied the charge conjugate reaction $\pi^+ n \rightarrow \omega^0 p$ at lower energies. The highest energy (published[71]) data are at 7 GeV/c, so that we must extrapolate the cross sections to 15 GeV/c. The energy dependence of the cross section from 2 to 7 GeV is well represented by a slope of $1/p^{2.25}$ which implies an extrapolation factor of 1/5.6. In addition, we assume that the t dependence at 15 GeV/c is identical with that at 7 GeV/c. This yields a cross section in our t interval at 15 GeV/c of $\sigma(\omega \rightarrow 3\pi) = 9.0 \pm 2.8$ μb where we have included an estimate of 25% error for the extrapolation.

The exact value of B.R. cannot be determined without knowledge of the coherency parameter which is rather poorly determined for large values of C. However, the lower limit of B.R. can be derived by assuming C=1. We first consider the corrected mass distribution for which case $\alpha_\omega = 315 \pm 81$. Then

$$\sigma(\omega \rightarrow 2\pi) = N \int q \cdot |a_\omega|^2 \cdot |M_\omega|^2 \cdot dm$$

where N gives the number of μb represented by one event and has the value $N = 0.00034 \pm 0.000023$ μb/event (see Chapter IV.B). So the lower limit on

B. R. from the corrected mass distribution is

$$\text{B.R.} \geq 2.4 \, ^{+2.0}_{-1.2} \, \%$$

where we have included estimates of the possible systematic effects. We observe that, as above, the errors are quite nonlinear. In particular the 95% confidence level is given by

$$\text{B.R.} > 0.7\% \quad (95\% \text{ CL}) \quad .$$

Since the ω effect is so much more significant in the mass distribution with the cut $|\cos \theta^{H}| < 0.4$, it is of interest to derive the branching ratio from it. It is necessary for this purpose to know the angular distribution of the ω decay.

We have noted previously that ρ_{11}^{ω} might be expected to be larger than 0.39 at this energy. If we wish to calculate a lower limit, we make the most conservative assumption for that purpose, which is to assume that ρ_{11}^{ω} $\left[0.1 < |t| < 0.3 \text{ (GeV/c)}^2\right] = 0.5$. This yields

$$\text{B.R.} \geq 2.1 \, ^{+1.6}_{-0.9} \, \% \qquad \text{with} \qquad \text{B.R.} > 0.7\% \quad (95\% \text{ CL}) \, ,$$

in excellent agreement with the value of B.R. from the corrected distribution.

In order to show the importance of the assumption that $\rho_{11}^{\omega} = 0.5$, we note that if $\rho_{11}^{\omega} = 0.39$, as given by the 7-GeV/c Toronto[71] data, then $\text{B.R.} \geq 2.6 \, ^{+2.0}_{-1.1} \, \%$.

Finally, using the total data sample we find that

$$\text{B.R.} \geq 1.8 \, ^{+0.9}_{-0.8} \, \% \qquad \text{with} \qquad \text{B.R.} > 0.7\% \quad (95\% \text{ CL})$$

which agrees very well with the above determinations.

We can also calculate a significant upper limit on the branching ratio from our data. The central value of the upper limits are identical with the lower

limits noted previously since C=1 is the best fit value for all the distributions. The errors are quite large, however, and we find from the total data sample that

$$\text{B.R.} < 4.9\% \ (84\% \text{ CL}) \qquad \text{with} \qquad \text{B.R.} < 6.0\% \ (95\% \text{ CL}) \ .$$

We note that the above branching ratios are quite similar to those derived from most other experiments. For example, Hagopian et al.[32] obtain as a lower limit B.R. $\geq 0.36 \pm 0.1\%$ and as an upper limit B.R. $\leq 3.2 \pm 0.8\%$, while the Orsay storage ring[52] obtained the value B.R. $= 4.0 \, ^{+2.3}_{-1.8}\%$. The experiments with the smallest quoted errors on B.R. are the photoproduction experiments off nuclei. Their analyses are, however, somewhat more model dependent than the foregoing. A complete photoproduction experiment using three different nuclei in order to check the contribution of the nuclear physics was recently carried out by Alvensleben et al.[73] who obtained B.R. $= 1.22 \pm 0.3\%$.

Conclusion

We have observed a significant ($> 1\sigma$) ρ-ω interference effect for $0.1 < |t| < 0.3 \, (\text{GeV/c})^2$ in the reaction $\pi^- p \to \pi^+ \pi^- n$ at 15 GeV/c. The overall phase between the amplitudes in the observed data is dominated by the transverse production amplitudes and is shown to be $\approx -1.40 \pm 0.45$ (rad). This phase differs by $\approx -\pi/2$ from both the prediction of Goldhaber, Fox and Quigg, and the previous experiment of Hagopian et al. in the same reaction at 2.3 GeV/c. The coherency was determined to be > 0.30 (95% CL) for the entire data sample and > 0.41 (95% CL) for the transverse region ($|\cos \theta^H| < 0.4$), while C is not well determined for the corrected mass spectrum. The lower limit on the branching ratio was shown to be B.R. $> 0.7\%$ (95% CL).

REFERENCES

1. A. R. Erwin et al., Phys. Rev. Letters 6, 628 (1961).
2. M. Alston et al., Phys. Rev. Letters 6, 300 (1961); B. C. Maglic et al., Phys. Rev. Letters 7, 178 (1961); P. Schlein et al., Phys. Rev. Letters 10, 368 (1963); P. L. Connolly et al., Phys. Rev. Letters 10, 371 (1963).
3. Y. Nambu, Phys. Rev. 106, 1366 (1957).
4. W. R. Frazer and J. R. Fulco, Phys. Rev. Letters 2, 365 (1959).
5. J. J. Sakurai, Ann. Phys. (N.Y.) 11, 1 (1960) and in Selected Topics on Elementary Particle Physics, Proceedings of the International School of Physics, "Enrico Fermi," Course XXVI, edited by M. Conversi (Academic Press, New York, 1963), p. 41.
6. A. Salam and J. C. Ward, Nuovo Cimento 20, 419 (1961).
7. M. Gell-Mann, Phys. Rev. 125, 1067 (1962).
8. Y. Ne'eman, Nucl. Phys. 26, 222 (1961).
9. M. Gell-Mann and F. Zachariasen, Phys. Rev. 124, 953 (1961).
10. N. M. Kroll, T. D. Lee, and B. Zumino, Phys. Rev. 157, 1376 (1967) and references listed therein.
11. D. S. Beder, Phys. Rev. 149, 1203 (1966); H. Joos, Acta Phys. Austr., Suppl. IV (1967); C. Iso and H. Yoshii, Ann. Phys. (N. Y.) 47, 424 (1968); M. Krammer and D. Schildknecht, Nucl. Phys. B7, 583 (1968).
12. D. H. Coward et al., Phys. Rev. Letters 20, 292 (1968).
13. H. Joos, Proceedings of the Heidelberg International Conference on Elementary Particles, 1967, edited by H. Filthuth (North-Holland Publishing Co., 1968), p. 349.

14. M. Roos and L. Stodolsky, Phys. Rev. 144, 1172 (1966); M. Gourdin, Springer Tracts in Modern Physics, Vol. 55, edited by G. Hohler (Springer-Verlag, New York, 1970), p. 191.

15. A. M. Boyarski et al., Phys. Rev. Letters 20, 300 (1968); A. M. Boyarski et al., Phys. Rev. Letters 21, 1767 (1968); and private communication.

16. P. Heide et al., Phys. Rev. Letters 21, 248 (1968).

17. H. Burfeindt et al., Phys. Letters 33B, 509 (1970); C. Geweniger et al., Phys. Letters 29B, 41 (1969); H. Burfeindt et al., preprint submitted to the 1969 International Symposium on Electron and Photon Interactions at High Energies, Daresbury, England (Abstract 86).

18. For example, R. Diebold, Proceedings of the High Energy Physics Conference, Boulder, Colorado, 1969, edited by K. T. Mahanthappa et al. (Colorado Associated University Press, Boulder, 1970), p. 3. (This was also issued as SLAC-PUB-673.) F. J. Gilman, invited talk given at the Conference on Particle Interactions at High Energies, University of Toronto, March 28-29, 1969 (also SLAC-PUB-589).

19. A. Dar et al., Phys. Rev. Letters 20, 1261 (1968).

20. R. Diebold and J. A. Poirier, Phys. Rev. Letters 20, 1532 (1968).

21. I. Derado and Z.G.T. Guiragossian, Phys. Rev. Letters 21, 1556 (1968).

22. R. Diebold and J. A. Poirier, Phys. Rev. Letters 22, 255 (1969).

23. R. Diebold and J. A. Poirier, Phys. Rev. Letters 22, 906 (1969).

24. D. Schildknecht, DESY Report No. 69/10 (1969).

25. G. F. Chew and F. E. Low, Phys. Rev. 113, 1640 (1959).

26. For example, J. P. Baton et al., Phys. Letters 25B, 419 (1967).

27. G. L. Kane and M. Ross, Phys. Rev. 177, 2353 (1969); P. K. Williams, Phys. Rev. D1, 1312 (1970).

28. S. L. Glashow, Phys. Rev. Letters 7, 469 (1961).

29. S. M. Flatté et al., Phys. Rev. 145, 1050 (1966); S. M. Flatté, Phys. Rev. D1, 1 (1970).

30. For example, G. Goldhaber, talk given at the International Conference on Experimental Meson Spectroscopy, Philadelphia, Pennsylvania, 1970, see Experimental Meson Spectroscopy, edited by C. Baltay and A. H. Rosenfeld (Columbia University Press, New York, 1970), p. 59.

31. G. Goldhaber et al., Phys. Rev. Letters 23, 1351 (1969).

32. S. Hagopian et al., Phys. Rev. Letters 25, 1050 (1970).

33. M. Gan, F. Bulos, and H. L. Lynch, Report No. SLAC-TN-71-20; F. Bulos and H. L. Lynch, SLAC Group C Internal Report.

34. A. Kilert et al., discussed in the Proceedings of the International Conference on Instrumentation for High Energy Physics, Dubna, USSR, September 1970, edited by V. P. Dzhelepov et al. (Joint Institute for Nuclear Research, USSR, 1971), p. 453 (also issued as SLAC-PUB-828); H. H. Williams, Stanford University Doctoral Dissertation in Physics (1972), to be issued as Report No. SLAC-142.

35. Particle Data Group: N. Barash-Schmidt et al., Rev. Mod. Phys. 43, S1 (1971).

36. K. J. Foley et al., Phys. Rev. 181, 1775 (1969); K. J. Foley et al., Phys. Rev. Letters 11, 425 (1963); Phys. Rev. Letters 19, 330 (1967).

37. J. Ballam et al., Report No. SLAC-PUB-900 (1971), submitted to Phys. Rev.; C. Caso et al., Nuovo Cimento 47A, 675 (1967); S. J. Barish et al., Phys. Rev. 184, 1375 (1969); R. Honecker et al., Nucl. Phys. B13, 571 (1969).

38. See, for example, K. Gottfried and J. D. Jackson, Nuovo Cimento 33, 309 (1964); P. Csonka and L. Gutay, Report No. UCRL 50101 (1966); S. Gasiorowicz, Elementary Particle Physics (John Wiley and Sons, Inc., New York, 1966); L. Montanet, CERN 67-23 (1967).

39. F. James and M. Roos, MINUIT: A program to minimize a general function of n variables and calculate the true errors, CERN Computer Library, D506 (1967).

40. E. I. Shibata et al., Phys. Rev. Letters 25, 1227 (1970).

41. P. Sonderegger and P. Bonamy, preprint submitted to the Fifth International Conference on Elementary Particles, Lund, Sweden, 25 June - 1 July 1969 (Abstract 372).

42. K. Gottfried and J. D. Jackson, Nuovo Cimento 34, 735 (1964); F. Henyey et al., Phys. Rev. 182, 1579 (1969).

43. P. Baillon et al., Phys. Letters 35B, 453 (1971); H. H. Williams, Stanford University Doctoral Dissertation in Physics (1972), to be issued as Report No. SLAC-142.

44. J. Pisut and M. Roos, Nucl. Phys. B6, 325 (1968).

45. J. D. Jackson, Nuovo Cimento 34, 1644 (1964).

46. N. N. Biswas et al., Phys. Rev. D1, 2705 (1970).

47. Most of these results have been presented by F. Bulos et al., Phys. Rev. Letters 26, 1457 (1971).

48. E. Lohrmann, Proceedings of the Fifth International Conference on Elementary Particles, Lund, Sweden, 25 June - 1 July 1969, edited by G. von Dardel (Berlingska Boktryckeriet, Lund, 1969), p. 11.

49. J. E. Augustin et al., Phys. Letters 28B, 503 (1969).

50. J. F. Allard et al., Nuovo Cimento 50A, 106 (1967). Data from the charge conjugate reaction $\pi^+ n \rightarrow \omega p$ at 7.0 GeV/c indicates (see Ref. 71) that the ratio may be even smaller for very small t ($-t < m_\pi^2$).

51. For discussions of many of these experiments and the values they derive for $\gamma_\rho^2/4\pi$, see J. J. Sakurai, Phys. Rev. Letters 17, 1021 (1966); S.C.C. Ting, Proceedings of the 14th International Conference on High Energy Physics, Vienna, 1968, edited by J. Prentki and J. Steinberger (CERN, Geneva, 1968), p. 43; D.W.G.S. Leith, Lectures at the Scottish Universities Summer School in Physics, July-August, 1970 (to be published).

52. J. Lefrançois, reported at the 1971 International Symposium on Electron and Photon Interactions at High Energies, Cornell. (Proceedings are not yet published.)

53. P. Stichel, Z. Phys. 180, 170 (1964); G. Cohen-Tannoudji, and Ph. Salin, Nuovo Cimento 55A, 412 (1968); J. P. Ader et al., Nuovo Cimento 56A, 952 (1968).

54. H. Fraas and D. Schildknecht, Nucl. Phys. B6, 395 (1968).

55. A. Bialas and K. Zalewski, Phys. Letters 28B, 436 (1969).

56. C. F. Cho and J. J. Sakurai, Phys. Letters 30B, 119 (1969); A. Dar, Nucl. Phys. B19, 259 (1970).

57. M. Le Bellac and G. Plaut, Nuovo Cimento 64A, 95 (1969).

58. R. F. Schwitters et al., Phys. Rev. Letters 27, 120 (1971).

59. C. F. Cho and J. J. Sakurai, Phys. Rev. D2, 517 (1970) and private communication.

60. J. S. Ball, Phys. Rev. 124, 2014 (1961).

61. J. D. Jackson and C. Quigg, Phys. Letters 29B, 236 (1969).

62. J. Bernstein and G. Feinberg, Nuovo Cimento 25, 1343 (1962).

63. J. Harte and R. G. Sachs, Phys. Rev. 135B, 459 (1964); J. Yellin, Phys. Rev. 147, 1080 (1966); M. Gourdin, L. Stodolsky and F. M. Renard, Phys. Letters 30B, 347 (1969); D. Horn, Phys. Rev. D1, 1421 (1970); R. G. Sachs and J. F. Willemsen, Phys. Rev. D2, 133 (1970).

64. A. S. Goldhaber, G. C. Fox, and C. Quigg, Phys. Letters 30B, 249 (1969).

65. T. D. Lee, R. Oehme, C. N. Yang, Phys. Rev. 106, 340 (1957).

66. R. Marshall, invited talk at the International Conference on Meson Resonances and Related Electromagnetic Phenomena, Bologna, April 14-16, 1971, and Daresbury Report No. DNPL/P73.

67. R. Gatto, Nuovo Cimento 28, 658 (1963).

68. S. Coleman and S. L. Glashow, Phys. Rev. 134B, 671 (1964).

69. T. N. Rangaswamy et al., reported at the Conference on $\pi\pi$ and $K\pi$ Interactions at Argonne National Laboratory, May 14-16, 1969; P. Dalpaiz et al., as reported in Ref. 66.

70. M. Roos, Proceedings of the Daresbury Study Weekend on Vector Meson Production and Omega-Rho Interference, 1970, edited by A. Donnachie and E. Gabathuler (Daresbury, 1970), p. 173.

71. J.A.J. Matthews et al., Phys. Rev. Letters 26, 400 (1971).

72. G. E. Chikovani et al., Phys. Letters 25B, 44 (1967); H. Benz et al., Phys. Letters 28B, 233 (1968).

73. H. Alvensleben et al., Phys. Rev. Letters 27, 888 (1971).